Max-Planck-Institut für Metallforschung
Stuttgart

Fatigue Behavior of Sub-Micron Silver and Copper Films

Ruth Schwaiger

Dissertation
an der
Universität Stuttgart

Bericht Nr. 112
Dezember 2001

Fatigue Behavior of Sub-Micron Silver and Copper Films

Von der Fakultät Chemie der Universität Stuttgart
zur Erlangung der Würde einer Doktorin der Naturwissenschaften (Dr. rer. nat.)
genehmigte Abhandlung

vorgelegt von

Ruth Schwaiger

aus Wien (Österreich)

Hauptberichter: Prof. Dr. phil. E. Arzt
Mitberichter: Prof. Dr. rer. nat. F. Aldinger
Tag der mündlichen Prüfung: 12. Dezember 2001

Max-Planck-Institut für Metallforschung und
Institut für Metallkunde der Universität Stuttgart

STUTTGART 2001

Ruth Schwaiger

Fatigue Behavior of Sub-Micron Silver and Copper Films

121 pages, 50 figures, 8 tables

Abstract

Fatigue compromises the reliability of macroscopic metallic components utilized in a variety of technological applications. However, the fatigue behavior of thin metal films and small-scale components used in microelectronics and mechanical microdevices has yet to be explored in detail. The fatigue behavior in (sub)micron thin films is likely to differ from that in bulk material, since the volume necessary for the formation of dislocation structures typical of cyclic deformation is larger than that available in thin films. The microscopic processes responsible for fatigue are, therefore, affected by the thin film dimensions and microstructure. This work focused on the characterization of such mechanisms and the resulting fatigue damage. In particular, the effect of grain size and/or film thickness were investigated.

The fatigue behavior of 0.2-1.5 µm thick, Ag films on SiO_2 and 0.4-3.0 µm thick,Cu films on polyimide substrates was investigated. The films were tested using cantilever microbeam deflection and cyclic tensile testing.

Extrusions similar to those observed in bulk material were found at the Ag and Cu film surfaces after cyclic loading. Voids observed beneath the extrusions, at the film-substrate interface, contributed significantly to thin film failure. The occurrence of these extrusions and voids was qualitatively explained by a model that combines mechanisms of bulk fatigue with the constraints exerted on dislocations by thin film dimensions.

Fatigue lifetime decreased with increasing cyclic amplitude. Moreover, thin films were more fatigue resistant and contained fewer, smaller extrusions than thicker films. We found that a small thickness and/or grain size inhibits void nucleation. This observation is explained in terms of vacancy diffusion and annihilation at free surfaces or grain boundaries.

These investigations shine a new light on a well-known phenomenon and provide a basis for designing thin film devices against cyclic loading.

Max-Planck-Institut für Metallforschung und
Institut für Metallkunde der Universität Stuttgart, 2001

Als Manuskript gedruckt. Printed in Germany.

Ruth Schwaiger

Ermüdungsverhalten von Silber- und Kupferschichten im Submikrometerbereich

121 Seiten, 50 Abbildungen, 2 Tabellen

Kurzzusammenfassung

Ermüdung gilt als eine der wichtigsten Versagensursachen makroskopischer metallischer Bauteile. Das Ermüdungsverhalten in dünnen Metallschichten und miniaturisierten Bauteilen, wie sie in der Mikroelektronik oder Mikrosystemtechnik eingesetzt werden, ist bisher jedoch kaum untersucht worden. Für Abmessungen im Mikrometerbereich kann aber ein anderes Verhalten als in Massivmaterial erwartet werden, da das geringe Materialvolumen die Ausbildung typischer Ermüdungs-Versetzungsstrukturen nicht zuläßt. Die mikroskopischen Prozesse, die Materialermüdung verursachen, werden durch Dimension und Mikrostruktur der dünnen Schicht beeinflußt. Im Rahmen dieser Arbeit werden Ermüdungsschädigung und die dafür verantwortlichen Mechanismen charakterisiert. Im besonderen wird auf die Einflüsse von Schichtdicke und Korngröße eingegangen.

Das Ermüdungsverhalten wurde anhand von 0.2 - 1.5 µm dicken Ag Schichten auf SiO_2- und 0.4 – 3 µm dicken Cu Schichten auf Polyimid-Substrat untersucht. Die Schichten wurden mit Mikrobalkenbiegung und in Zugversuchen zyklisch verformt.

Nach der Ermüdungsbelastung wurden an der Oberfläche der Ag und der Cu Schichten Extrusionen gefunden, die jenen in Massivmaterial gleichen. Unterhalb der Extrusionen, nahe der Grenzfläche zwischen Schicht und Substrat, wurden Poren beobachtet, die wesentlich zur Ermüdung der dünnen Schichten beitrugen. Die Entstehung von Extrusionen und Poren wurde qualitativ mit Hilfe eines Modells erklärt, das Mechanismen aus der Ermüdung von Massivmaterial mit den Einschränkungen, die eine dünne Schicht auf die Versetzungsbewegung ausübt, verbindet.

Die Lebensdauer der Schichten nahm, wie zu erwarten, mit zunehmender Belastung ab. Darüber hinaus waren dünnere Schichten ermüdungsbeständiger und wiesen weniger und kleinere Extrusionen als dicke Schichten auf. Die Nukleation von Poren wurde durch geringe Schichtdicke und/oder Korngröße behindert. Diese Beobachtung kann durch Diffusionsprozesse und das Ausheilen von Leerstellen an der freien Oberfläche oder an Korngrenzen erklärt.

Diese Untersuchungen werfen einerseits ein neues Licht auf ein klassisches Materialphänomen; andererseits schaffen sie Grundlagen für den zuverlässigen Einsatz von Dünnschichtsystemen.

Danksagung

Die vorliegende Doktorarbeit wurde in der Zeit zwischen November 1997 und August 2001 am Max-Planck-Institut für Metallforschung in Stuttgart und Institut für Metallkunde der Universität Stuttgart angefertigt.

Viele Personen haben zum Gelingen dieser Arbeit beigetragen, denen ich hiermit meinen Dank aussprechen möchte.

Im besonderen danke ich Herrn Prof. Dr. E. Arzt für die Stellung dieses Promotionsthemas, sein großes Interesse am Fortgang der Arbeit und für die Übernahme des Hauptberichts.

Herrn Prof. Dr. F. Aldinger danke ich für die freundliche Übernahme des Mitberichts.

Herrn Dr. O. Kraft danke ich für die fördernde Betreuung, sein Interesse und viele Anregungen, die sich aus den zahlreichen Diskussionen ergaben.

Herrn Dr. G. Dehm danke ich für die ausführliche Einschulung am *TEM* und viele wertvolle Diskussionen.

Herrn Dr. D. Müller, Herrn R. Völker und Herrn F. Thiele danke ich für die Herstellung der untersuchten Schichten.

Meinem Lebensgefährten Dr. T. Cramer danke ich besonders für seine große Geduld und stete Motivation während der letzten Monate.

Ich danke allen Mitarbeitern und Kollegen für die gute Zusammenarbeit.

Table of Contents

Chapter 1

Introduction **1**

Chapter 2

Basic Principles and Literature Review **3**

2.1 Thin Film Literature....3

2.2 Fatigue....4

2.2.1 Phenomenological Description....5

2.2.1.1 Stress-controlled fatigue....5

2.2.1.2 Strain-controlled fatigue....7

2.2.1.3 Cyclic creep and mean stress relaxation....9

2.2.1.4 Fatigue crack growth....11

2.2.2 Cyclic Deformation of Face-centered Cubic Metals....14

2.2.2.1 Cyclic stress-strain behavior....14

2.2.2.2 Microstructural changes....16

2.2.2.3 The formation of extrusions....18

2.2.2.4 Cyclic deformation of polycrystalline *fcc* metals....22

2.2.3 Thin Film Fatigue....23

2.2.4 Perspectives of this Work....25

2.2.5 References....26

Chapter 3

Dimensional and Microstructural Influences

on the Fatigue Behavior of Thin Ag films **35**

3.1 Introduction....35

3.2 Experimental details....36

3.2.1 Sample preparation and characterization....36

3.2.2 Microbeam deflection....38

3.3 Results....42

3.3.1 Characterization of the microstructure....42

3.3.2 Monotonic loading and *FEA*....42

3.3.3 Cyclic deformation....45

3.4 Discussion....52

3.4.1 Fatigue damage....53
3.4.2 Influence of a mean stress on fatigue life....58
3.4.3 Influence of the film thickness....60
3.5 Summary and conclusions....64
3.6 Acknowledgements....64
3.7 References....65

Chapter 4

Cyclic Deformation of Polycrystalline Cu Films 71

4.1 Introduction....71
4.2 Experimental details....72
4.2.1 Sample preparation and characterization....72
4.2.2 Testing procedure....73
4.2.3 Transmission electron microscopy....74
4.3 Results....75
4.3.1 Microstructural characterization....75
4.3.2 Monotonic tests....75
4.3.3 Fatigue tests....77
4.3.4 Fatigue damage....79
4.4 Discussion....87
4.4.1 Fatigue Lifetime....87
4.4.2 Microstructure and damage mechanisms....89
4.5 Summary and conclusions....92
4.6 Acknowledgements....93
4.7 References....93

Chapter 5

On the Nucleation of Voids During Fatigue of Thin Cu Films 99

5.1 Introduction....99
5.2 Lifetime model....100
5.3 Comparison of experiment and model....103
5.4 Conclusions....105
5.5 References....105

Chapter 6

Final Remarks **107**

Appendix

A Fatigue testing of thin Ag films **111**

A.1 Grain size distributions..... 111

A.2 Monotonic stress-strain behavior..... 112

A.3 Fatigue tests..... 112

B Grain size distributions of thin Cu films **117**

C List of symbols **118**

D List of abbreviations **121**

Chapter 1 Introduction

This research work is concerned with the fatigue behavior of thin metal films. It is based on findings by several authors that the mechanical properties of thin film materials differ from those of their bulk counterparts. In technological thin film systems, reliability problems were attributed in particular to high internal stresses typical for thin films on rigid substrates, but also repeated stresses were found to be detrimental to device functionality. Thin film properties have been extensively investigated over the last years; however, cyclic deformation of thin films has not yet been studied as thoroughly as monotonic behavior.

Generally, fatigue failure is preceded by microstructural changes in the bulk and formation of damage at the surface. When the cyclic load is large enough to lead to macroscopic plasticity, fatigue failure occurs rather quickly ($<10^4$ cycles) and is referred to as *low cycle fatigue* (*LCF*). When sufficiently small loads are applied, highly localized instead of macroscopic plasticity occurs and the material fails in $>10^4$ cycles, referred to as *high cycle fatigue* (*HCF*). How fatigue mechanisms operate in thin films and if differences to bulk behavior exist, is not yet clear.

This work is roughly divided into three parts: In the first one, the basic principles of fatigue will be described in detail. Furthermore, a brief overview of thin film behavior will be given. This introductory part is then followed by two sections dealing with two different aspects of fatigue, i.e. *LCF* and *HCF*, respectively, in thin metal films.

The investigations to be described were performed utilizing different methods: The *HCF* behavior of Ag films with thicknesses ranging from 0.2 to 1.5 µm on SiO_2 substrates was investigated by cantilever microbeam deflection and will be described in chapter 3. Chapters 4 and 5 characterize the *LCF* behavior of thin Cu films with thicknesses between 0.4 and 3.0 µm on polyimide substrates, which were tested by cyclic tensile testing methods.

These two aspects of thin film fatigue will be discussed separately. Central to both parts, is a characterization of the mechanisms that are relevant in the fatigue of thin metal films. Implications of dimensions and texture on the fatigue life of the specimens will be described.

Chapter 2 Basic Principles and Literature Review

Laws describing the deformation behavior of bulk material cannot readily be applied to thin films. In the last years, the properties of thin films have been extensively studied, especially under monotonic loading, and several testing techniques have been developed. During metal fatigue the material experiences localized plastic deformation and is expected to be subject to strong size effects, as the motion of dislocations may be hindered by smaller sample dimensions. It is the aim of this study to investigate and elucidate size effects in fatigue. As a background, section 2.1 gives a brief overview of the literature on thin film mechanical properties and testing, and section 2.2 is concerned with the fundamental mechanisms of metal fatigue.

2.1 Thin film literature

Properties of thin films with dimensions in the (sub)micron range cannot simply be deduced from the mechanical behavior of bulk samples, since mechanical behavior is controlled by length scales [1], which are inherent to the respective physical mechanisms. In bulk materials, the sample dimensions usually do not interfere with fundamental lengths, but in thin film samples the geometrical as well as the microstructural dimensions are typically of the same order of magnitude and, hence, it is expected that the mechanical properties of the material will be affected by sample dimensions. For instance, the role of constrained dimensions and the presence of a substrate has been treated by Nix [2], who also gave an excellent review of the work of the 1980s on thin film plasticity.

The plastic yield stress of thin films has been investigated extensively during the last years: Experimentally, it has been found that metallic thin films on a substrate support significantly higher stresses than their bulk counterparts, e.g. [3], [4]. A number of models have been proposed to explain this effect: They are based either on the balance of forces exerted on a dislocation pinned by the substrate and the surface [5], or on energy-balance arguments [6], [2], or on the assumption that the stress fields of geometrically necessary dislocations hinder dislocations moving in the film [7]. The influence of the grain size [8] as well as strain hardening [9] have been taken into account. Various aspects of these models have been summarized and discussed by Keller [10], Hommel [11], and Weiss [12].

Specialized techniques have been developed to study mechanical properties in small dimensions as bulk testing methods are generally difficult or impossible to directly apply to thin films. The challenges encountered in measuring thin film mechanical properties are due to

difficulties in specimen fabrication and handling, and in measuring small forces and small deformations. Current methods include substrate curvature measurement, depth-sensing nanoindentation, microbeam bending, microtensile testing, x-ray diffraction, and bulge testing. Elastic, plastic, as well as time-dependent properties can be determined utilizing these techniques, but the various methods are not equally well applicable to determine any characteristic quantity. Recently, thin film testing techniques have been reviewed and critically discussed by Kraft and Volkert [13]. Further recommendations include articles by Brotzen [14], Vinci and Vlassak [15], and Nix [2].

2.2 Fatigue

Fatigue terms changes in materials structures and properties that occur due to a repeated application of stresses and strains. These changes can gradually lead to component failure. Fatigue failures occur in many different forms in ductile, brittle, and non-crystalline materials, and are influenced by temperature and environment, i.e. mechanical fatigue, creep-fatigue, thermomechanical fatigue, corrosion fatigue, and contact fatigue. Fatigue failures attributed to any of these processes generally take place under the influence of cyclic loads with peak values considerably smaller than the “safe” loads determined on the basis of static experiments. The descriptions below pertain to only a small area within this huge field of research, i.e. mechanical fatigue and ductile materials. The list of references is by far not complete, but is supposed to list pioneering work as well as to give an idea of the current concepts and understanding of cyclic deformation.

Fatigue damage can generally be described in terms of (i) fatigue hardening/softening and microstructural changes, (ii) microcrack nucleation, (iii) initiation and propagation of a fatal crack. The fatigue life of a component can therefore be defined as the sum of the number of cycles to initiate a fatigue crack and the number of cycles to propagate it to some final size at which catastrophic failure occurs. It is not always possible to make a clear distinction between crack initiation and crack propagation. The methods based on this definition will be described in 2.2.1.1 - 2.2.1.2. A second definition for fatigue life of a component is the time or number of cycles to propagate an already dominant crack from its initial size to its critical dimension. In this case the basic assumption is that all engineering components are inherently flawed. The decision when the fatigue crack has reached its critical size is related to the fracture toughness of the material. This approach is based on fracture mechanics and will be briefly described in 2.2.1.4.

In section 2.2.2 attention is focused on the mechanisms of cyclic deformation including a description of the cyclic stress-strain behavior of face-centered cubic metals and the corresponding microstructure. Further, the influence of the grain size and results on thin film fatigue will be discussed.

2.2.1 Phenomenological description

2.2.1.1 Stress-controlled fatigue

Fatigue tests under stress control were first introduced by *Wöhler* in the 1860s [16]. This method is relevant for applications where low-amplitude stresses induce nominally only elastic deformation in a component that has been designed for a long life (*high cycle fatigue* (*HCF*) regime). Nevertheless, plastic deformation occurs in the material in a highly localized way. Stress parameters affecting fatigue life are defined in Fig. 2.1, which shows sinusoidal fatigue cycles with zero and non-zero mean stresses. The stress range $\Delta\sigma$, the stress amplitude σ_a, the mean stress σ_m, and the loading ratio R are defined as

$$\Delta\sigma = \sigma_{max} - \sigma_{min} \tag{2.1}$$

$$\sigma_a = \frac{\sigma_{max} - \sigma_{min}}{2} \tag{2.2}$$

$$\sigma_m = \frac{\sigma_{max} + \sigma_{min}}{2} \tag{2.3}$$

$$R = \frac{\sigma_{min}}{\sigma_{max}} \tag{2.4}$$

where σ_{max} and σ_{min} are the maximum and minimum stresses, respectively, in a load cycle.

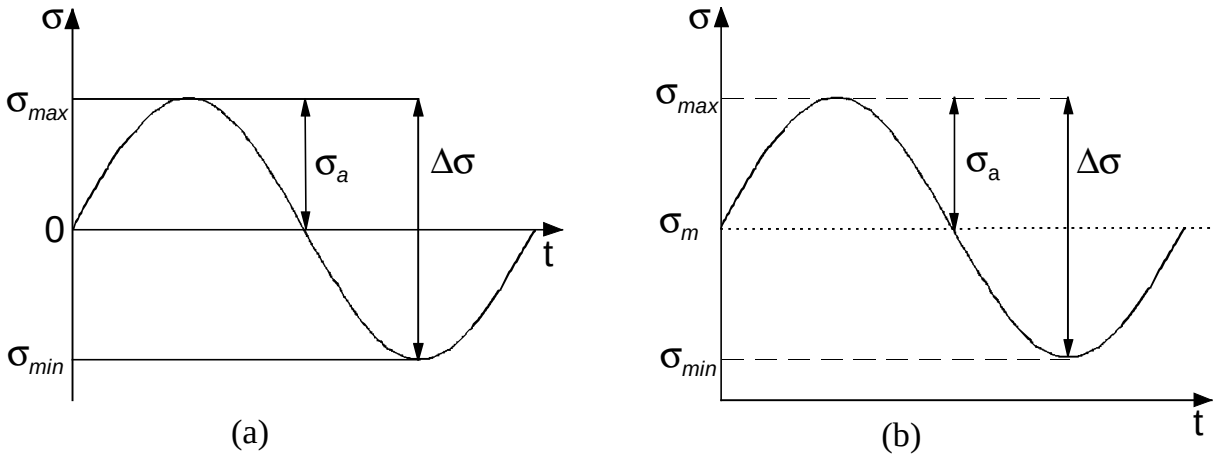

Fig. 2.1: Nomenclature for stress parameters. The variation of stress σ during one cycle for (a) zero and (b) non-zero mean stress is shown.

Stress-life plots (*S-N* curves, often referred to as *Wöhler* curves) describe the fatigue life of nominally defect-free materials with smooth surfaces. *S-N* curves are schematically shown in Fig. 2.2.

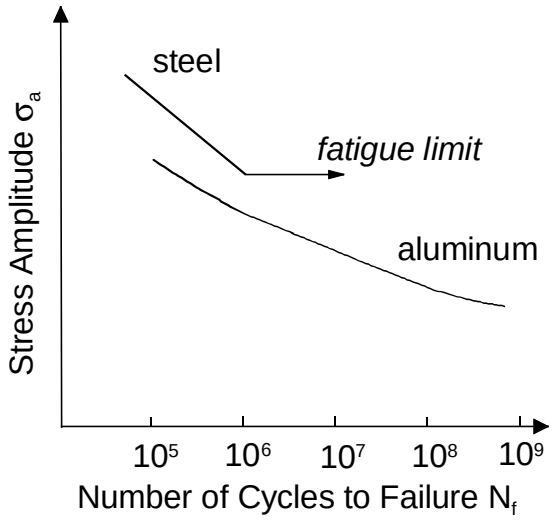

Fig. 2.2: Typical *S-N* diagram showing the variation of the stress amplitude σ_a for fully reversed fatigue loading as a function of the number N_f of cycles to failure for ferrous and non-ferrous alloys, e.g. steel and aluminum, respectively.

The stress amplitude σ_a is plotted versus the number N_f of cycles to failure. N_f implies the number of cycles to initiate fatigue cracks in the smooth specimen plus the number of cycles to propagate a fatigue crack till failure occurs. Under constant stress amplitude loading conditions, a few materials, such as steel and titanium, exhibit a plateau in the *S-N* curve typically beyond about 10^6 fatigue cycles (see for instance [17]). Below this plateau stress, which is called the *fatigue limit*, the material presumably can endure an infinite number of cycles. Most materials, like aluminum, magnesium, and copper alloys do not have a true fatigue limit, as schematically shown in Fig. 2.2. This empirical description pertains to fully reversed fatigue loads, i.e. the mean stress of the fatigue cycle is zero.

The stress amplitude σ_a in a fully reversed, constant amplitude fatigue test can be related to the number $2N_f$ of load reversals to failure by the *Basquin* equation [18],

$$\frac{\Delta\sigma}{2} = \sigma_a = \sigma_f' \cdot (2N_f)^{c_s} \qquad (2.5)$$

where σ_f' is the fatigue strength coefficient and c_s is known as the fatigue strength exponent or *Basquin* exponent, which for most metals is in the range of -0.05 to -0.12 [19].

However, fully reversed stress cycles with zero mean stress are usually not representative for many applications. The mean stress is known to play an important role for the fatigue behavior of engineering materials. A phenomenon known as cyclic creep or ratchetting takes place when plastic strains accumulate from cycle to cycle (see 2.2.1.3).

A number of modifications to stress-life equations have been suggested for loading conditions with mean stresses superimposed on cyclic stresses,. Perhaps the two most common ones are the approaches of Morrow [20] and Smith *et al.* [21]. Morrow [20] has presented a modification of the *Basquin* relation (eq. (2.5)):

$$\sigma_a = (\sigma_f' - \sigma_m) \cdot (2N_f)^{c_s} \qquad (2.6).$$

The number N_f of cycles to failure for any mean stress can then be written as

$$N_f = \left(1 - \frac{\sigma_m}{\sigma_f'}\right)^{\frac{1}{c_s}} \cdot N_f\Big|_{\sigma_m=0} \qquad (2.7)$$

where $N_f\big|_{\sigma_m=0}$ is the number of cycles to failure for zero mean stress. A tensile mean stress can thus be considered to reduce the fatigue strength coefficient, and a compressive mean stress to increase the coefficient. Fatigue life decreases with increasing mean stress.
The stress function of Smith *et al.* [21] will be described in 2.2.1.2.

2.2.1.2 Strain-controlled fatigue

Plastic strain

When considerable plastic deformation occurs during cyclic loading, for example as a consequence of high stress amplitudes or stress concentrations, the fatigue life is considerably shortened. Coffin and Manson proposed independently a plastic strain-based lifetime relation for the so-called *low cycle fatigue* (*LCF*) regime [22], [23]. They found a linear relationship between the logarithm of the plastic strain amplitude ε_{ap} and the logarithm of the number $2N_f$ of load reversals to failure for metallic materials. This relationship can be written as

$$\varepsilon_{ap} = \varepsilon_f' \cdot (2N_f)^{c_d} \qquad (2.8)$$

where ε_f' is the fatigue ductility coefficient and c_d the fatigue ductility exponent. In general, ε_f' is approximately equal to the true fracture ductility in monotonic tension, and c_d is in the range of -0.5 to -0.7 for most metals [24].

Total strain

The total strain amplitude ε_a in a constant strain amplitude test can be written as the sum of the elastic strain amplitude ε_{ae} and the plastic strain amplitude ε_{ap}:

$$\varepsilon_a = \varepsilon_{ae} + \varepsilon_{ap} \qquad (2.9).$$

Using eq. (2.5) and noting that

$$\varepsilon_{ae} = \frac{\sigma_a}{E} \qquad (2.10)$$

where E is Young's modulus, it is found that

$$\varepsilon_{ae} = \frac{\sigma_f'}{E} \cdot (2N_f)^{c_s} \qquad (2.11).$$

Combining eqs. (2.8), (2.9), and (2.11) one obtains

$$\varepsilon_a = \frac{\sigma_f'}{E} \cdot (2N_f)^{c_s} + \varepsilon_f' \cdot (2N_f)^{c_d} \qquad (2.12).$$

The first and second terms on the right hand side are the elastic and plastic components, respectively, of the total strain amplitude. The variations of the elastic, plastic and total strain amplitudes are plotted in Fig. 2.3. as functions of $2N_f$. The *transition life* of a material is defined as the number of load reversals $2N_t$ to failure at which the elastic and plastic strain amplitudes are equal.

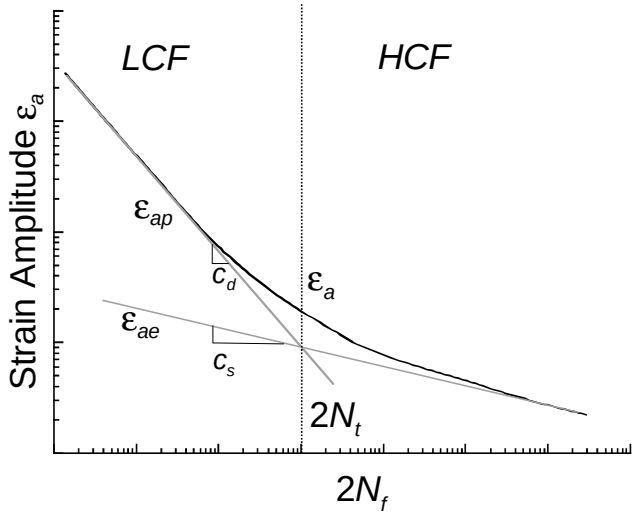

Fig. 2.3: Total strain versus fatigue life. The variations of the elastic, plastic and total strain amplitudes, ε_{ae}, ε_{ap}, and ε_a, respectively, are plotted as functions of load reversals $2N_f$ to failure from equations (2.11), (2.8) and (2.12).

At short fatigue lives, i.e. when $2N_f << 2N_t$, the plastic strain amplitude is more dominant than the elastic strain amplitude and the fatigue life is controlled by ductility. At long fatigue

lives, i.e. when $2N_f >> 2N_t$ the elastic strain amplitude is more significant than the plastic strain amplitude and the fatigue life is controlled by the strength of a material. Mean stress (or strain) effects have been incorporated into the strain-based characterization of fatigue life, too [20]. Combining eqs. (2.6) and (2.12) the strain-life relationship can then be rewritten as

$$\varepsilon_a = \frac{\sigma_f' - \sigma_m}{E} \cdot (2N_f)^{c_s} + \varepsilon_f' \cdot (2N_f)^{c_d} \qquad (2.13).$$

Smith *et al.* [21] proposed that, for a given life, $\sigma_a\varepsilon_a$ for a fully reversed test is equal to $\sigma_{max}\varepsilon_a$ for a test having a mean stress. This proposal leads to

$$\sigma_{max}\varepsilon_a = \sigma_f' (2N_f)^{c_s} \left\{ \frac{\sigma_f' (2N_f)^{c_s}}{E} + \varepsilon_f' (2N_f)^{c_d} \right\} \qquad (2.14)$$

where σ_f', c_s, ε_f', and c_d have the same meaning as above.

Relaxation of the mean stress under strain-controlled fatigue loading is counterpart of the ratchetting mechanism under stress-controlled loading.

2.2.1.3 Cyclic creep and mean stress relaxation

In stress-controlled fatigue experiments under the action of a mean stress a phenomenon known as cyclic creep or ratchetting takes place, as plastic strains accumulate from cycle to cycle. A material, for instance, that shows cyclic softening behavior - which means that the flow stress decreases with increasing number of cycles - will accumulate plastic strain and the mean strain will be shifted to higher tensile strain levels. A compressive mean stress in this case may lead to buckling. Stress-strain cycles for a material exhibiting fatigue softening under the action of a tensile and a compressive mean stress are schematically shown in Fig. 2.4.

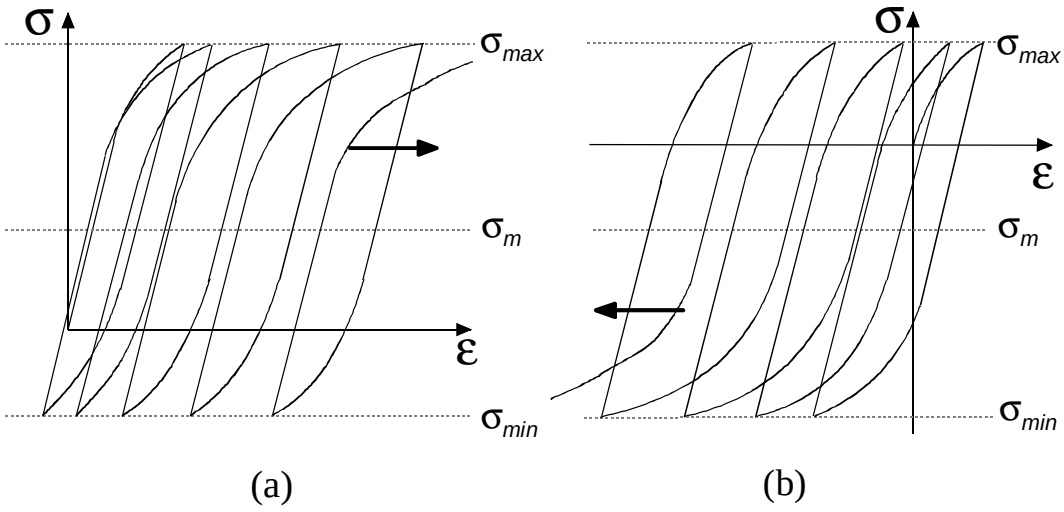

Fig. 2.4: Ratchetting under a (a) tensile and (b) compressive mean stress.

Cyclic strains of a fixed amplitude with a tensile mean strain will lead to a progressive reduction of the mean stress with the number of cycles (for example [25]). The rate of decrease progressively diminishes as the mean stress level approaches zero. Mean stress relaxation can also occur in cyclically hardening materials (for example [26]), where the flow stress increases from cycle to cycle. Cyclic hardening reduces the plastic strain range and increases the stress range for a fixed total strain amplitude. When the mean stress is tensile the material yields more in tension than in compression, which alters the shape of the hysteresis loop in such a way that the tensile stress level increases and the compressive stress level decreases and a relaxation of the mean stress occurs. The two cases of mean stress relaxation described above are schematically shown in Fig. 2.5.

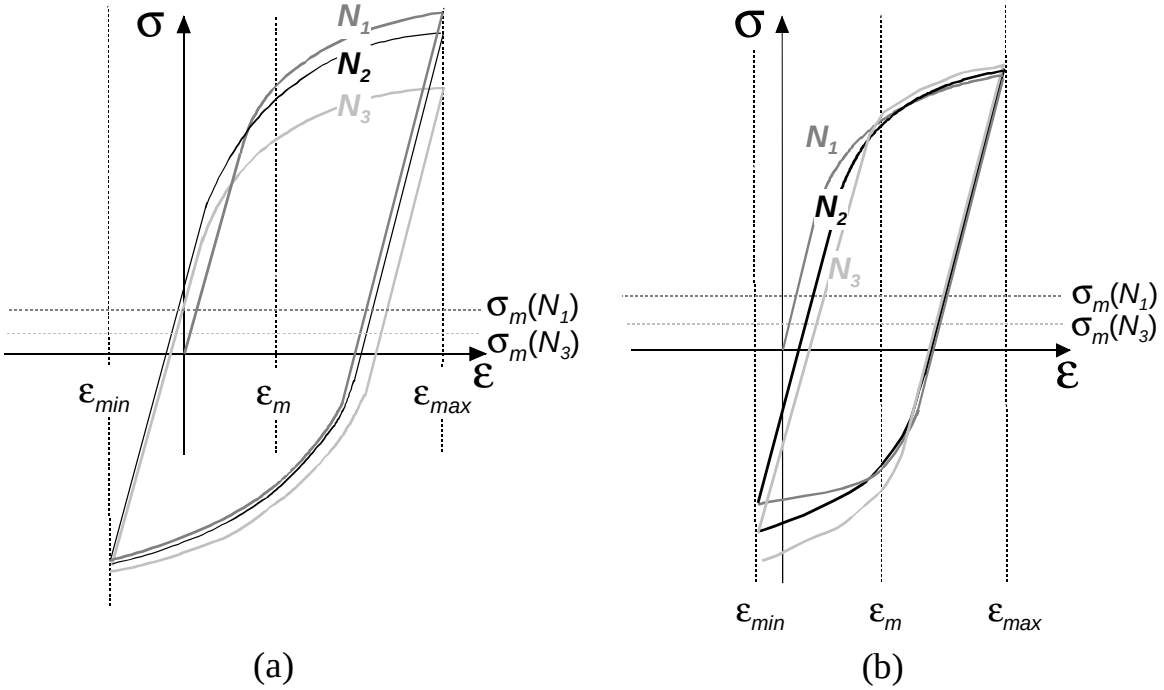

Fig. 2.5: Mean stress relaxation under strain-controlled cyclic loading in a (a) cyclically softening and (b) cyclically hardening material.

2.2.1.4 Fatigue crack growth

Long fatigue cracks

Linear elastic fracture mechanics describe fatigue fracture in case of sufficiently small cyclic stresses[1] The rates at which these cracks propagate are functions of the applied stress, crack length and geometry of the specimen, mean stress, test frequency and environment.

The rate of growth of a fatigue crack subjected to constant stress amplitude cycles can be expressed in terms of the crack length increment da/dN per cycle. Values of da/dN are determined from experimentally measured changes in crack length over a number of elapsed fatigue cycles. When the applied stress range is held constant, the rate of growth of a fatigue crack generally increases with increasing number of cycles; da/dN can be expressed as a unique function of the range ΔK of the stress-intensity factor[2] [28]:

$$\Delta K = K_{max} - K_{min} \tag{2.15}$$

$$\frac{da}{dN} = C \cdot (\Delta K)^m \tag{2.16}$$

where K_{max} and K_{min} are the maximum and minimum values, respectively, of the stress intensity factor during a fatigue cycle, and C and m are scaling constants. The exponent m is typically between 2 and 4 for ductile metallic alloys [29]. These constants are influenced by such variables as material microstructure, environment and temperature, and load ratio R. The load ratio is defined as

$$R = \frac{\sigma_{min}}{\sigma_{max}} = \frac{K_{min}}{K_{max}} \tag{2.17}$$

Eq. (2.16) is applicable for a single mode of loading and for a fixed value of R. For tensile fatigue ΔK refers to the range of mode I[3] stress intensity factors during the stress cycle. It is important to note here that stable fatigue crack growth occurs at stress intensity factor levels $K_{max}=\Delta K/(1-R)$ that are well below the static fracture toughness, K_{Ic}. The *Paris* power law relationship, i.e. eq. (2.16), showing a linear variation of log da/dN with log ΔK, pertains to stable fatigue crack growth over only a portion of the total crack growth resistance curve. A schematic illustration of the different regimes of crack growth, which is typical for most engineering alloys, is given in Fig. 2.6.

[1] When the process zone ahead of a crack tip is not sufficiently small non-linear fracture mechanics have to be applied. A detailed description is given e.g. in [27].
[2] The stress intensity factor is a quantity describing the stress distribution near the crack-tip under linear elastic loading conditions [27].
[3] Mode I is the tensile opening mode in which the crack faces separate in a direction normal to the plane of a crack [27].

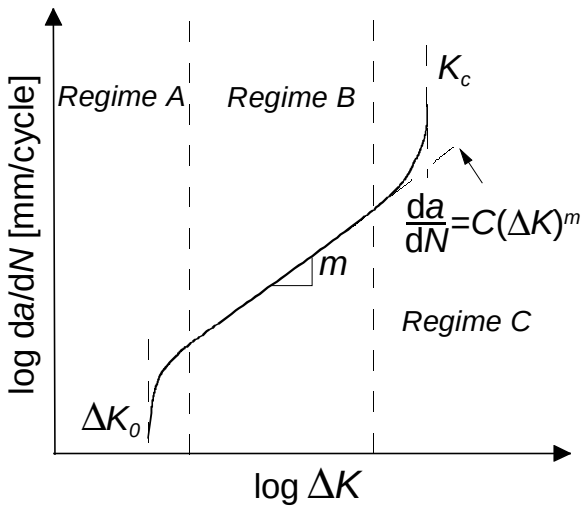

Fig. 2.6: Schematic of the different regimes of fatigue crack propagation.

Three distinct regimes can be identified: *Regime A*, in which the average growth increment per cycle is smaller than a lattice spacing, is associated with the existence of a threshold stress intensity factor range ΔK_0. Below this threshold, cracks either do not grow or grow at undetectable rates; above ΔK_0 there is a steep increase in da/dN with ΔK. *Regime B*, known as the *Paris regime*, exhibits a linear variation of $\log da/dN$ with $\log \Delta K$. *Regime C* is the range of high ΔK values where crack growth rates increase rapidly causing fracture of the remaining cross-section. At this point the stress-intensity factor achieves the value of the static fracture toughness K_{Ic}.

The definition of fatigue life in this section deals primarily with the resistance to fatigue crack growth of an already dominant crack, while the concepts described in section 2.2.1.1 include microstructural changes preceding fatigue crack initiation as well as final failure. This results in different guidelines for the design of components for optimum fatigue resistance. For example, in many applications the resistance to the growth of long fatigue cracks generally increases with an increase in grain size (or a decrease in yield strength) at low ΔK values, where a significant portion of subcritical crack growth happens. On the other hand, when the fatigue life is estimated on the basis of *S-N* plots higher strength materials and finer grained microstructures usually lead to a longer fatigue life.

Short cracks

The growth rates of “small cracks” can be significantly greater than the corresponding rates of “long cracks”. This was first studied by Pearson [30]. A fatigue crack can be considered to be “small” when its size is comparable to the scale of the characteristic microstructural

dimension, such as grain size or particle spacing, or to the size of the plastic zone ahead of the crack tip [31].

For two differently sized long cracks in the same material system, subjected to equal stress intensity values (under small-scale yielding), crack tip plastic zones will be equal in size and equal amounts of crack extension da/dN will be expected. This is not the case for short cracks [32]. Small cracks are observed to grow at stress intensities below the long-crack threshold ΔK_0; some extend with decaying growth rates until arrest, while others propagate quite rapidly and finally merge with long-crack behavior. This is schematically shown in Fig. 2.7.

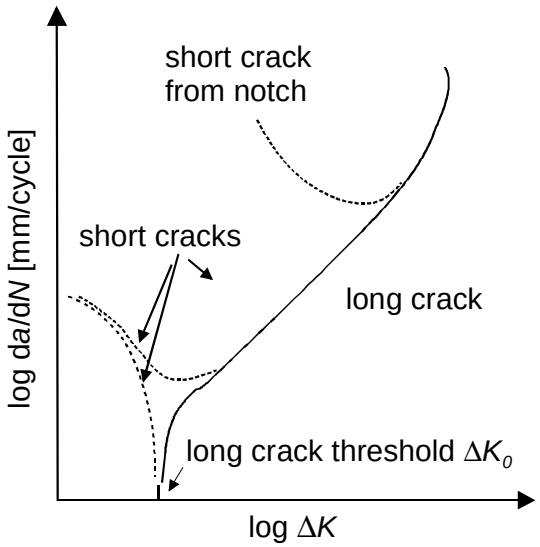

Fig. 2.7: Schematic representation of typical fatigue crack growth rates da/dN, with the nominal cyclic stress intensity factor ΔK, for “long” and “small” cracks. Long cracks remain dormant below ΔK_0 (after [31]).

Crack closure is a major reason for differences in crack growth behavior between long and short cracks. Plasticity-induced crack closure was first commented on by [33]. Crack closure is a result of contact between crack faces behind the advancing crack tip leading to crack tip shielding [34]. As a short crack has a smaller wake, crack closure effects are less pronounced [35], [34], and hence, the crack growth rate of small cracks is increased.

For small cracks of a size approaching microstructural dimensions, additional factors were found to be responsible for anomalous behavior: besides crack closure local arrest at grain boundaries [36], [37] and enhanced plastic deformation at the crack tip [38] influence their growth rate. The plastic zone of such a crack is often related to the grain size, and thus, the crack tip behaves as it would in a preferentially oriented single crystal; the crack front encompasses just one or relatively few grains, so that growth is not averaged over many

probably disadvantageously oriented grains [31]. Furthermore, the behavior of a small crack inside an individual grain is dictated by crystal plasticity resulting in crack deflection and a change in the crack tip driving force as the crack propagates into an adjacent grain [39].

Owing to the presence of a notch an initially short crack propagates through the stress-strain field of the notch before it reaches the bulk stress-strain field and behaves like a long crack. In the plastic field of a notch, linear elastic fracture mechanics cannot be applied, and crack growth rates are much higher than those expected on the basis of the nominal ΔK values. These cracks often exhibit transient crack growth effects until the tip of the small crack leaves the strain field of the notch; in such cases temporary retardation is observed as the crack tip advances ahead of the notch tip. (compare Fig. 2.7). Several attempts have been made to account for the faster growth of short cracks at notches (e.g. [40]-[42]) providing corrections to the physical crack length.

For design issues it is important to note that microstructural modifications, such as a reduced grain size (e.g. [43]), offer an enhanced resistance to crack initiation and the growth of small fatigue cracks, but are generally regarded as disadvantageous to the growth of long cracks. Long cracks are usually impeded by coarse grain structures due to crack deflection and crack closure effects (e.g. [44]).

2.2.2 Cyclic deformation of face-centered cubic metals

2.2.2.1 Cyclic stress-strain behavior

It is now well established that plastic strains are necessary to induce fatigue damage in metals. This goes back to the work of Ewing and Humfrey [45] and Bairstow [46], who performed first microscopic investigations and stress-strain analyses, respectively, of cyclically strained metals. A cyclic stress-strain curve (*CSS* curve) is an important fatigue characteristic of a material and will be described below. It is usually measured in *LCF* constant strain or constant plastic strain amplitude loading. It can also be found from constant stress amplitude loading test [47].

The most conclusive results of cyclic deformation have been obtained on single crystals of face-centered cubic (*fcc*) metals, and the further description given here is restricted to the behavior of *fcc* metals. Cyclic hardening is typical for annealed *fcc* single crystals, oriented for single slip and subjected to cyclic strains under fully reversed loading; the flow stress increases with increasing number of cycles, the changes being strongest at the beginning of cyclic loading. With continued cyclic straining this hardening progressively diminishes and a

quasi-steady state of deformation, referred to as saturation, is reached. The hardening process can be described quantitatively in terms of the stress-strain response of the metal. The cyclic deformation of a single crystal is usually characterized in terms of the resolved shear stress τ_r and resolved shear strain γ_r acting on a specific slip plane along a specific slip direction.

Fig. 2.8 schematically depicts the hysteresis loop representing the relation between τ_r and γ_r within one cycle. The stress amplitude is given by the peak stress τ_s at a total applied shear strain γ_s; plastic and elastic shear strain amplitudes are denoted by γ_{pl} and γ_{el}, respectively. The saturated state is characterized by a hysteresis loop undergoing no further changes.

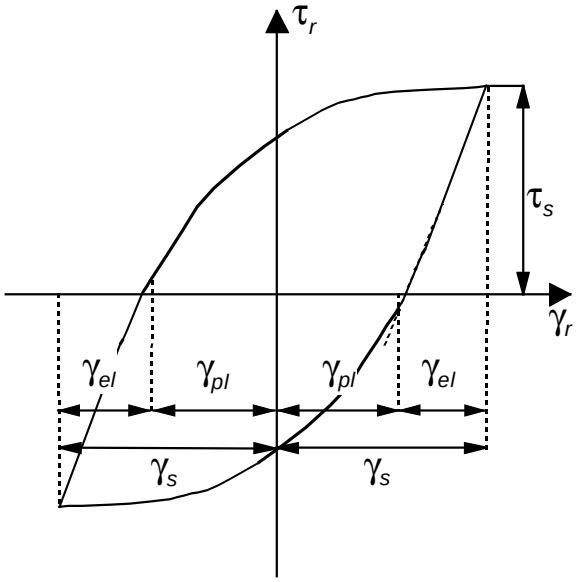

Fig. 2.8: Schematic of τ_r-γ_r hysteresis loop

The *CSS* curve was first experimentally determined by Mughrabi [48]. Fig. 2.9 schematically shows such a curve for *fcc* single crystals oriented for single slip. Cyclic stress-strain curves like this one are typical for a large number of *fcc* single crystals including Cu, Ni, Ag, and Al [49]-[51].

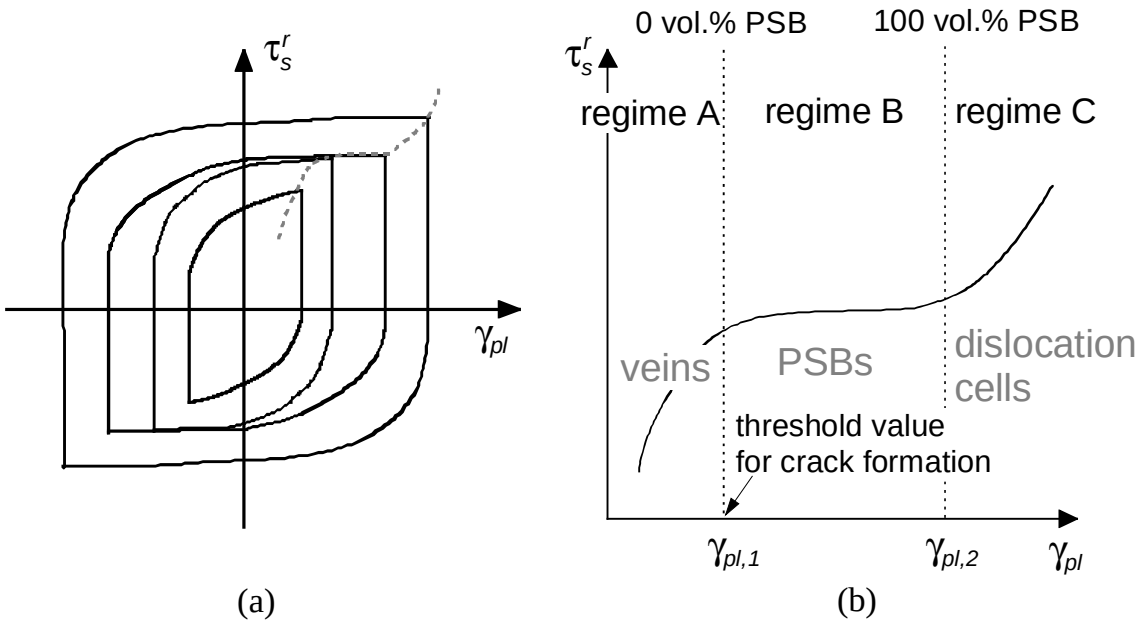

Fig. 2.9: (a) Stable hysteresis loops for different plastic strain amplitudes with the resolved shear stress τ_s^{sat} at saturation plotted against the resolved plastic shear strain γ_{pl}. The *CSS* curve is drawn through the tips of the stable loops obtained at different plastic strain amplitudes. (b) Schematic showing the different regimes of the *CSS* curve of *fcc* single crystals.

The curve in Fig. 2.9(b) can be divided into three regions. In *regime A*, at low values of the applied plastic strain amplitude, hardening occurs and the cyclic strain does not cause progressive damage. The specimen withstands an infinite number of fatigue cycles. This region is followed by a plateau in the *CSS* curve that spans a wide range of γ_{pl} (designated as *regime B*), where the saturation stress τ_s^r is independent of the plastic strain. A further increase in γ_{pl} results in an increase in τ_s^r (*regime C*).

The existence of a plateau in the *CSS* curve and its extent is strongly dependent on the crystallographic direction of the *fcc* crystal along which the fatigue load is applied. When multiple slip occurs, the plateau is less pronounced or does not exist (e.g. [52]-[54]).

2.2.2.2 Microstructural changes

The *CSS* curve presented above (Fig. 2.9(b)) is related to the formation of typical dislocation structures in the three regimes. The dislocation structure in *regime A* at low γ_{pl} is made up of edge dislocation dipoles accumulating on the primary glide plane, called veins, separated by dislocation-poor regions, where screw dislocations ply back and forth during

cyclic straining (see for instance [55]-[58]). In the early stage of fatigue the veins contribute to rapid hardening by partially impeding dislocation motion on the primary slip system. Typically, the value of γ_{pl} does not exceed 10^{-4}.

Plastic strain-controlled cycling in *regime B* leads to the formation of marked slip bands on the specimen surface. Slip is localized along bands, γ_{pl} typically is in the range from 10^{-4} to 10^{-2}. These slip lines were termed "persistent slip bands" (*PSB*s) by Thompson *et al*. [59], who found that in Cu and Ni the bands persistently reappeared at the same sites during continued cycling, even after a thin layer of the surface containing these bands was removed by electropolishing.

The dislocation arrangement in the *PSB* differs from the vein-like structure of the surrounding matrix and is schematically shown in Fig. 2.10 (a) and (b).

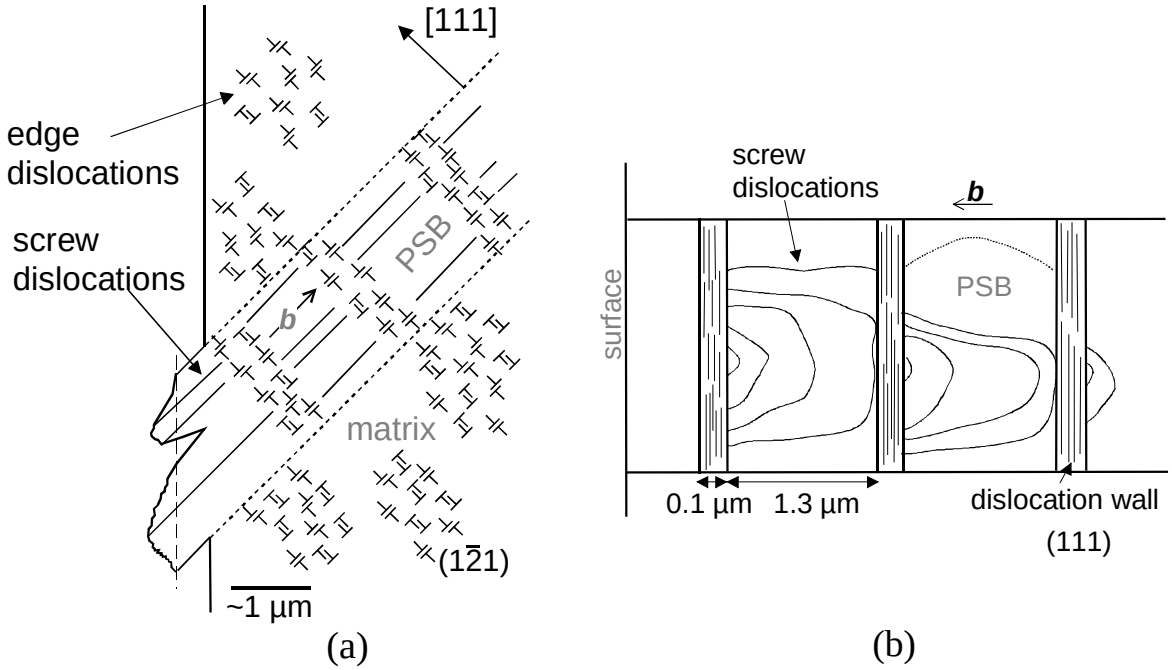

Fig. 2.10: Schematic of a *PSB* structure. A view of the (a) $(1\,\bar{2}\,1)$ section with matrix veins and *PSB* walls (after [60]) and the (b) (111) section is shown (after [61]).

A periodic array of dislocation ladders or walls divides the *PSB* lamella into channels. Fig. 2.10 (a) depicts the dislocation arrangements in a $(1\,\bar{2}\,1)$ section, which contains the primary Burgers vector $\boldsymbol{b} = \frac{1}{2}[\bar{1}01]$ and the normal to the primary glide plane (111). The line direction $[1\,\bar{2}\,1]$ of the primary edge dislocation is at right angles to the plane of the drawing. In Cu single crystals fatigued at room temperature the distance between the walls and the wall

thickness are about 1.3 μm and 0.03 - 0.25 μm, respectively [62]. The walls are predominantly made up of edge dislocation dipoles. In Cu the dislocation densities in the walls are ~$6x10^{15}$ m^{-2} [62], [63]. Two thirds of the dipoles were found to be of the vacancy type, about one third were interstitial dipoles [63], [64]. In the channels in-between screw dislocations were observed with a density of ~$5x10^{13}$ m^{-2} [62]. The volume fraction of the slip bands increases with increasing γ_{pl}.

The condition of saturation (see 2.2.2.1) demands that in the *PSB*s the dislocation densities in channels and walls are maintained constant by a dynamical equilibrium between the multiplication and annihilation of both screw and edge dislocations [49], [65], [66]. Edge dislocation segments bow out of the walls and traverse the channels thereby producing screw dislocations, which then glide along the channels by elongating the edge dislocations along the walls [49], [62]. Thus, a continuous flux of screw dislocations along the channels and of edge dislocations across the walls is maintained.

The sites where *PSB*s emerge at the surface were found to cause surface features such as micronotches where fatigue crack nucleation is promoted [67]. Therefore, the observation of a threshold strain for the formation of *PSB*s (compare Fig. 2.9) implies the existence of a fatigue (stress or strain) limit below which no failure occurs [48], [58].

The last basic type of dislocation structure formed in cyclically deformed *fcc* metals is the cell structure, typical for loading at high γ_{pl}. It can be assumed that the transition from *regime B* to *regime C* occurs when the *PSB*s can no longer accommodate the plastic deformation [68]. Ackermann *et al*. [69] have investigated the dislocation structures of single-crystalline Cu fatigued in the respective range of γ_{pl}, i.e. ~ 10^{-4} - 10^{-2}, by electron microscopy. At higher values of γ_{pl} secondary slip becomes more important; a gradual evolution of a cell structure has been found for $\gamma_{pl} > 2 \times 10^{-3}$. The cell structure starts to form at the *PSB*-matrix interface and expands to fill the *PSB*s. The cell size was found to depend on the amount of plastic strain [70], [71].

2.2.2.3 The formation of extrusions

This section concentrates on surface relief formation and the related dislocation structures for materials in which *PSB*s are formed. However, this is not the only mechanism for surface roughening, because localization of cyclic slip into *PSB*s is not a necessary prerequisite for the formation of a surface relief. For example, there are observations of extrusions at the surface with no *PSB*s but a vein structure underneath [72]; and dislocation cells also lead to surface roughness [70]. Furthermore, in *fcc* single crystals of low stacking-fault energy, the typical

dislocation structure after cycling can be characterized as planar arrays of dislocations in the whole volume of the fatigued material [73]. There are no zones of specific dislocation structures but extrusions build up during cyclic loading. The details of surface extrusion formation in those cases are not known. In general, it can be assumed that non-localized slip, when not replaced by localized slip, can also produce extrusions.

The first report of slip-induced surface roughening during fatigue goes back to Forsyth [74]. At sites where *PSB*s emerge at the surface, extrusions and intrusions are formed. Several models have been proposed to explain the formation of the surface extrusions. These models are based either on slip processes [68], [75]-[77] or on the formation and migration of point defects [78], or a combination of both [79]. Antonopoulos *et al.* [64] start with assumptions similar to Essmann *et al.* [79], but do not consider the formation of point defects. The models presented in Refs. [75]-[77] provide a micromechanical description of the behavior of dipolar dislocation layers under alternating stresses, but microscopic aspects evident from *TEM* observations have not been incorporated. The other models listed above take into account known dislocation properties and features of the dislocation substructure that have been revealed by *TEM*; they will be briefly outlined below.

Many observations suggest that both dislocation glide and point-defect production are important aspects of fatigue deformation: It is widely accepted that dislocation glide is irreversible in the *PSB* [49], [66], [79], and governed by the generation and annihilation of screw dislocations in the channels and edge dislocations in the walls, respectively. The critical distance for the annihilation of two screw dislocations by cross slip in Cu was found to be 50 nm at room temperature [49], [79]. A dipole consisting of edge dislocations of opposite sign will annihilate if the spacing between the edge dislocations becomes smaller than about 1.6 nm [79].

Electrical resistivity measurements showed that the concentration of point defects produced during fatigue increases significantly with γ_{pl} [80], [81]. Further, it has been found in *TEM* that the majority of the dislocation dipoles observed after fatigue are vacancy dipoles [64]. These features form the basis of the model of Essmann *et al*. [79], which refers to dislocation behavior after the establishment of *PSB*s. The required dynamic equilibrium of dislocation density in saturation (e.g. [65]) is accounted for by allowing a balanced creation and annihilation of both screw and edge dislocations. The elimination of edge dislocation dipoles in the walls of a *PSB* is envisaged as giving rise to vacancies. The production of vacancies is balanced by vacancy capture by dislocations passing within a critical distance.

The formation of extrusions involves microscopic slip processes of edge dislocations accompanied by dipole annihilation in the walls of the *PSB*. The paths of intermediate members of vacancy dipoles terminate at opposite *PSB*-matrix interfaces, resulting in interface dislocations (i.e. dislocations at the interface between the *PSB* and the matrix) with their extra halfplanes directed into the *PSB*; the *PSB* is thus in a state of compression. These interface dislocations glide under stress and leave the specimen surface, causing the extrusion of material along the Burgers vector direction. The height of the extrusions is determined by the product of the glide path length across the crystal, i.e. the sample size or the grain size, and the saturation vacancy concentration. Annihilation of screw dislocations also has important consequences, slip steps are formed when screws leave the surface, but annihilations render their glide random, so that the *PSB* profile becomes statistically roughened [82].

Fig. 2.11 illustrates the case when a large number of microsopic slip processes are superimposed. Dislocations moving during tensile loading are denoted by solid symbols and those moving during compressive loading by open symbols. Under the action of the applied stress, the interface dislocations glide out of the crystal at A and A' during the tensile phases, and at B and B' during the compressive phase, respectively.

A staircase-like glide sequence ($X \leftrightarrow Y$ in Fig. 2.11) is shown in more detail in the lower right corner; vacancies are produced by annihilation of unlike edge dislocations. The arrangement of interface dislocations in Fig. 2.11 leads to a compressive stress within the *PSB* and to a tensile stress in the matrix.

The model predicts the effect of temperature on *PSB* profiles according to the mobility of vacancies. At low temperatures, when vacancies are immobile, the extrusion is of fixed height, it stops growing when all interface dislocations have left the sample. At higher temperature, when vacancies move away from the *PSB*, the equilibrium concentration is restored by formation of more vacancies and deposition of more interface dislocations, so that the extrusions will grow continuously.

These predictions do not match the experimental observations [83], [84]: The largest extrusions form at temperatures where point defects are immobile, at room temperature small extrusions form only if the cycling speed is low enough, and above room temperature extrusions do not form.

The combined effect of applied stress and internal stress can produce high local stresses at A, A', B and B', these interfaces are expected to act as preferential sites for fatigue crack nucleation. Direct experimental evidence of crack initiation at the interface has been obtained by Hunsche and Neumann [67] and Ma and Laird [85], [86].

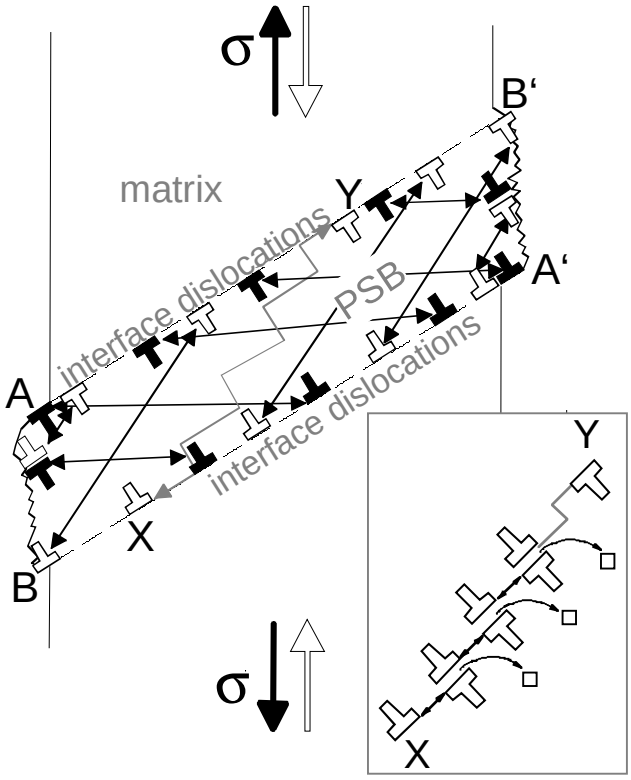

Fig. 2.11: Formation of extrusions by emergence of *PSB*-matrix interface dislocations. Basic mechanism of glide and annihilation of edge dislocations results in a series of staircase-like glide sequences (as shown in detail in the lower right corner). The extra halfplanes of the interface dislocations are directed into the *PSB* lamella. All other microstructural features (edge dislocation walls, screw dislocations) have been omitted for the sake of clarity. Full and open symbols correspond to the glide sequences in tension and compression, respectively. Annihilation of edge dislocations take place in the walls.

The model of Antonopoulos *et al.* [64] is based on weak-beam *TEM* investigations, which showed that the narrow edge dislocation dipoles that build up the walls in the *PSB* and the veins in the matrix have predominantly vacancy character [64]. The authors assume that the density of these vacancy dipoles in the *PSB*s becomes larger than that in the matrix during cyclic saturation, but they do not consider the annihilation of the dipoles and thus the formation of vacancies. The long-range effect of this dislocation distribution is described by replacing each dislocation wall in the *PSB* by fictitious interface dislocations. Thus, the whole *PSB* can be described by interface dislocations similar to those shown in Fig. 2.11, but the extra halfplanes are directed out of the *PSB*. Therefore, the internal stress in the *PSB* is tensile in the direction of the primary Burgers vector. This prediction is contradictory to that of Essmann *et al*. [79].

The interface dislocations are not considered as glide dislocations that can emerge at the surface, hence they are not involved in the development of surface topography. Rather, it is envisaged that the motion of screw dislocations is responsible for the production the vacancy-type dipoles [87] and generates extrusions by a cross-slip mechanism [88].

Polák [78] proposed a model based on the flux of vacancies in the *PSB*s. Point defects are continuously produced by non-conservative motion of the jogs on screw dislocations and the mutual annihilation of two opposite edge dislocations moving on adjacent slip planes [89]. The vacancies are formed both in the walls and in the channel areas between the walls. As the densities of dislocations in the walls and in the channels differ considerably and edge dislocations serve as sinks for vacancies, the excess vacancy concentration will differ, too. Therefore, a concentration gradient arises and vacancies migrate from the channels into the walls, which is equivalent to the flow of atoms in the opposite direction. This results in the accumulation of mass in the *PSB*, and the material is extruded from the crystal. This model is less elaborate compared to the model of Essmann *et al*. [79] and differences exist regarding the spatial distribution of the point defect formation and the subsequent point defect migration.

2.2.2.4 Cyclic deformation of polycrystalline fcc metals

Persistent slip is generally accepted to be a bulk phenomenon in single crystals but has been proven to occur on the surface of polycrystalline metals as well as within the bulk of polycrystalline metals (e.g. [90]-[93]). *PSB*s are typical for single-slip-oriented grains and thus for slip systems with high *Schmid* factors.

The cyclic stress-strain response of polycrystalline metals can be expected to differ from that of single crystals simply because the various grains have different orientations. Reports on the *CSS* curve of polycrystals are contradictory. Rasmussen and Pedersen [91] performed experiments at low cycling frequencies (0.25 Hz) and low amplitudes of plastic strain ($\sim 10^{-3}$) and found a plateau, although it was less pronounced than the one for single crystals. Polák *et al.* [94] found a region of low cyclic strain hardening, which they find comparable to the plateau found for single crystals. It has to be mentioned that their experiments were performed at a cycling frequency of 80 Hz. The saturation in both cases was found to correspond to an increase in the number of *PSB*s at the surface. These results were obtained on coarse-grained samples with grain sizes ranging from 100 to 300 μm. In coarse-grained polycrystals *PSB*s formed within interior grains produce slip that is confined to the individual grain; the grains were found to deform mainly by single slip [91]. For fine-grained polycrystalline *fcc* metals multislip is more pronounced. The *CSS* curve shows no plateau [95] and can be compared to

the *CSS* curve of single crystals oriented for multiple slip [54]. In nano-crystalline Cu fatigued at low strain amplitudes no *PSB*s in the interior grains have been found, but surface damage reminiscent of the extrusions and intrusions associated with *PSB*s. The existence of *PSB*s in the surface grains could not be excluded [96].

The influence of the grain size on the fatigue life was studied by Thompson and Backofen [97] and Lukáš and Kunz [98]. Investigating the fatigue life in terms of the stress amplitude both groups of authors found that the grain size affected the fatigue life of Cu in the *LCF* region, whereas the fatigue limit did not depend on the grain size. But effects of the grain size are sometimes more significant, when the fatigue life is expressed in terms of the plastic strain amplitude. This has been discussed by Lukáš and Kunz [98].

In the last years ultrafine-grained metals have become the subject of interest: in those materials the stress fatigue limit was enhanced [99] compared to copper of conventional grain sizes [97], [98]. A comprehensive review of earlier work and ideas on grain-size effects in fatigue as well as a summary of recent findings for ultrafine-grained metals has been presented by Mughrabi [100].

2.2.3 Thin Film Fatigue

The fatigue properties of thin films have not been investigated as thoroughly yet as those of bulk materials. It is now well accepted that the mechanical properties of thin metal films may differ from those measured in bulk form, as typical microstructures in such systems include very fine grain diameters and sometimes textures. Grain diameters are often of the same order of magnitude as the film thickness, typically less than one micrometer, and localized deformation becomes important in such systems. Given only limited material in the thickness direction, we expect films to show different fatigue behavior compared to that of bulk materials. This becomes clear upon realization that dislocation structures can reach a limiting, absolute dimension during deformation. For instance, *PSB*s with characteristic wall-spacings of approximately 1.3 µm develop in Cu that has been cyclically deformed into saturation [63], [49] (see 2.2.2.2). Another reason for a possible size-effect in fatigue behavior is the high surface-to-volume ratio in thin films, where almost all grains have a free surface.

Experimental data on thin film fatigue and a size-effect are contradictory and not conclusive. Most experiments have been performed on Cu, for very obvious reasons: the fatigue behavior of bulk Cu single and polycrystals has been well characterized, not to mention its technological role in microelectronics and packaging. Most experiments have been performed on samples with thicknesses of at least several microns, results obtained on films in the (sub)micron range are rare.

A variety of experimental techniques have been developed for fatigue testing of thin foils and thin films. Several uniaxial tension/tension fatigue tests were performed [101]-[106]. A uniaxial tension/compression mode fatigue characterization is possible by testing a thin film deposited on an elastic substrate, which then is subjected to cyclic loading [107], [108]. Another method is a bending type fatigue characterization [109]-[111]. In bending, rather than uniform strain across the specimen, a strain gradient through the sample thickness exists.

Judelewicz *et al.* [102] conducted fatigue tests on Cu foils of 20 and 100 µm thickness fabricated by cold rolling and annealing. They reported thickness dependent behavior, to the effect that thinner specimens sustained more cycles at the same stress amplitude. Samples of 100 µm thickness failed after a number of cycles 10-30 times lower than that for the thinner foils. Concerning the dislocation structures, they also found a thickness effect: after the same number of cycles the thicker specimens contained a large number of well-defined, sharp slip bands with well-developed extrusions, whereas the thinner specimens were almost free of extrusions and contained only a few grains with faint slip bands. In the case of the 100 µm thick foils the cyclic stress-strain curve was determined [101]; a plateau region comparable to bulk single crystals was reported, as well as bulk-like dislocation structures, i.e. veins and *PSB*s in the plateau region, a cell structure at low, and a quasi-ladder structure at high plastic strains.

A size-effect has been shown in a fatigue study of copper and gold wires performed by Hofbeck *et al*. [112]. Thinner wires were found to sustain significantly more cycles than thicker wires; for the same stress amplitude wires of 25 µm diameter had an endurance of 10^5 cycles, whereas wires of 95 µm diameter ruptured at 10^2 - 10^3 cycles. This behavior was interpreted in terms of a lack of *PSB* formation due to surface annihilation of dislocations.

Hong and Weil [103] studied the fatigue behavior of Cu foils that were 25 and 33 µm thick; they found no appreciable difference regarding the fatigue life between the thin foil material and its bulk counterpart. Dislocation cell structures in grains larger than 2 µm were found, but none in smaller grains.

Merchant *et al.* [109] tested electrodeposited Cu foils in the same thickness range (12 and 35 µm). They performed strain-controlled bending tests and compared the *Coffin-Manson* parameters (see 2.2.1.2) to those of larger scaled polycrystalline Cu. Enhanced fatigue resistance was observed with decreasing foil thickness. Cracks initiated at the foil surface, where the maximum strain was, and propagated along the high angle grain boundaries across the width and through the thickness of the sample; high angle grain boundaries oblique to the crack propagation direction hindered the forward motion of a crack. There were only few slip

bands, probably due to the small grain size of the samples; cellular patterns as well as grid networks over the grain boundaries were found.

Cu films of 1.1 µm thickness were investigated by Read [105]. The Cu films were capped on both sides by 50 nm thick Ti layers. The average grain size was smaller than 1 µm, and the grain structure columnar. After the fatigue tests there were no extrusions on the surface, but microcracks in the cap layer. Only few dislocations, but no dislocation cells or slip bands were observed in the fatigued specimen.

Cyclic loading of free-standing 1 µm thick Al films showed that at small strains their behavior is to a large extent characterized by anelastic processes [106], which were also observed in monotonic tensile testing [113].

Only little information on fatigue crack growth in thin foils is available. Hadrboletz *et al.* [114] investigated free-standing rolled and electrodeposited Cu films of thicknesses ranging from 20 µm to 250 µm. When the ratio of the grain size to the foil thickness was close to or larger than unity fewer slip systems seemed to be activated. Crack propagation was also influenced by the foil thickness: for specimens with a thickness up to 150 µm the crack propagation rate decreases with increasing crack length, whereas in case of bulk material opposite behavior was observed. This was explained by a transition from a plane stress state to a plane strain state with increasing film thickness. Furthermore, crack arrest due to grain boundaries and bifurcation occurred resulting in temporary saturation of the crack propagation rate.

2.2.4 Perspectives of this work

Bulk fatigue models do not apply to the behavior of small-scaled specimens. Since dislocations are involved in the fatigue process, the effects of substrate, interface, the free surface, and the grain size have to be considered.

We expect size-effects in all stages of the fatigue process: It is questionable if dislocation structures typical for bulk fatigue, such as persistent slip bands or cell structures, form, since their characteristic dimensions may exceed film thickness and grain size. Hence, the damage mechanisms may differ compared to those active in bulk and influence the height of extrusions. Effects on the fatigue crack growth behavior can also be expected, since the film thickness and the presence of a substrate affect the stress state at the crack tip. Furthermore, the crack length is usually of similar size as film thickness and microstructural dimensions, and laws valid for long cracks may not apply. All these points put up the question, if and how the fatigue lifetime of thin films is affected by dimensional and microstructural constraints.

In this research work some aspects of thin film fatigue were investigated. *HCF* as well as *LCF* behavior of thin Ag and Cu films was studied utilizing two different methods, cantilever microbeam deflection and cyclic tensile tests, respectively. Central to both tasks is the question whether the film thickness influences the fatigue resistance.

The objective of the findings to be presented is to show similarities and differences to bulk fatigue behavior. We focus on microstructural changes during fatigue, the formation of fatigue damage, and crack initiation. The issue of crack propagation in thin films will not be addressed. A qualitative model of the mechanisms that are responsible for damage formation in thin metal films will be given.

2.3 References

1. Arzt, E., "Size effects in materials due to microstructural and dimensional constraints: a comparative review", *Acta Mater.* **46** (16), 5611-5626 (1998).
2. Nix, W. D., "Mechanical Properties of Thin Films", *Metall. Trans. A* **20**, 2217-2245 (1989).
3. Venkatraman, R. and Bravman, J. C., "Separation of film thickness and grain boundary strengthening effects in Al thin films on Si", *J. Mater. Res.* **7** (8), 2040-2048 (1992).
4. Keller, R.-M., Baker, S. P. and Arzt, E., "Quantitative Analysis of Strengthening Mechanisms in Thin Cu Films: Effects of Film Thickness, Grain Size, and Passivation", *J. Mater. Res.* **13** (5), 1307-1317 (1998).
5. Murakami, M., Kuan, T.-S. and Blech, I. A., "Mechanical Properties of Thin Films on Substrates", in *Treatise on Materials Science and Technology*, Vol. 24 (Academic Press, (1982)), pp. 163-210.
6. Chaudari, P., "Plastic properties of polycrystalline thin films on a substrate", *Phil. Mag. A* **39** (4), 507-516 (1979).
7. Ronay, M., "Yield stress of thin fcc polycrystalline metal films bonded to rigid substrates", *Phil. Mag. A* **40** (2), 145-160 (1979).
8. Thompson, C. V., "The Yield Stress of Polycrystalline Thin Films", *J. Mater. Res.* **8** (2), 237-238 (1992).
9. Nix, W. D., "Yielding and Strain Hardening of Thin Films on Substrates", *Scripta Mater.* **39** (4-5), 545-554 (1998).
10. Keller, R.-M., "Thermomechanisches Verhalten und Mikrostruktur dünner, polykristalliner Kupferschichten", *PhD Dissertation* (Institut für Metallkunde, Universität Stuttgart (1996)).

11. Hommel, M., "Röntgenographische Untersuchung des monotonen und zyklischen Verformungsverhaltens dünner Metallschichten auf Substraten", *PhD Dissertation* (Institut f. Metallkunde, Universität Stuttgart (2000)).
12. Weiss, D., "Deformation Mechanisms in Pure and Alloyed Copper Films", *PhD Dissertation* (Institut für Metallkunde, Universität Stuttgart (2000)).
13. Kraft, O. and Volkert, C., "Mechanical testing of thin films and small structures", *Advanced Engineering Materials* **3** (3), 99-110 (2001).
14. Brotzen, F. R., "Mechanical Testing of Thin Films", *Int. Mater. Rev.* **39** (1), 24-45 (1994).
15. Vinci, R. P. and Vlassak, J. J., "Mechanical Behavior of Thin Films", *Ann. Rev. Mater. Sci.* **26**, 431-462 (1996).
16. Wöhler, A., "Versuche zur Ermittelung der auf die Eisenbahnwagen-Achsen einwirkenden Kräfte und der Widerstandsfähigkeit der Wagen-Achsen", *Zeitschrift f. Bauwesen* **10**, (1860).
17. Suresh, S., "Fatigue of Materials", Cambridge University Press, Cambridge (1998), p. 222.
18. Basquin, O. H., "The exponential law of endurance tests", *Proc. of the ASTM* **10**, 625-630 (1910).
19. Dieter, G. E., "Mechanical Metallurgy", McGraw-Hill, (1988), p. 392.
20. Morrow, J. D., in *Fatigue Design Handbook - Advances in Engineering*, Vol. 4, Sec. 3.2 (Society of Automotive Engineers, Warrendale, PA, (1968)), pp. 21-29.
21. Smith, K. N., Watson, P. and Topper, T. H., "A Stress-Strain Function for the Fatigue of Metals", *Journal of Materials* **5** (4), 767-778 (1970).
22. Coffin, L. F., Jr., "A study of the effects of cyclic thermal stresses on a ductile metal", *Trans. ASME* **76**, 931-950 (1954).
23. Manson, S. S., "Behavior of materials under conditions of thermal stress", *National advisory commission on aeronautics: Report 1170* (Lewis flight propulsion laboratory, Cleveland (1954)).
24. Dieter, G. E., "Mechanical Metallurgy", McGraw-Hill, (1988), p. 391.
25. Bergmann, J., Klee, S. and Seeger, T., "Über den Einfluß der Mitteldehnung und Mittelspannung auf das zyklische Spannungs-Dehnungs- und Bruchverhalten von StE70", *Materialprüfung* **19** (1), 10-17 (1977).
26. Sandor, B. I. and Schauer, J. F., "The relaxation of mean stresses at elevated temperatures", in *Dimensioning and Strength Calculations,* edited by Czoboly, E. (Fourth

Conference on Dimensioning and Strength Calculations, Akadémiai Kiadó, Budapest (1971)), pp. 185-191.

27. Broek, D., "Elementary Engineering Fracture Mechanics", Martinus Nijhoff Publishers, The Hague (1984).
28. Paris, P. C., Gomez, M. P. and Anderson, W. E., "A rational analytic theory of fatigue", *The trend in engineering* **13**, 9-14 (1961).
29. Dieter, G. E., "Mechanical Metallurgy", McGraw-Hill, (1988), p. 398.
30. Pearson, S., "Initiation of fatigue cracks in commercial aluminium alloys and the subsequent propagation of very short cracks", *Eng. Fract. Mech.* **7**, 235-247 (1975).
31. Ritchie, R. O. and Lankford, J., "Small fatigue cracks: a statement of the problem and potential solutions", *Mater. Sci. Eng.* **84**, 11-16 (1986).
32. Ritchie, R. O. and Suresh, S., "The fracture mechanics similitude concept: questions concerning its application to the behavior of short fatigue cracks", *Mater. Sci. Eng.* **57**, L27-L30 (1983).
33. Elber, W., "Fatigue crack closure under cyclic tension", *Eng. Fract. Mech.* **2**, 37-45 (1970).
34. Ritchie, R. O. and Yu, W., "Short Crack Effects in Fatigue: A Consequence of Crack Tip Shielding", in *Small Fatigue Cracks* (Metallurgical Society of AIME, Warrendale, PA, (1986)), pp. 167-189.
35. Pineau, A., "Short Fatigue Crack Behavior in Relation to Three-Dimensional Aspects and Crack Closure Effect", in *Small Fatigue Cracks* (Metallurgical Society of AIME, Warrendale, PA, (1986)), pp. 191-211.
36. James, M. R. and Morris, W. L., "The Effect of Microplastic Surface Deformation on the Growth of Small Cracks", in *Small Fatigue Cracks* (Metallurgical Society of AIME, Warrendale, PA, (1986)), pp. 145-156.
37. Tanaka, K., "Modeling of Propagation and Non-Propagation of Small Fatigue Cracks", in *Small Fatigue Cracks* (Metallurgical Society of AIME, Warrendale, PA, (1986)), pp. 343-361.
38. Lankford, J. and Davidson, D. L., "The Role of Metallurgical Factors in Controlling the Growth of Small Fatigue Cracks", in *Small Fatigue Cracks* (Metallurgical Society of AIME, Warrendale, PA, (1986)), pp. 51-71.
39. Suresh, S., "Crack deflection: implications for the growth of long and short fatigue cracks", *Metall. Trans. A* **14**, 2375-85 (1983).

40. Smith, R. A. and Miller, K. J., "Prediction of Fatigue Regimes in Notched Components", *Int. J. Mech. Sci.* **20**, 201-206 (1978).
41. El Haddad, M. H., Topper, T. H. and Topper, T. N., "Fatigue Life Predictions of Smooth and Notched Specimens Based on Fracture Mechanics", *J. Eng. Mater. Technol.* **103**, 91-96 (1981).
42. El Haddad, M. H., Dowling, N. E., Topper, T. H. and Smith, K. N., "J-Integral Applications for Short Fatigue Cracks at Notches", *Int. J. Fracture* **16**, 15-30 (1980).
43. Brown, C. W. and King, J. E., "The Relevance of Microstructural Influences in the Short Crack Regime to Overall Fatigue Resistance", in *Small Fatigue Cracks* (Metallurgical Society of AIME, Warrendale, PA, (1986)), pp. 73-95.
44. Suresh, S. and Ritchie, R. O., "Near-threshold fatigue crack propagation: a perspective on the role of crack closure", in *Fatigue Crack Growth Threshold Concepts* (Metallurgical Society of AIME, Warrendale, PA, (1984)), pp. 227-261.
45. Ewing, J. A. and Humfrey, J. C., "The fracture of metals under rapid alterations of stress.", *Phil. Trans. Royal Soc. London A* **200**, 241 (1903).
46. Bairstow, L., "The elastic limits of iron and steel under cyclic variations of stress.", *Phil. Trans. Royal Soc. London* **210**, 35-55 (1910).
47. Pohl, K., Mayr, P. and Macherauch, E., "Cyclic deformation behavior of a low carbon steel in the temperature range between room temperature and 850K.", *Int. J. Fracture* **17** (2), 221-33 (1981).
48. Mughrabi, H., "The cyclic hardening and saturation behavior of copper single crystals", *Mater. Sci. Eng.* **33**, 207-223 (1978).
49. Mughrabi, H., Ackermann, F. and Herz, K., "Persistent slipbands in fatigued face-centered and body-centered cubic metals", in *Fatigue Mechanisms* (Special Technical Publication 675, ASTM, Philadelphia, PA, (1979)), pp. 69-97.
50. Mecke, K. and Blochwitz, C., "Saturation dislocation structures in cyclically deformed nickel single crystals of different orientations", *Crystal Res. & Technol.* **17**, 743-758 (1982).
51. Dhers, J. and Driver, J., "The cyclic response and microstructure of aluminium single crystals", in *Basic Mechanisms in Fatigue of Metals,* edited by Lukás, P. and Polák, J. (Proc. of the Int.. Colloquium, Elsevier, Amsterdam, NL (1988)), pp. 33-40.
52. Lepistö, T. K. and Kettunen, P. O., "Comparison of the cyclic stress-strain behaviour of single- and <111> multiple-slip oriented copper single crystals", *Mater. Sci. Eng.* **83**, 1-15 (1986).

53. Gong, B., Wang, Z. G. and Zhang, Y. W., "The cyclic deformation behavior of Cu single crystal oriented for double slip", *Mater. Sci. Eng. A* **194**, 171-178 (1995).
54. Gong, B., Wang, Z. and Wang, Z. G., "Cyclic deformation behavior and dislocation structures of [001] copper single crystals - I. Cyclic stress-strain response and surface feature", *Acta Mater.* **45** (4), 1365-1377 (1997).
55. Basinski, S. J., Basinski, Z. S. and Howie, A., "Early stages of fatigue in copper single crystals", *Phil. Mag.* **19**, 899-924 (1969).
56. Hancock, J. R. and Grosskreutz, J. C., "Mechanisms of fatigue hardening in copper single crystals", *Acta Metall.* **17**, 77-97 (1969).
57. Winter, A. T., "A model for the fatigue of copper at low plastic strain amplitudes", *Phil. Mag.* **30**, 719-738 (1974).
58. Laird, C., "The fatigue limits of metals", *Mater. Sci. Eng.* **22**, 231-236 (1976).
59. Thompson, N., Wadsworth, N. and Louat, N., "The origin of fatigue fracture in copper", *Phil. Mag.* **1**, 113-126 (1956).
60. Essmann, U., "Dislocation interactions in persistent slip bands and macroscopic properties of fatigued fcc metals", in *Basic Mechanisms in Fatigue of Metals,* edited by Lukás, P. and Polák, J. (Proc. of the Int. Colloquium, Elsevier, Amsterdam, NL (1988)), pp. 433-440.
61. Klesnil, M., Lukás, P. and Polák, J., "General Features of the Fatigue Process", in *Cyclic Deformation and Fatigue of Metals* (Materials Science Monographs, Vol. 78, Elsevier, (1993)), pp. 1-32.
62. Grosskreutz, J. C. and Mughrabi, H., "Description of the work-hardened structure at low temperature in cyclic deformation", in *Constitutive equations in plasticity* (The MIT Press, Cambridge, MA, (1975)), pp. 251-325.
63. Antonopoulos, J. G. and Winter, A. T., "Weak-beam study of dislocation structures in fatigued copper", *Phil. Mag.* **33**, 87-95 (1976).
64. Antonopoulos, J. G., Brown, L. M. and Winter, A. T., "Vacancy dipoles in fatigued copper", *Phil. Mag.* **34** (4), 549-563 (1976).
65. Backofen, W. A., "Formation of slip-band cracks in fatigue", in *Fracture,* edited by Averbach, B. L., Felbeck, D. K., Hahn, G. T. and Thomas, D. A. (Inter.Conf. on the Atomic Mechanisms of Fracture, The Technology Press of MIT, Cambridge (1959)), pp. 435-449.
66. Essmann, U. and Mughrabi, H., "Annihilation of dislocations during tensile and cyclic deformation and limits of dislocation densities", *Phil. Mag. A* **40** (6), 731-756 (1979).

67. Hunsche, A. and Neumann, P., "Quantitative measurement of persistent slip band profiles and crack initiation", *Acta Metall.* **34** (2), 207-217 (1986).
68. Finney, J. M. and Laird, C., "Strain localization in cyclic deformation of copper single crystals", *Phil. Mag.* **31**, 339-366 (1975).
69. Ackermann, F., Kubin, L. P., Lepinoux, J. and Mughrabi, H., "The dependence of dislocation microstructure on plastic strain amplitude in cyclically strained copper single crystals", *Acta Metall.* **32** (5), 715-725 (1984).
70. Feltner, C. E. and Laird, C., "Cyclic stress-strain response of fcc metals and alloys - II Dislocation structures and mechanisms", *Acta Metall.* **15**, 1633-1653 (1967).
71. Kayali, E. S. and Plumtree, A., "Stress-substructure relationships in cyclically and monotonically deformed wavy slip mode metals", *Metall. Trans. A* **13**, 1033-1041 (1982).
72. Holzwarth, U. and U., E., "Transformation of dislocation patterns in fatigued copper single crystals", *Mater. Sci. Eng. A* **164**, 206-210 (1993).
73. Lukás, P. and Klesnil, M., "Dislocation structures in fatigued Cu-Zn single crystals", *Phys. Stat. Sol.* **37**, 833-842 (1970).
74. Forsyth, P. J. E., "Exudation of material from slip bands at the surface of fatigued crystals of an aluminium-copper alloy", *Nature* **171**, 172-173 (1953).
75. Lin, H. and Ito, Y. M., "Mechanics of a fatigue crack nucleation mechanism", *J. Mech. Phys. Solids* **17**, 511-523 (1969).
76. Lin, T. H. and Lin, S. R., "Micromechanics theory of fatigue crack initiation applied to time-dependent fatigue mechanisms", in *Fatigue Mechanisms* (Special Technical Publication 675, ASTM, Philadelphia, PA, (1979)), pp. 707-728.
77. Tanaka, K. and Mura, T., "A dislocation model for fatigue crack initiation", *J. Appl. Mech.* **48**, 97-103 (1981).
78. Polák, J., "On the role of point defects in fatigue crack initiation", *Mater. Sci. Eng.* **92**, 71-82 (1987).
79. Essmann, U., Gösele, U. and Mughrabi, H., "A model of extrusions and intrusions in fatigued metals", *Phil. Mag. A* **44** (2), 405-426 (1981).
80. Johnson, E. W. and Johnson, H. H., "Imperfection density of fatigued and annealed copper via electrical-resistivity measurements", *Trans. Metall. Soc.* **233**, 1333-1339 (1965).
81. Polák, J., "The effect of intermediate annealing on the electrical resistivity and shear stress of fatigued copper", *Scripta Metall.* **4**, 761-764 (1970).

82. Differt, K., Essmann, U. and Mughrabi, H., "A model of extrusions and intrusions in fatigued metals, II. Surface roughening by random irreversible slip", *Phil. Mag. A* **54** (2), 237-258 (1986).
83. Basinski, Z. S. and Basinski, S. J., "Low amplitude fatigue of copper crystals from 4.2K to 350K", in *Strength of Metals and Alloys*, Vol. 1, edited by Kettunen, P. O., Lepistö, T. K. and Lehtonen, M. E. (Proceedings of the 8th International Conference (ICSMA 8), Pergamon Press, Oxford, UK (1988)), pp. 13-24.
84. Basinski, Z. S. and Basinski, S. J., "Copper single crystal PSB morphology between 4.2 and 350 K", *Acta Metall.* **37**, 3263 (1989).
85. Ma, B.-T. and Laird, C., "Overview of fatigue behavior in copper single crystals - I. Surface morphology and stage I crack initiation sites for tests at constant strain amplitude", *Acta Metall.* **37** (2), 325-336 (1989).
86. Ma, B.-T. and Laird, C., "Overview of fatigue behavior in copper single crystals - II. Population, size distribution and growth kinetics of stage I cracks for tests at constant strain amplitude", *Acta Metall.* **37** (2), 337-348 (1989).
87. Brown, L. M., "Dislocation substructures and the initiation of cracks by fatigue", *Metal Science* **11**, 315-320 (1977).
88. Brown, L. M., "Dislocations and the fatigue strength of metals", in *Dislocation modelling of physical systems*, edited by Ashby, M. F., Bullough, R., Hartley, C. S. and Hirth, J. P. (Proc. of the Int. Conf., Pergamon Press, Elmasford, N.Y. (1981)), pp. 51-69.
89. Polák, J., "Resistivity of fatigued copper single crystals.", *Mater. Sci. Eng.* **89**, 35-43 (1987).
90. Winter, A. T., "Dislocation structure in the interior of a fatigued copper polycrystal", *Acta Metall.* **28**, 963-964 (1980).
91. Rasmussen, K. V. and Pedersen, O. B., "Fatigue of copper polycrystals at low plastic strain amplitudes", *Acta Metall.* **28**, 1467-1478 (1980).
92. Winter, A. T., Pedersen, O. B. and Rasmussen, K. V., "Dislocation microstructures in fatigued copper polycrystals", *Acta Metall.* **29**, 735-748 (1981).
93. Mughrabi, H. and Wang, R., "Cyclic strain localization and fatigue crack initiation in persistent slip bands in face-centered cubic metals and single phase alloys", in *Defects and Fracture*, edited by Sih, G. C. and Zorski, H. (Proc. First Int. Symp. on Defects and Fracture, Martinus Nijhoff Publishers, The Hague (1982)), pp. 15-28.
94. Polák, J., Klesnil, M. and Lukás, P., "High cycle plastic stress - strain response of metals", *Mater. Sci. Eng.* **15**, 231-237 (1974).

95. Lukás, P. and Kunz, L., "Is there a plateau in the cyclic stress-strain curves of polycrystalline copper ?", *Mater. Sci. Eng.* **74**, L1-L5 (1985).
96. Agnew, S. R. and Weertman, J. R., "Cyclic softening of ultrafine grain copper", *Mater. Sci. Eng. A* **244**, 145-153 (1998).
97. Thompson, A. W. and Backofen, W. A., "The effect of grain size on fatigue", *Acta Metall.* **19**, 597-606 (1971).
98. Lukás, P. and Kunz, L., "Effect of Grain Size on the High Cycle Fatigue Behaviour of Polycrystalline Copper", *Mater. Sci. Eng.* **85**, 67-75 (1987).
99. Agnew, S. R., Vinogradov, A. Y., Hashimoto, S. and Weertman, J. R., "Overview of Fatigue Performance of Cu Processed by Severe Plastic Deformation", *J. Electronic Mater.* **28** (9), 1038-1044 (1999).
100. Mughrabi, H., "On the grain-size dependence of metal fatigue: outlook on the fatigue of ultrafine-grained metals", in *Investigations and Applications of Severe Plastic Deformation* (Kluwer Academic Publishers, (2000)), pp. 241-253.
101. Judelewicz, M., "Cyclic deformation of 100 µm thin polycrystalline copper foils", *Scripta Metall. Mater.* **29**, 1463-1466 (1993).
102. Judelewicz, M., Künzi, H. U., Merk, N. and Ilschner, B., "Microstructural development during fatigue of copper foils 20-100 µm thick", *Mater. Sci. Eng. A* **186**, 135-142 (1994).
103. Hong, S. and Weil, R., "Low cycle fatigue of thin copper foils", *Thin Solid Films* **283**, 175-181 (1996).
104. Read, D. T. and Dally, J. W., "Fatigue of microlithographically-patterned free-standing aluminum thin films under axial stresses", *J. Electronic Packaging* **117**, 1-6 (1995).
105. Read, D. T., "Tension-tension fatigue of copper thin films", *Int. J. Fatigue* **20** (3), 203-209 (1998).
106. Cornella, G., "Monotonic and cyclic testing of thin film materials for MEMS applications", *PhD Dissertation* (Dept. Materials Science and Engineering, Stanford University (1999)).
107. Hommel, M., Kraft, O., Baker, S. P. and Arzt, E., "Micro-Tensile and Fatigue Testing of Copper Thin Films on Substrates", in *Materials Science of Microelectromechanical Systems (MEMS) Devices*, edited by Heuer, A. H. and Jacobs, S. J. (Mater. Res. Soc. Symp. Proc. Vol. 546, Materials Research Society, Warrendale, PA (1999)), pp. 133-138.
108. Kraft, O., Schwaiger, R. and Wellner, P., "Fatigue in Thin Films: Lifetime and Damage Formation", to be published in *Mater. Sci. Eng. A.*

109. Merchant, H. D., Minor, M. G. and Liu, Y. L., "Mechanical Fatigue of Thin Copper Foil", *J. Electronic Mater.* **28** (9), 998-1007 (1999).

110. Oshida, Y. and Chen, P. C., "High and Low-Cycle Fatigue Damage Evaluation of Multilayer Thin Film Structure", *J. Electronic Packaging* **113**, 58-62 (1991).

111. Schwaiger, R. and Kraft, O., "High Cycle Fatigue of Thin Silver Films Investigated by Dynamic Microbeam Deflection", *Scripta Mater.* **41** (8), 823-829 (1999).

112. Hofbeck, R., Hausmann, K., Ilschner, B. and Künzi, H. U., "Fatigue of very thin copper and gold wires", *Scripta Metall.* **20**, 1601-1605 (1986).

113. Vinci, R. P., Cornella, G. and Bravman, J. C., "Anelastic contributions to the behavior of freestanding Al thin films", in *Stress Induced Phenomena in Metallization*, edited by Kraft, O., Arzt, E., Volkert, C. A., Ho, P. S. and Okabayashi, H. (5th Int. Workshop, American Institute of Physics, Melville, N.Y. (1999)), pp. 241-248.

114. Hadrboletz, A., Weiss, B. and Khatibi, G., "Fatigue and fracture properties of thin metallic foils", *Int. J. Fracture* **107**, 307/327 (2001).

Chapter 3 Size Effects in the Fatigue Behavior of Thin Silver Films

3.1 Introduction

Thin metal films are important parts in modern miniaturized electronic and mechanical devices. Film materials are usually chosen because of their electronic, magnetic, or optical properties, but the mechanical ones are frequently found to be the limiting factor in application. The films must be able to withstand the large stresses created during the deposition process, but also the repeated stresses due to mechanical vibrations and temperature changes during operation, or the high operating frequencies that are typical for mechanical small-scale devices. It is obvious that the deformation mechanisms in thin films are influenced by the presence of interfaces and free surfaces. Due to the small and continuously decreasing dimensions these deformation mechanisms occur on a scale not yet completely understood. As a result, many laws governing the deformation of bulk material do not apply to the case of thin films.

On one hand, the microstructure, which is decisive for mechanical behavior, differs from bulk microstructures. Typical microstructures in thin film systems include textures and fine grains. In polycrystalline metal films, for instance, normal grain growth stagnates when the grain size is comparable to the thickness; moreover, many thin films can be regarded as a two-dimensional array of grains, as the grains are often columnar and extend through the film thickness.

On the other hand, there is a direct influence of the film thickness on the mechanical behavior. For instance, much higher yield stresses are predicted and experimentally found for coarse-grained Al films [1], an order of magnitude higher than for bulk Al of the same purity.

Generally, the introduction of constraints, such as interfaces, surfaces or grain boundaries, act to restrict dislocation formation and motion, resulting in very high strengths at small scales. Models for the constraint of dislocation motion within films with thicknesses up to a micron suggest yield strengths which scale inversely with the film thickness [2], [3] and/or grain size [4] and this predicted trend has been generally borne out [5]. However, the experimentally found yield stresses are often much higher than predicted by theory [5]-[7].

It can further be expected that in fatigue loading the local accumulation of plastic strain will also be affected by microstructure and thickness of the film: dislocation structures characteristic for bulk fatigued metals, such as veins, slip bands, and cell structures typically

extend at least over several micrometers. For (sub)micron dimensions the fatigue behavior is likely to be different than in bulk material as the volume of material available is too small to allow the formation of these typical dislocation structures.

The fatigue properties of bulk metals have been thoroughly investigated. It is now well established that local plastic strains are necessary for the inducement of fatigue failure in ductile bulk crystals. However, experimental data on thin film fatigue and size effects are contradictory and not conclusive. Fatigue studies on thin copper foils within the thickness range of 18 – 100 µm have been reported [8]-[11]. Judelewicz *et al*. [8] found thickness dependent behavior to the effect that thinner specimens sustained higher cycle numbers at the same stress amplitude, whereas Hong and Weil [9] reported only a minor thickness effect; Merchant *et al*. [10] found the fatigue behavior of the tested foils to be comparable to bulk polycrystalline copper. A detailed report of the fatigue behavior of thin metal films with thicknesses smaller than 1 µm as well as the influence of the film thickness has not yet been presented.

In the work reported here the cyclic deformation of Ag films having thicknesses between 0.2 and 1.5 µm on a silicon dioxide substrate was studied. Bilayer cantilever microbeams were cyclically deflected by a nanoindenter; the fatigue life was investigated with respect to the film thickness and the loading conditions. For a detailed interpretation of the experiments, the stress-strain behavior of the film material was investigated by monotonic loading. Finite element calculations were performed to correlate the load-deflection data of the beams with stresses and strains in the film material. Both dimensional and microstructural factors were found to play a role for the fatigue endurance of these thin films.

3.2 Experimental details

3.2.1 Sample preparation and characterization

Silver films were sputter-deposited onto microfabricated SiO_2 cantilever beams. For the preparation of the beams, SiO_2 layers were grown on (100) Si wafers by wet thermal oxidation at 1100 °C for 18 h. The oxide film thickness was measured by ellipsometry to be 2.84 ± 0.05 µm. The films were then patterned using standard photolithography and etching processes. The final structures consisted of SiO_2 cantilever beams extending over an open trench bounded by four {111} walls. The preparation method has been described in more detail in Ref. [12]. The cross-section of the SiO_2 beams was not perfectly rectangular, but trapezoidal with a width of 19 µm and 21 µm at the surface and bottom, respectively, as determined by focused ion beam (*FIB*) microscopy (FEI 200). The lengths of the beams varied

between 50 and 100 μm. The thickness of the SiO_2 after the final etching was measured to be 2.83 ± 0.05 μm. The supporting silicon substrate was not etched back beyond the fixed ends of the beams. The cantilever beams were fabricated at the Center of Integrated Systems at Stanford University by Dr. S. Hong.

The metal films with thicknesses ranging from 0.2 to 1.5 μm were then deposited onto the patterned microbeam specimen by magnetron sputtering under UHV conditions (base pressure of $6x10^{-7}$ Pa, sputter machine: DAF) at a rate of 77 nm/s. The film thickness was adjusted by the duration of sputtering. The deposition was performed at a power of 100 W and Ar pressure of 4.2×10^{-1} Pa. During deposition the substrate was clamped to a plate that was cooled by liquid nitrogen and electrically grounded. Then the samples were annealed for 22 h at a temperature of 373 K without breaking the vacuum. Finally, the Ag film was removed by ion beam milling, using the *FIB*, where the indenter tip was to contact the beam to avoid penetration into the film material.

The microstructure of the Ag films has been extensively characterized: The texture was investigated by standard X-ray diffraction (*XRD*) methods [13], using a 4-circle texture goniometer with Cu K_α radiation. Local information on grain orientation was obtained from electron backscatter diffraction (*EBSD*), using a LEO 438VP scanning electron microscope and Orientation Imaging Microscopy (*OIM*) software (TSL, Utah, USA). The residual stresses in the Ag films were determined by *XRD* measuring the elastic strains using {422} planes in <111>-oriented grains. The elastic strains were determined through measurements of interplanar spacings as a function of $\sin^2\psi$, where ψ is the angle between the surface normal and the normal of the diffracting planes. This method has been described in detail in Ref. [14].

The grain structure of the films was characterized by *FIB* microscopy. Digitized *FIB* images were evaluated using a Quantimet 500 (Zeiss, Oberkochen, Germany). The *FIB* is an appropriate means to image grains without special sample preparation. The grain contrast depends on the secondary electron yield due to ion channeling by the crystal lattice, which depends on the orientation of individual grains with respect to the incident beam. This contrast mechanism was first described by Levi-Setti *et al.* [15]. A series of four images of a surface area for each film thickness were taken; the respective tilt angles of the sample were 0°, 15°, 20°, and 25°; at just a single tilt angle adjacent grains may still have the same contrast, especially in a highly textured film. The distortion due to the sample tilt was corrected by the *FIB* software. The grain boundaries identified in these four images were copied onto a transparency, which was digitized and analyzed utilizing the Quantimet. Straight boundaries

identified as twin boundaries were not taken into account. The grain size was defined as the diameter d of an equivalent circular grain area A:

$$d = 2 \cdot \sqrt{\frac{A}{\pi}} \qquad (3.1).$$

The microstructure through the depth of the film was investigated by preparing cross-sections through the film using the ion-milling mode of the *FIB* and subsequent imaging. The thickness of the films was determined in the same way.

3.2.2 Microbeam deflection

Microbeam deflection experiments using a nanoindenter are well established for determining yield stress and elastic stiffness in small volumes of materials [12], [16], [17]. However, the application of this technique to fatigue testing of thin films requires some special considerations as described below. The bilayer microbeams were monotonically and cyclically tested using a load- and depth-sensing indentation instrument (Nano Indenter ® II, MTS Systems Corp.) that is equipped with the *Continuous Stiffness Measurement* (*CSM*) option and has been described in Refs. [18], [19].

Monotonic testing and finite element modeling

Microbeam deflection and finite element analysis (*FEA*) were combined to obtain information on the monotonic stress-strain behavior of film and substrate from experimentally determined load-deflection curves. A schematic of the bilayer beam deflection experiment is shown in Fig. 3.1(a). The indenter tip approached the beam at a constant velocity between 6 and 10 nm/s. The slope of the load-displacement data collected in this part of the experiment represents the spring constant of the suspending springs that support the indenter shaft. The stiffness of the indenter springs varies with temperature and mechanical history. Therefore, it was determined by a linear least-squares fit to the data before the beam was contacted for each experiment. At contact, the load rate was set to 60 µN/s and the beam was deflected to at least 5 µm. Load and deflection data were recorded continuously during each experiment. A 90° wedge-shaped diamond tip was used, with a wedge length of 10 µm. For every film thickness three beams were tested at varying lengths between 30 and 50 µm. The penetration of the tip into the SiO_2 (< 50 nm) was neglected.

For *FEA* a commercial finite element code, ANSYS 5.6 (Ansys, Inc., Pennsylvania), was used. The geometrical *FE* model is schematically shown in Fig. 3.1(b). The beam is attached to a Si substrate (see Fig. 3.1(a)), which results in an additional compliance at the beam support. In the two-dimensional *FE* model the compliance of the beam support was accounted

for by constraining the nodal displacements and rotations only at the SiO_2-Si interface, as schematically shown in Fig. 3.1(b). A micrograph of a beam array is shown in Fig. 3.1(c).

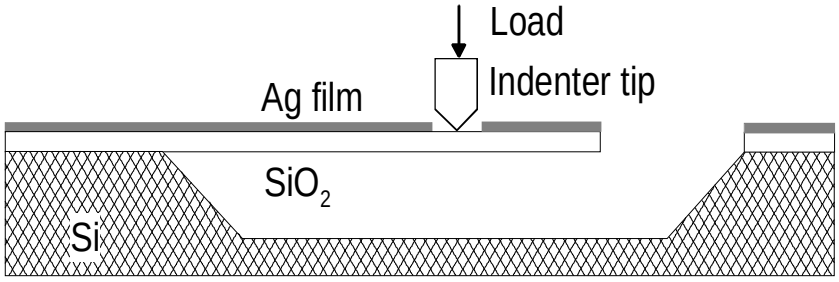

(a)

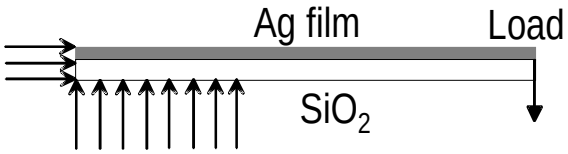

(b)

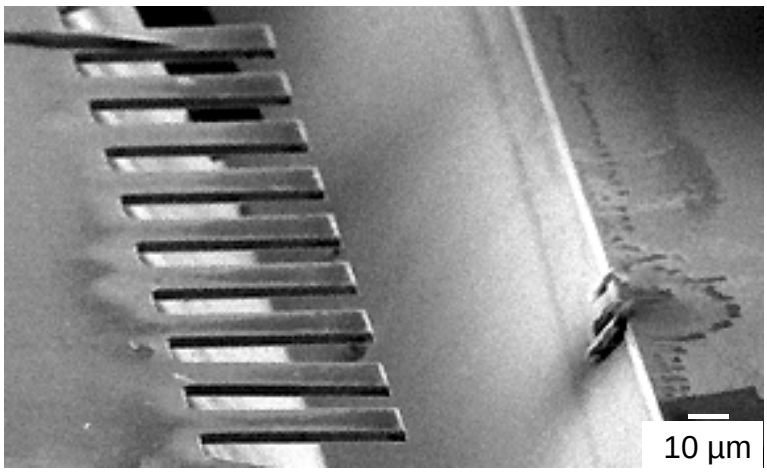

(c)

Fig. 3.1: Schematic of the beam deflection experiment. (a) Edge view: The bilayer Ag-SiO_2 beam extends over an etch pit in the underlying Si. The indenter tip is used to deflect the beam. (b) *FE* model of the bilayer beam. The Si support is accounted for by constraining the nodal displacements and rotations at the bottom of the beam along a distance of 17 µm from the fixed end, as symbolized by arrows. (c) Micrograph of a beam array.

The *FE* model was constructed from eight-node quadrilateral elements. The elastic constants used in the calculations were assumed to be isotropic and are summarized in Table 3.1. The SiO_2 was modeled as a perfectly elastic solid, whereas the mechanical behavior of the

metal film was described by a bilinear stress-strain relation using a model with a *von Mises* yield surface and associated plastic flow. The interfaces between the metal and SiO_2 were assumed to be perfectly mechanically bonded at all times during the numerical experiment. Fig. 3.2 defines terms and illustrates the stress-strain parametrization for Ag.

Material	E [GPa]	ν
SiO_2	70 [20]	0.16 [21]
Ag	71 [22]	0.38 [23]

Table 3.1: Materials parameters for *FEA*

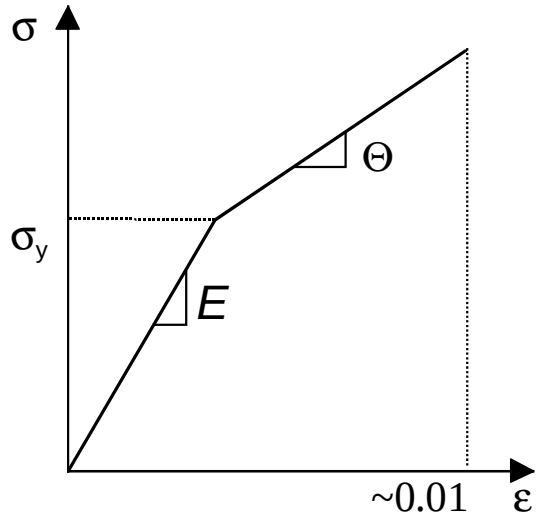

Fig. 3.2: Bilinear stress-strain relation as used for the Ag film. The initial slope is defined by Young's modulus E, the deviation from linearity by the yield stress σ_y, and the slope of the curve for $\sigma > \sigma_y$ by the work hardening rate Θ.

The procedure for determining the yield stress σ_y and the work hardening rate Θ of the metal film was the following: First, the lever length was varied in the simulation until the elastic part of the calculated load-deflection curve matched the elastic part of the experimental one. Then, values for σ_y and Θ were estimated and modified to obtain agreement between modeled and experimental curves, which were calculated to a maximum strain of ~0.01 in the film at the beam surface. For all film thicknesses the parameters σ_y and Θ were determined for three experimentally obtained curves and averaged to be used in further calculations.

Cyclic deformation

The indentation system has the ability to superimpose an oscillation on the monotonic force signal and measure the displacement response of the sample at the same frequency. Details of this dynamic technique have been described in Ref. [18].

The beams were deflected at a distance of 30 to 50 μm from the support. A sinusoidal force oscillation at 45 Hz with different amplitudes was superimposed on the static force signal during the beam deflection experiments. The experiments were performed using the following load-time sequence: The indenter was loaded at a constant load rate. The static peak load, i.e. the mean load of the fatigue cycle, was held constant for a period of 23.3 h and then removed at a rate of 300 μN/s. Different mean loads were applied ranging from 40 to 800 μN. The respective loading rates were adjusted in proportion to the load to make sure that the loading segments of each experiment required approximately the same time. The stiffness of the suspending springs was determined as described above. Due to damping in the indentation system (see Ref. [18]) only a small fraction of the input amplitude of the oscillating signal is applied to the beam; the input force amplitude was adjusted to obtain an oscillating displacement with an amplitude of 168 to 295 nm during the hold segment. The displacement amplitude was constant within ±3 % throughout the tests. The input load amplitude varied between 300 and 460 μN.

The displacement of the tip, the displacement amplitude, as well as the phase difference between the oscillating displacement and the force signal were recorded throughout the tests. The absolute displacement of the indenter tip due to the static load during the hold was not considered in the interpretation of the results, as it was influenced by thermal expansion in the system. Temperature drift is a well-known problem related to the displacement-sensing system in particular for tests made over a long period of time. However, slow temperature changes do not influence the dynamic displacement measurement.

During the experiment at constant mean load, the stiffness of the beams is determined as described in detail in [24]. Fatigue damage was seen as a decrease of the beam stiffness. 3.8×10^6 cycles were applied as determined from the elapsed time. The tests were conducted at room temperature and atmospheric pressure.

Using the values for σ_y and Θ obtained for each individual film thickness from the monotonic tests, *FEA* was applied to calculate stress amplitudes and mean stresses for the fatigue tests. The maximum values, which occurred at the film surface close to the beam support, will be denoted by σ_a and σ_m, respectively.

3.3 Results

3.3.1 Characterization of the microstructure

The microstructural parameters for the Ag films are summarized in Table 3.2. The film thickness was examined and verified to be equal to the nominal value with an accuracy of 10 %. The grain size distributions of the films were lognormal with a median grain size of about 1 µm for all samples. The density of twins was high in all films investigated. Except for the 1.5 µm thick ones the films had a columnar grain structure (all grain boundaries extending through the thickness of the film). Two fiber texture components, (111) and (100) fiber orientations, have been observed. The fraction of randomly oriented grains was negligible. Increasing the film thickness leads to an increase of the fraction of (100) fiber oriented grains, the fraction of random orientations was not influenced by the thickness. The residual stresses determined by *XRD* were between 26 and 41 MPa as measured in <111>-oriented grains.

Film thickness	d_{50} [µm]	s_d [µm]	Number of grains	Residual stress [MPa]
0.2 µm	0.92	0.46	223	26
0.4 µm	0.93	0.44	395	37
0.6 µm	0.84	0.51	244	27
0.8 µm	0.91	0.46	303	30
1.0 µm	0.98	0.41	180	41
1.5 µm	1.01	0.66	297	43

Table 3.2: Film parameters (with d_{50} and s_d as the median grain size and the standard deviation, respectively).

3.3.2 Monotonic loading and *FEA*

In Fig. 3.3(a) experimental and calculated load-deflection curves of two beams with a 0.6 µm thick Ag film are shown. The beams were deflected at a length of 42.5 and 44.5 µm, respectively. At displacements smaller than approximately 2000 nm, the load-deflection curves are linear; the deformation of the beams is elastic and can be described by linear elastic beam theory (see for example [25]). As the deflection continues, the slope of the curves starts to decrease; the Ag film begins to deform plastically and simple beam bending equations no longer apply. The load-deflection curves as calculated by *FEA*, are shown as solid lines in Fig. 3.3 (a). In contrast, the load-deflection curve of a bare SiO_2 beam, which is also shown in Fig. 3.3 (a), shows no deviation from linearity indicating that the SiO_2 behaves completely elastic in this strain regime, hence justifying the assumption in the *FEA*. Plastic deformation of the

film starts at the fixed end and at the surface of the beam, where the maximum strain is present. Fig. 3.3(b) shows the distribution of the plastic strain as calculated by *FE*. The maximum strain is achieved at the film surface; a strain gradient through the thickness and along the beam axis exists. The stress as well as the total strain along the beam axis are not constant; they are highest close to the beam support and decrease in the direction of the contact point. Calculated stress and strain along the beam axis at the film surface are shown in Fig. 3.3(c). For x<0 the stress decreases gradually due to the compliant support.

The average values for σ_y and Θ for all film thicknesses, each obtained from three monotonic beam deflection experiments, are summarized in Fig. 3.4(a) and (b), respectively. In Fig. 3.4(c) and (d) σ_y and Θ are plotted versus the reciprocal thickness.

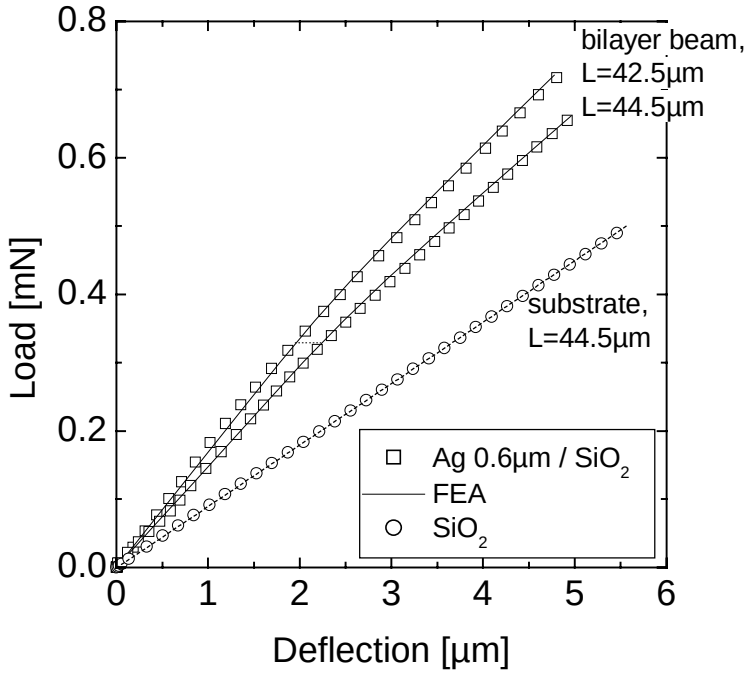

(a)

Fig. 3.3: (a) Monotonic loading, experimental and calculated load-deflection curves for a 0.6 µm thick Ag film on SiO_2. The experimental curves of the bilayer beams are shown as square symbols, the deflection of the substrate beam is denoted by circles. The calculated curves are shown as solid lines. In *FEA* Young's modulus and Poisson's ratio for SiO_2 and Ag were 70 GPa and 0.16, and 71 GPa and 0.38, respectively. The yield stress σ_y and work hardening rate Θ were determined to be 270 MPa and 28 GPa, respectively.

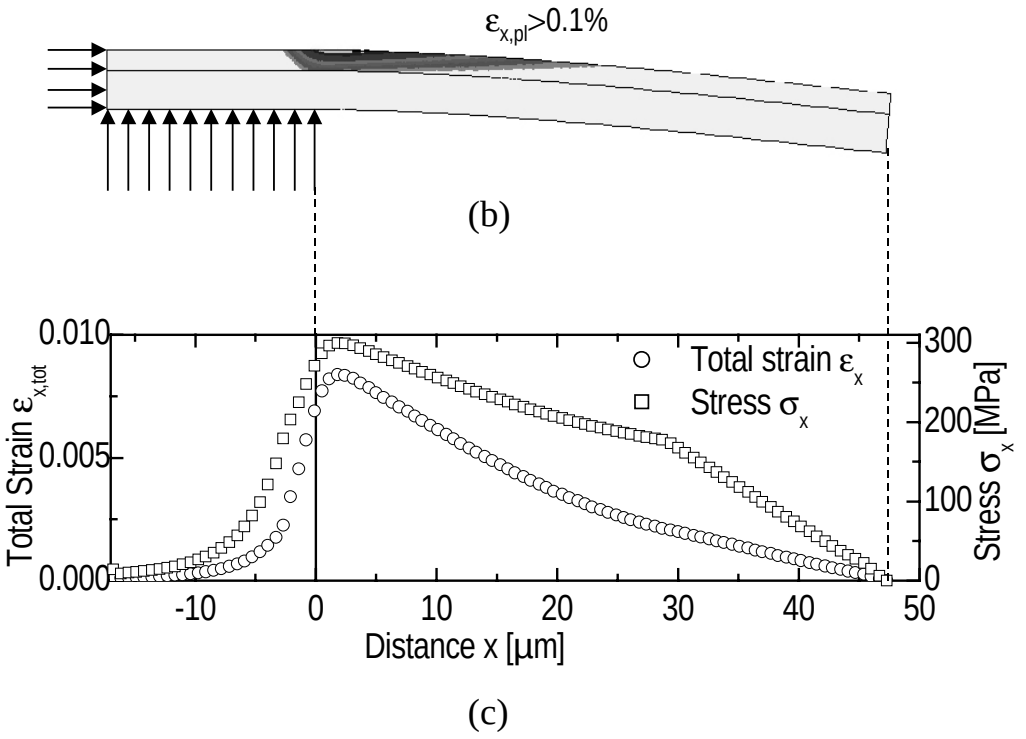

Fig. 3.3 (continued): (b) *FEA*, deformed shape of a bilayer beam. The distribution of the plastic strain is shown. The substrate behaves elastically, whereas in the film plastic deformation occurs. There is a strain gradient along the beam length and through the film thickness with a maximum at the film surface. (c) Stress and total strain component in the direction of the beam as a function of the position along the beam axis at the film surface.

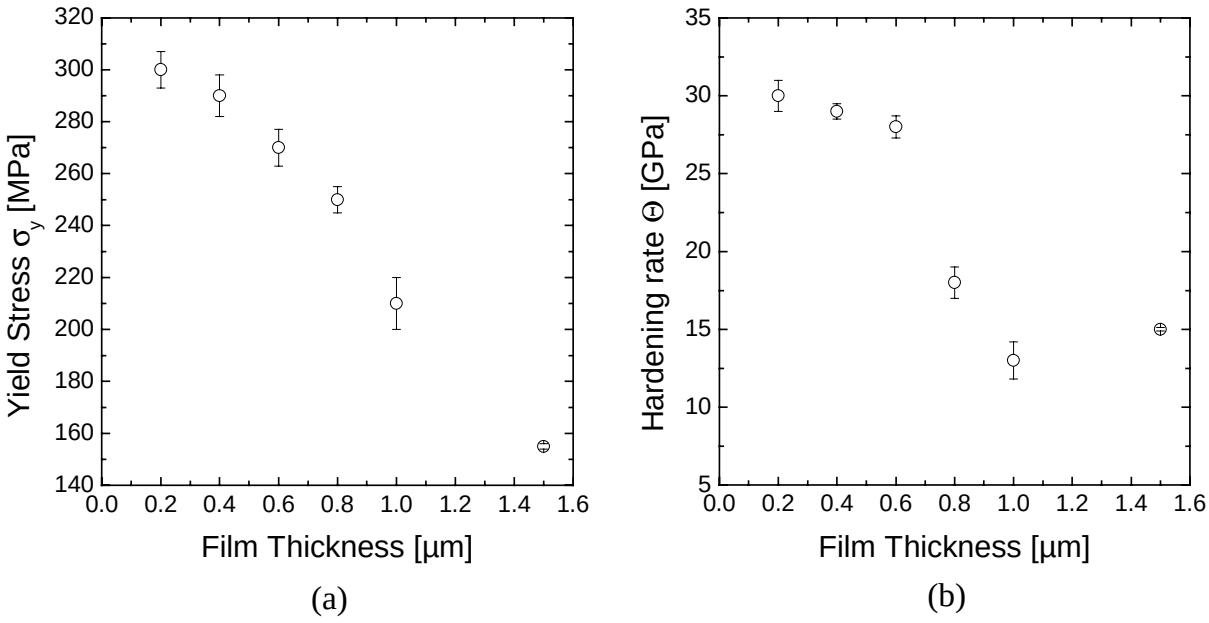

Fig.3.4 (continued next page)

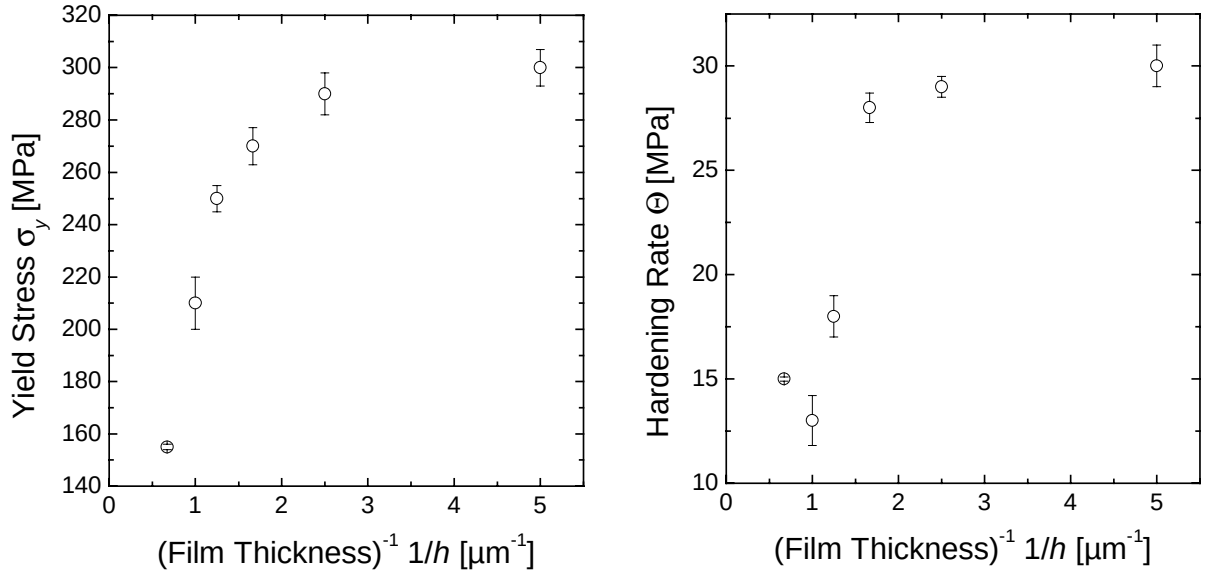

Fig. 3.4: (a) σ_y and (b) Θ versus the film thickness. (c) σ_y and (d) Θ versus the reciprocal film thickness The average of the numerical simulations of three experiments per film thickness is shown.

3.3.3 Cyclic deformation

Fatigue Tests

The dynamic beam stiffness was shown to be an appropriate means for indicating fatigue damage [24]. Fig. 3.5(a) compares stiffness curves measured dynamically for films with a thickness of 0.2, 0.4, 0.6, 0.8, 1.0, and 1.5 µm fatigued with stress amplitudes σ_a that were approximately the same in all tests. In the following, stated mean stresses and stress amplitudes correspond to the largest stresses occurring in the film, i.e. the stress component in the direction of the beam axis at the surface of the Ag film close to the beam support as determined by *FEA*. Note that the initial stiffness of the beams depends on the thickness of the Ag film as well as on the lever length that was not constant in these tests. The mean stress σ_m varied according to Table 3.3, and a number of 3.8×10^6 force cycles was applied. For films with a thickness ≤ 0.8 µm, the stiffness was constant throughout the experiment. The stiffnesses of the 1.0 and 1.5 µm thick films were constant up to 8.9×10^5 cycles and 7.5×10^5 cycles, respectively, then a significant decrease was observed. The stiffness decrease suggests the onset of damage formation; the number N_d of cycles to stiffness decrease was defined according to the following procedure: Constant slope regions of the stiffness curves were fitted by straight lines, the intersection of which then defined N_d. This is illustrated in Fig. 3.5(b) for the case of the 1.5 µm thick film. As discussed below and also in Refs. [24] and

[26], microscopical damage analyses confirmed that this decrease in stiffness is associated with the formation of fatigue damage such as extrusions, cracks, and voids.

Film thickness [µm]	σ_a [MPa]	σ_m [MPa]	N_d
0.2	53	200	$>3.8x10^6$
0.4	58	340	$>3.8x10^6$
0.6	50	350	$>3.8x10^6$
0.8	54	283	$>3.8x10^6$
1.0	54	265	$8.9x10^5$
1.5	57	255	$7.5x10^5$

Table 3.3: Summary of experimental data. N_d denotes the number of cycles to damage formation, σ_a the stress amplitude, and σ_m the mean stress.

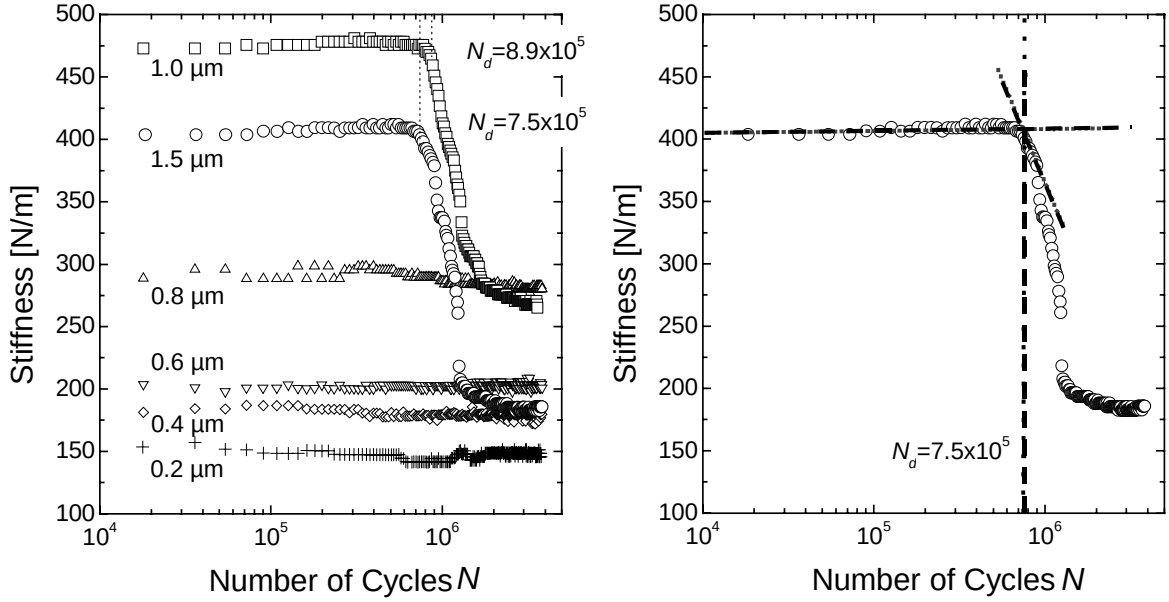

Fig. 3.5: (a) Stiffness at a stress amplitude σ_a~54 MPa (see Table 3.3) and a mean stress σ_m varying according to Table 3.3 over a period of 3.8 x 10^6 cycles. Bilayer beams with 1.5, 1.0, 0.8, 0.6, 0.4, and 0.2 µm thick films were tested; the lever lengths were 46, 44.5, 42.5, 43.3, 41, and 40 µm, respectively. (b) Determination of the number N_d of cycles to stiffness decrease.

In Table 3.4 experimental parameters, i.e. σ_a and σ_m, as well as the values for N_d obtained from fatigue tests of beams with a 0.6 µm thick Ag film are summarized. At a stress amplitude of 44 and 50 MPa no stiffness decrease occurred within 3.8 x 10^6 cycles; for the damaged beams σ_a was between 71 and 85 MPa. The mean stress σ_m was between 182 and 520 MPa. The results obtained for this film thickness are typical for the films investigated: under less

severe testing conditions, i.e. small σ_a, no stiffness decrease was observed within the applied number of cycles of 3.8×10^6. Fig. 3.6 shows the mean stress σ_m versus the number N_d of cycles to stiffness decrease for σ_a=78±7 MPa for the 0.6 µm thick film; the respective experimental results are summarized in Table 3.4. At high mean stresses the films endured fewer cycles than at lower ones.

Ag 0.6 µm	σ_a [MPa]	σ_m [MPa]	N_d
	44	520	*>3.8 x 10^6*
	50	350	*>3.8 x 10^6*
	71	160	4.68×10^5
	76	254	7.21×10^4
	77	273	4.51×10^4
	78	167	1.80×10^5
	78	261	4.96×10^4
	83	288	5.4×10^4
	84	191	1.62×10^5
	85	182	1.08×10^5

Table 3.4: Summary of experimental data performed on 0.6 µm thick Ag films. σ_a denotes the stress amplitude, σ_m the mean stress, and N_d the number of cycles to stiffness decrease.

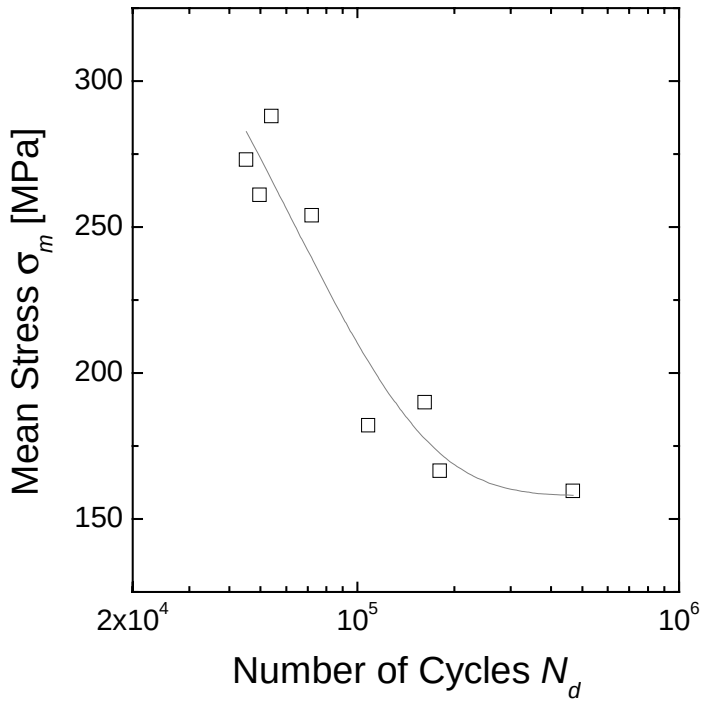

Fig. 3.6: Mean stress σ_m vs. the number N_d of cycles to stiffness decrease for experiments performed on beams with a 0.6 µm thick Ag film (compare Table 3.4).

All fatigue tests are summarized in Fig. 3.7, which includes tests on samples with different film thicknesses at various mean stress levels and stress amplitudes. The stress amplitude is plotted versus the film thickness. It should be noted that the mean stresses were not the same for all tests and between 126 and 600 MPa. Amplitudes that resulted in a stiffness decrease are denoted by open symbols, those leading to no stiffness decrease within 3.8×10^6 by crosshairs. For every film thickness, there is a critical stress amplitude below which the films were not damaged within the applied number of cycles irrespective of the applied mean stress. Increasing mean stress was observed to reduce the number of cycles to stiffness decrease (compare Fig. 3.6), but did not influence the critical stress amplitude. At $\sigma_a = 55$ MPa the 1.5 µm thick film was damaged, whereas the thinner films were intact; to induce fatigue damage in the 0.2 µm thick films a stress amplitude twice as high as in case of the thicker films was required. In the case of the 1.5 µm thick film, all experiments were performed at stress amplitudes at which fatigue damage occurred.

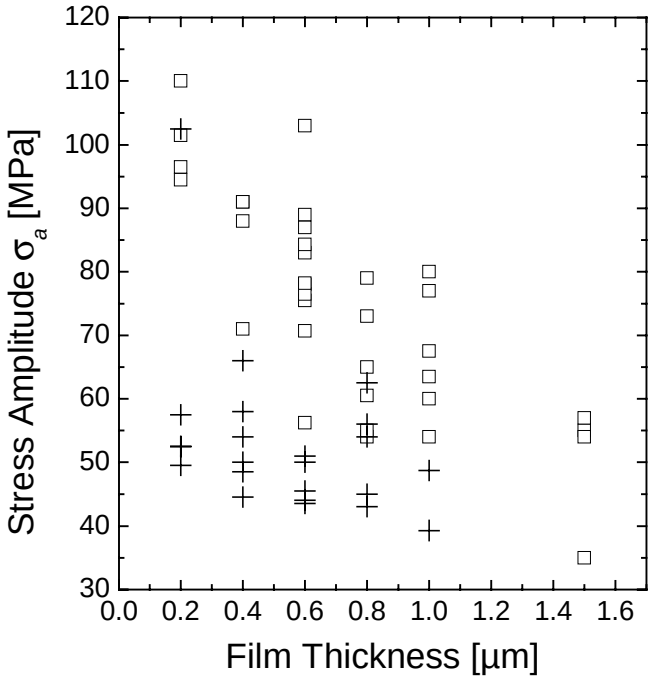

Fig. 3.7: Stress amplitude vs. film thickness. Beams that were damaged within 3.8×10^6 cycles are denoted by open symbols, those that were not damaged by crosshairs.

Damage analysis

A typical example of such fatigue damage is given in Fig. 3.8, which shows a micrograph of the surface damage of a 1.5 µm thick Ag film after 3.8 x 10^6 cycles (Fig. 3.8(a)). The failure process, i.e. the stiffness decrease, started at 7.5 x 10^5 cycles (see Table 3.3). The decrease of the beam stiffness was related to the formation of voids at the film-substrate interface and the formation of extrusions and cracks at the film surface. Fatigue damage in the beam samples investigated is generally restricted to a small area of the film close to the beam support, where the highest strains occur. At a higher magnification in Fig. 3.8(b) the surface damage is seen as extrusions in individual grains. In addition, there are cracks along the grain boundaries as well as cracks in extruded grains (ic and tc, respectively, in Fig. 3.8(b)). The slip traces on the surface are not generally uniformely distributed within one grain, some parts of extruded grains may remain undamaged.

In Fig. 3.8(c) a cross-section of an extrusion is shown. The position of the cross-section is indicated in Fig. 3.8(a). An irregularly shaped void extends from the substrate towards the film surface. There are also small voids close to the film-substrate interface. The height of the extrusion is comparable to the thickness of the film.

In Fig. 3.9(a)-(d), the fatigue damage of films with different thicknesses is shown. At the surface of the 0.8 µm thick film, large extrusions were observed over a wide region of the film similar to the ones in the 1.5 µm thick film (compare Fig. 3.8(a) and Fig. 3.9(a)). In case of thinner films, the damaged regions were fewer and smaller, e.g. at the surface of the 0.2 µm thick film only isolated extrusions were found (compare Fig. 3.9(d)). In all films, however, intergranular cracks span across the entire beam.

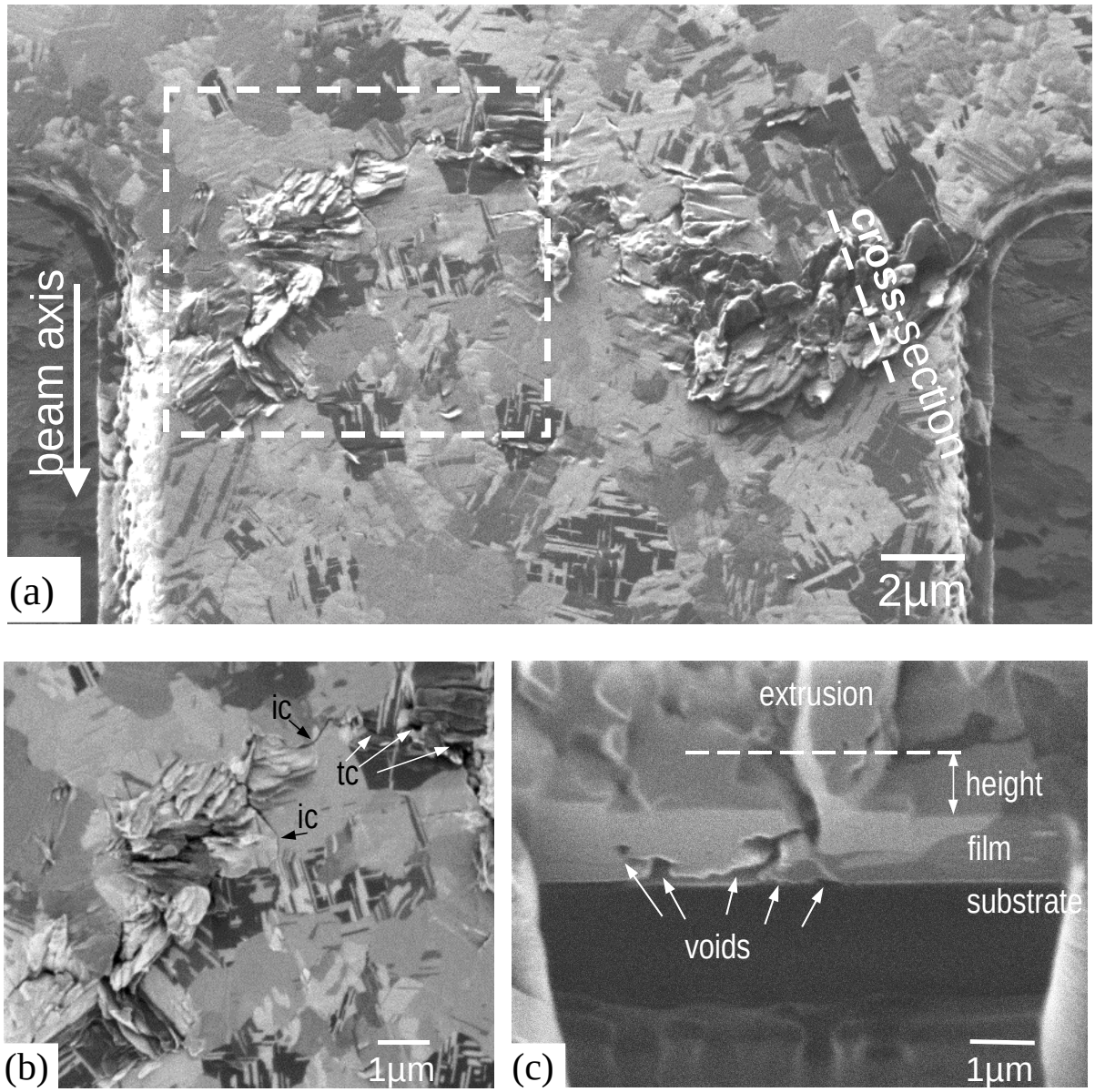

Fig. 3.8: Fatigue damage of a 1.5 µm Ag film. (a) Surface damage after 3.8 x 10^6 cycles at σ_a=57 MPa and σ_m=255 MPa. The assigned part of the sample is shown at higher magnification in (b), the position of a cross-section is indicated. (b) Extrusions, intergranular, as well as transgranular cracks along slip traces (marked by ic and tc, respectively) were observed. (c) Cross-section produced by focused ion beam milling. The tilt angle of the sample is 45°. Voids and extrusions are tagged.

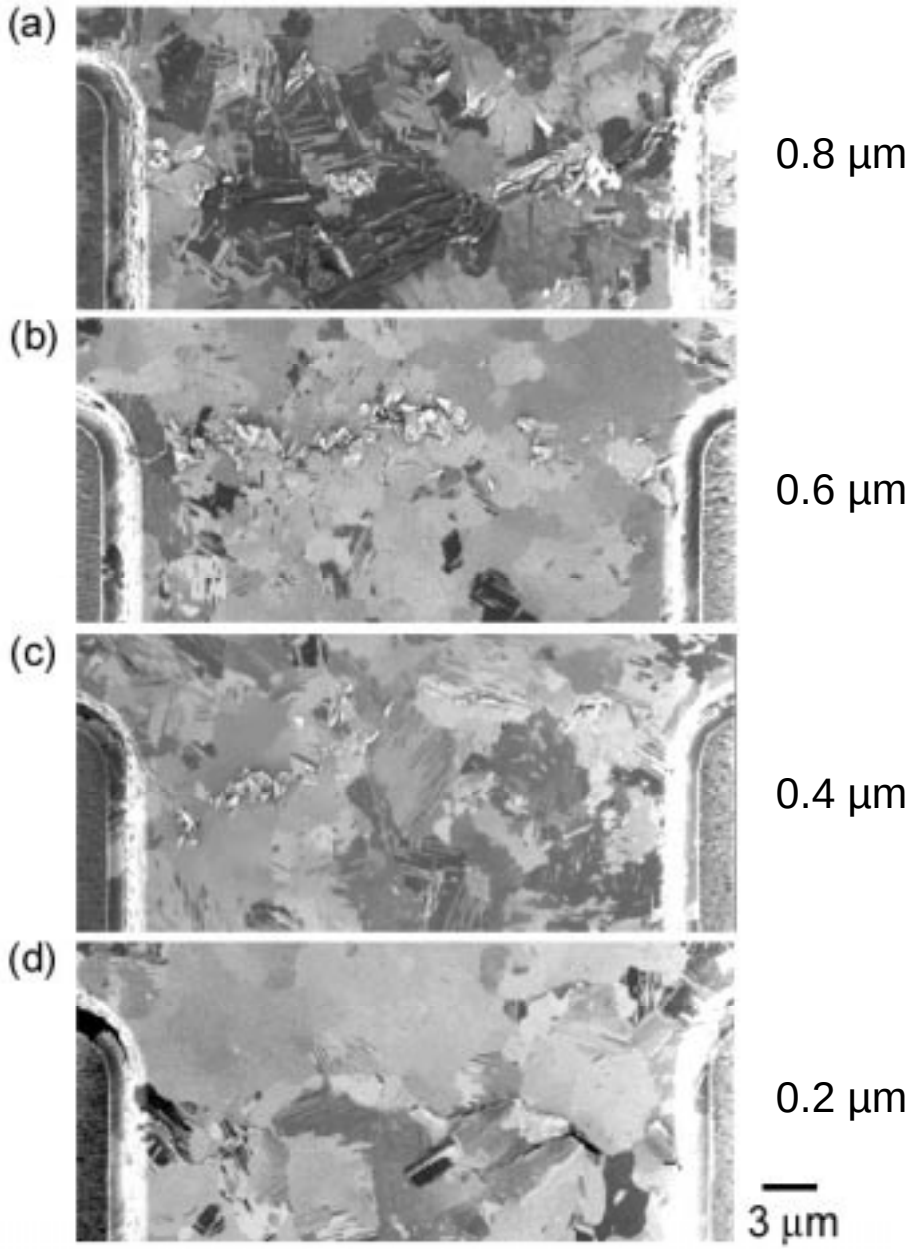

Fig. 3.9: (a)-(d) Fatigue damage of different film thicknesses. Note, that σ_a was higher for the thinner films: (a) 0.8 µm thick film, σ_a=62 MPa, (b) 0.6 µm thick film, σ_a=90 MPa, (c) the 0.4 µm thick film, σ_a=91 MPa, and (d) 0.2 µm thick film σ_a=110 MPa.

Furthermore, it was found that only certain grains in the damage region showed extrusions. The influence of the grain orientation on the formation of extrusions was investigated by electron backscatter diffraction (*EBSD*). The grain orientations of about 100 grains in the

respective region of fatigued beams with a film thickness of 0.8 µm were recorded. These orientations are marked in the inverse pole figure shown in Fig. 3.10., which shows that mainly two texture components, (111)- and (100)-oriented grains, are present. The orientations of grains that were not damaged are denoted by crosshairs, the other orientations by square symbols. It shows that the (111) grains were for the most part not damaged, whereas more than half of the (100)-oriented grains had extrusions. *EBSD* information was not available for the thinnest films, but from the *FIB* micrographs in Fig. 3.9 we conclude that the few extrusions found are located in grains with a dark contrast, which is typical for (100) grains [27].

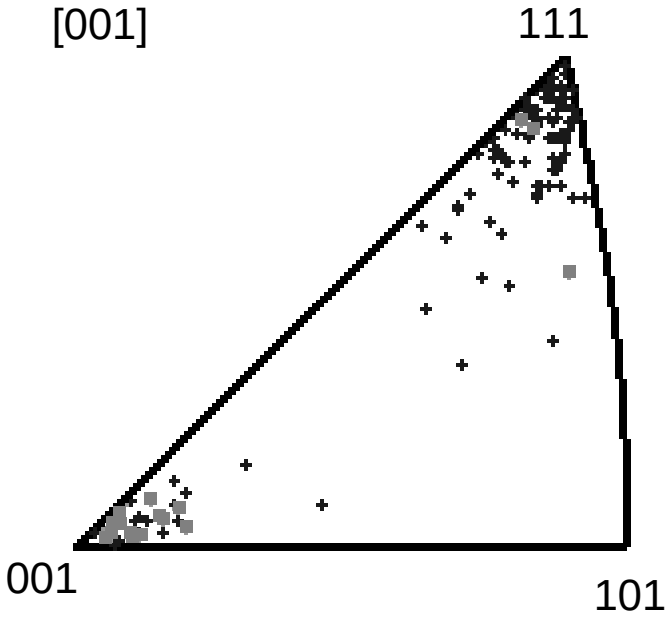

Fig. 3.10: Inverse pole-figure showing the orientation of grains in the damage region of beam samples with a 0.8 µm thick films tested at various stress amplitudes and mean stresses. Extruded grains are denoted by square symbols, grains that remained intact by crosshairs.

3.4 Discussion

The main issues to be discussed below are the microstructural changes due to cyclic deformation, the effect of experimentals parameters, i.e. stress amplitude and mean stress, and the influence of the film thickness on the fatigue behavior of the films. It is clear from Fig. 3.7 and Fig. 3.9 that the thickness of the films investigated has an effect on the fatigue behavior. The thinner the film, the higher the stress amplitude necessary to induce fatigue damage. An

attempt will be made to describe the mechanisms leading to fatigue damage in thin films on the basis of current understanding of thin film deformation and bulk fatigue.

3.4.1 Fatigue damage

The appearance of the surface extrusions shown in Fig. 3.8 and Fig. 3.9 is reminiscent of fatigue damage typically found in bulk single- and polycrystalline *fcc* metals (e.g. [28], [29], [30]). Cyclic deformation in bulk materials has been well investigated and the main characteristics can be summarized in a few sentences: In ductile crystals cyclic straining induces well-defined dislocation structures, i.e. a vein structure and *PSB*s (as a result of primary slip) and a cell structure (when multiple slip is more pronounced). At intermediate plastic strain amplitudes, a large fraction of the plastic strain may become localized in the *PSB*s, which are considered to be the major cause for fatigue crack nucleation. The dislocation arrangements have been extensively studied by *TEM* (see for example [31]-[43]). At the surface, a pronounced relief evolves at intermediate and high plastic strains (e.g. [33], [39], [44]), but also the vein structure was observed to be related to extrusions [42]. Furthermore, the existence of point defects in fatigued metals was inferred from changes in and the recovery of the electrical resistivity [45]-[47]. It has been postulated that vacancies or their agglomerates produced by glide processes are responsible for a volume increase resulting in extrusion of material [48], [49]. Moreover, several authors claim to have observed point-defect clusters [50], [51] and micropores [52]-[55] in fatigued *fcc* metals. The annihilation of narrow edge dislocation dipoles as well as intersections of dislocations are sources of vacancy type defect production [53], [56]. A dipole consisting of edge dislocations in Cu will annihilate to form a vacancy or an interstitial if the spacing of the dislocations becomes smaller than about 1.6 nm [49]. The majority of the dipoles that are annihilated during fatigue of bulk Cu are of the vacancy type [57], leading to a substantial increase in the vacancy concentration [45], [46].

It is unlikely that veins, *PSB*s or dislocation cells in a bulk sense would form in the course of thin film fatigue when the film thickness is smaller than 1.5 µm: In this case, the film thickness as well as the grain size, which usually is comparable to the film thickness, are much smaller than what appears to be necessary for *PSB* formation [42] and the dimensions of cells usually are of the same order as our thin film dimensions [44], [58]-[60]. *TEM* investigations of films having different thicknesses confirm these statements: In Cu foils that were 100 µm thick, bulk-like dislocation structures were found [8], [61], whereas in Cu films of 1 µm thickness only single dislocations were observed [62].

The processes responsible for the production of point defects seem to be of a more general nature, being also active in thin films: A general observation on fatigued thin film specimens is the formation of voids at the film-substrate interface beneath the extrusions (compare Fig. 3.8(c)), which we believe to result from vacancy condensation. The irregular shape of the void in Fig. 3.8(c) indicates that it was produced rather by vacancy condensation than by shear processes. Prior to the fatigue tests no voids were observed. Voids beneath extrusions have also been observed in case of fine- as well as coarse-grained thin Cu films (see Ref. [63] and chapter 4). The damage process can be described as follows: Vacancies are created close to the film-substrate interface and coalesce to form voids accompanied by a roughening of the surface. The voids inside individual grains band together and grow towards the surface. Finally, cracks are initiated inside the extruded grains at the voids along slip traces, and, in addition, cracks are initiated at intersections of slip lines and grain boundaries. Voids and extrusions in thin films were found to be a prerequisite for the formation of fatigue cracks [26]. Crack extension along grain boundaries has also been observed in ductile bulk materials due to impinging *PSB*s at grain boundaries [64], [65] and to surface steps at the boundary [66].

A qualitative model of extrusion formation in thin metal films was proposed by Schwaiger and Kraft [24]. This model is based on the mechanism of dislocation motion in thin films on substrates as discussed by several authors [3], [67], [68] and schematically shown in Fig. 3.11: As a dislocation moves in a thin film by “channeling”, an additional dislocation segment is created at the film-substrate interface. It is assumed that under cyclic loading conditions dislocations of opposite Burgers vectors are created at the interface as dislocations move back and forth on different glide planes. As proposed by Schwaiger and Kraft [24] the voids at the film-substrate interface observed after fatigue are due to the annihilation of vacancy-type edge dislocation dipoles at or close to the interface, and dislocations form slip steps by emergence at the surface. The irregularity of the surface roughening can be explained by continuous annihilation of screw dislocations leading to glide processes in a rather random and irreversible manner, as stated for fatigue behavior of bulk materials [69]. A large enough number of cycles finally leads to a supersaturation of vacancies and voids are created at the interface.

In the model of Essmann *et al*. [49] vacancies play an important role in the process of extrusion formation. Due to the vacancies in a *PSB* the material volume increases and material protrudes out of the crystal. However, according to Essmann *et al.* [49] the height of an extrusion is limited by the grain size in case of a polycrystal or the sample diameter when a single crystal is fatigued. Different from these findings, the extrusions in thin metal films

eventually reach a height comparable to the film thickness. Apparently, during cyclic deformation of thin films, the role of vacancies is more important than in cyclic deformation of bulk materials. This might be due to the fact that the interface between film and substrate does not act as a sink or source for point defects, as also discussed for diffusional creep in thin films [70], [71].

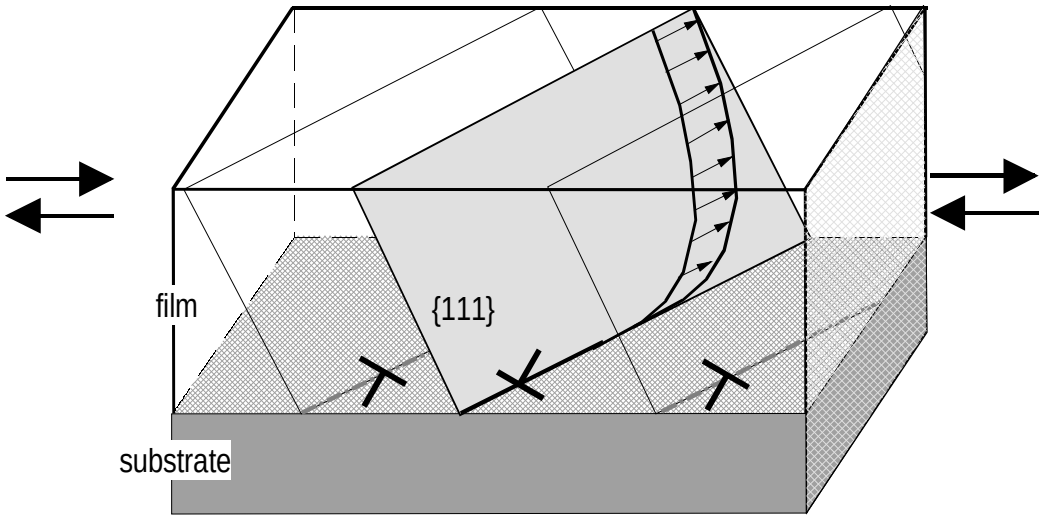

Fig. 3.11: Schematic of the motion of dislocations in a thin film under cyclic loading conditions.

From Fig. 3.10 we learn that (111) grains for the most part did not show extrusions after the fatigue experiments. However, from simple considerations of elastic behavior neglecting grain interaction effects, the stresses in (111) grains should be higher than in (100) grains: For uniaxial tension perpendicular to the film normal, the (111) grains are elastic isotropic with E=84 GPa, and the (100) grains are anisotropic with E between 44 and 84 GPa. Therefore, the stress in (100)-oriented grains is on average smaller than in (111)-oriented ones, at least in the elastic regime. This argument was indeed confirmed for Cu (which has a similar elastic anisotropy) by micro-tensile testing [72]. According to these findings, failure of (111)-oriented grains seems to be more probable, which is contradictory to our findings.

According to the *Schmid law*, slip occurs when the shear stress acting along a slip direction in the slip plane reaches a critical value; therefore, the slip systems with the highest *Schmid* factor will be activated as the shear stress is highest there. So one could argue that the *Schmid* factor of the active slip systems in (100) grains was larger than in (111) grains. In Fig. 3.12 the *Schmid* factors for a uniaxial stress perpendicular to the film normal are shown as a function of the rotation angle of the load axis for a (001)- and a (111)-oriented grain, respectively. In the

case of a (001)-oriented grain (see Fig. 3.12(a)), 12 slip systems can principally become active. The octahedral planes and their edges represent the planes and directions of slip, respectively. For a (111)-oriented grain (see Fig. 3.12(b)), there are nine slip systems to be activated, as the plane parallel to the surface will not be active. From these plots we learn that for the (100)- as well as for the (111)-oriented grains the maximum *Schmid* factors are 0.49 and 0.47, respectively. Further, there are slip systems with a *Schmid* factor between 0.4 and 0.5 for all rotation angles in both grain orientations. These considerations are consistent with the results obtained from *EBSD* measurements, as the *Schmid* factors of the damaged grains were not necessarily higher than the ones of the undamaged grains: The maximum *Schmid* factors of the primary slip systems of the extruded grains was between 0.41 and 0.49, those of the undamaged ones between 0.33 and 0.49.

From Fig. 3.12 we further conclude that in (111)-oriented grains the slip systems with the highest *Schmid* factors have the Burgers vectors in a plane parallel to the surface, independent of the rotation angle. This is not the case, however, for the primary slip systems in (100)-oriented grains. Let us consider a slip geometry as shown in Fig. 3.11 for a (001)-oriented grain: in this case the *Burgers* vector makes an angle of 60° to the line of the interface dislocation. Thus, the dislocation deposited at the interface is a 60° mixed dislocation. In case of a (111) orientation, a dislocation gliding along the primary slip planes creates a pure screw dislocation at the interface. However, according to the fatigue model described above, the formation of vacancies requires the annihilation of edge dislocations, as the annihilation of screw dislocations does not produce vacancies. Hence, the production of vacancies in (001)-oriented grains is more probable, while the damage formation in grains close to a (111) orientation should be inhibited, as there is no or only a very small edge component of the dislocations deposited at the interface. This explains, why (100) grains are more susceptible to fatigue damage than (111) grains.

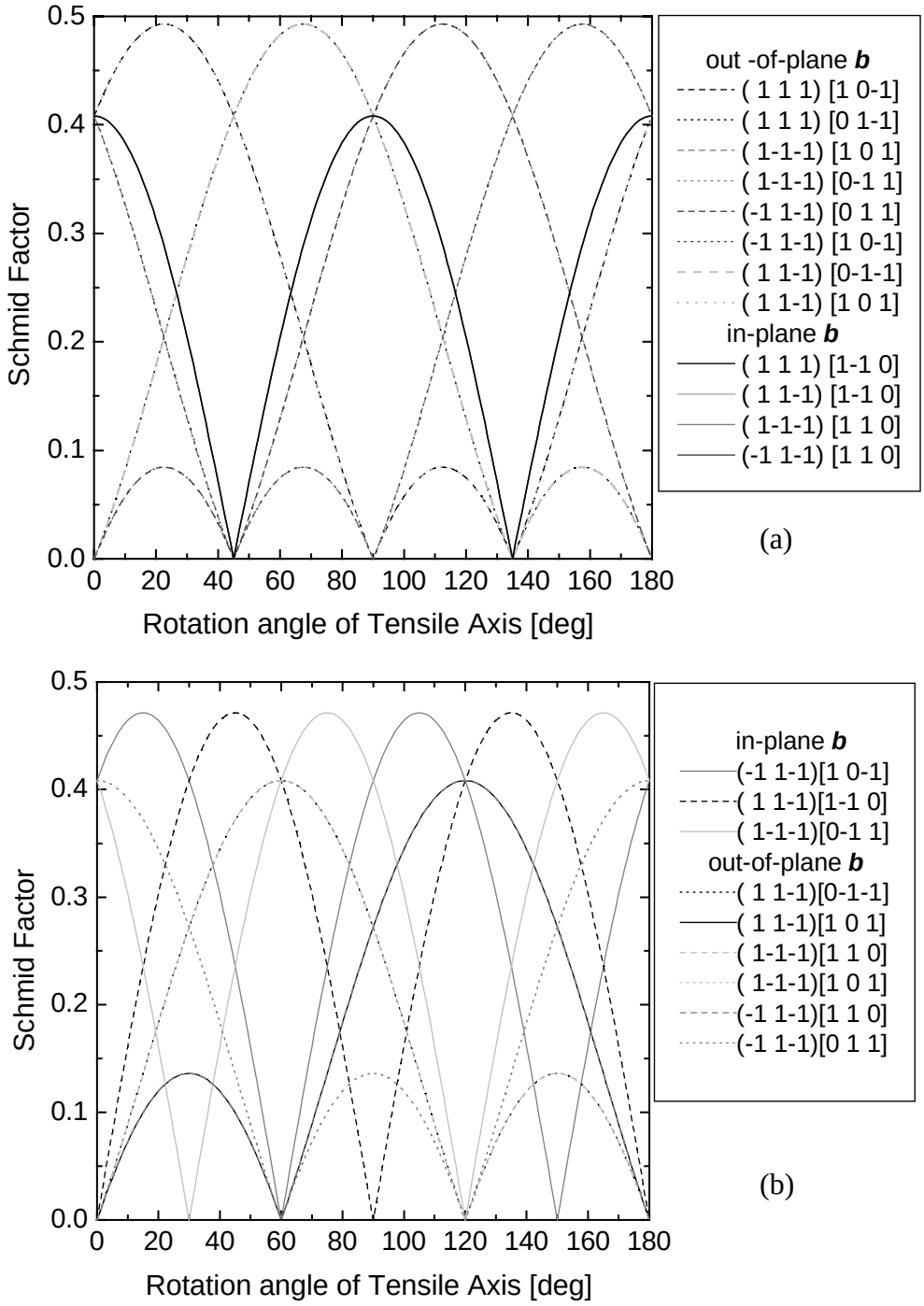

Fig. 3.12: *Schmid* factor of all slip systems vs. rotation angle of the tensile axis in a plane parallel to the surface for a (a) [001]- and a (b) [111]-oriented grain. A rotation angle of 0º refers to the (a) [001] and (b) [1-10] direction. For the (100)- as well as for the (111)-oriented grains the maximum *Schmid* factors are 0.49 and 0.47, respectively. There are slip systems with a *Schmid* factor between 0.4 and 0.5 for all rotation angles in both grain orientations. The differences in the *Schmid* factor between (100) and (111) grains are not sufficiently large to explain the observations that (100) grains are more susceptible to fatigue damage than (111) grains.

3.4.2 Influence of a mean stress on fatigue life

In our experiments, a mean stress was superimposed on the cyclic loading conditions. Fatigue life prediction is generally difficult and complex when mean stresses are present. Morrow [73] proposed that fatigue life under the action of mean stresses can be estimated by the expression

$$\sigma_a = (\sigma_f' - \sigma_m) \cdot (2N_d)^{c_s}, \qquad (3.2)$$

$$N_d = \left(1 - \frac{\sigma_m}{\sigma_f'}\right)^{\frac{1}{c_s}} \cdot N_d\big|_{\sigma_m=0} \qquad (3.3)$$

where σ_a is the stress amplitude, σ_m the mean stress, σ_f' the fatigue strength coefficient, c_s the fatigue exponent, and N_d the number of cycles to failure. The fatigue strength coefficient is comparable to the fracture strength of a material; a tensile mean stress can be considered to reduce and a compressive mean stress to increase the fatigue strength coefficient. Hence, for a certain stress amplitude and different mean stresses an array of *S-N* curves is obtained.

S-N curves (according to eq. (3.2)) for a stress amplitude of 79 MPa and mean stresses between 0 and 520 MPa are shown in Fig. 3.13. For c_s a value of –0.115 was assumed, which is typical for bulk metals [74]. The fatigue strength coefficient was varied to obtain reasonable agreement with the experimental data and found to be about twice the yield stress.

In our experiments on the 0.6 µm thick films the fatigue life decreased with increasing mean stresses (compare Fig. 3.6); the respective data are shown as full symbols in Fig. 3.13. The mean stresses in these experiments were between 160 and 288 MPa. It has to be pointed out that the datapoints lie well within the expected range in the diagram, but not exactly on the corresponding line. The films appear to follow the relation according to Morrow, but the plot in Fig. 3.13 is admittedly a gross approximation owing to our small number of experiments investigating mean stress effects. Experiments with a smaller amplitude but higher mean stresses have been added to the plot (gray symbols); within 3.8×10^6 cycles no stiffness decrease occurred. The mean stresses were 350 and 520 MPa respectively, the datapoints do not lie in the expected range of the plot; according to the calculated curves these films should have failed at cycle numbers an order of magnitude smaller. This may imply that there is a fatigue limit at about 60 MPa for the 0.6 µm thick Ag films on a substrate.

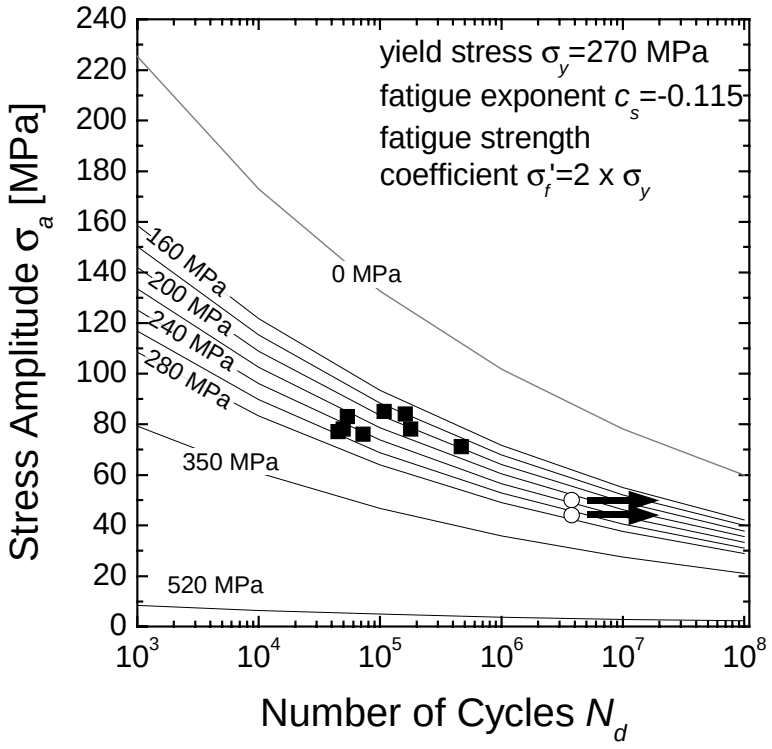

Fig. 3.13: Effect of a mean stress on the fatigue life according to eq. (3.2) [73]. Experimental data from Table 3.4(b) is also shown. For c_s and σ_f' –0.115 and 2 x σ_y were used.

Phenomenologically the influence of a mean stress can be described by bulk laws, but the mechanisms responsible must be different: In the bulk, the propagation of fatigue cracks is usually accelerated by a tensile stress perpendicular to the crack, in static as well as in cyclic deformation, or slowed down by a compressive mean stress. However, in our experiments the onset of fatigue damage, i.e. the formation of voids at or close to the film-substrate interface is detected by recording the stiffness of the cantilever beams. At a certain stress amplitude increasing mean stresses result in a higher maximum stress. Therefore, a higher initial dislocation density is created and the annihilation distance is more easily achieved rendering dislocation annihilation more probable, which in turn results in a higher density of vacancies. As a result, it is conceivable that in the presence of a tensile mean stress void nucleation and void growth are enhanced. Finally, we wish to emphasize that the influence of a mean stress on fatigue life is of particular importance for thin films, since metal thin films exhibit usually very high residual tensile stresses after processing. As a result, the fatigue lifetime of technological thin film devices is expected to be reduced and a clearer understanding of these effects remains desirable.

3.4.3 Influence of the film thickness

From Fig. 3.7, we find that the stress amplitude has to be increased with decreasing film thickness in order to induce fatigue damage. Fig. 3.7 can be interpreted as a snapshot of *S-N* curves for different film thicknesses at the arbitrarily chosen number of cycles of 3.8×10^6, which is an order of magnitude smaller than the numbers of cycles typically invoked to define the fatigue limit of materials.

The experimental observations suggest that a dimensional constraint might be active in the films investigated. In the model of damage formation presented above (compare 3.4.1), the motion of dislocations in a thin film was assumed to follow the dimensional constraint discussed by Nix [3]. In this section, this formulation will also be applied to rationalize the thickness dependence of the applied stress range. The Nix model [3] is an energy argument in which the stress σ_{Nix} required to move a dislocation through a film is determined by the work to deposit a dislocation segment at the interface between the substrate and the film. This model has often been applied to explain the thickness dependence of the yield stress, but will be used in a different sense here, as shown below.

Originally, the model applies to a biaxial stress state, but in the beam deflection experiments an approximate uniaxial tensile stress is applied. For this special case and in the absence of a passivating surface layer σ_{Nix} is given by

$$\sigma_{Nix} = \frac{\sin\Phi}{\cos\alpha\cos\lambda}\frac{b}{2\pi(1-\nu)h}\left[\frac{\mu_f\mu_s}{\mu_f+\mu_s}\ln\left(\frac{\beta h}{b}\right)\right] \qquad (3.4)$$

where Φ is the angle between the glide plane normal and the film normal, α is the angle between the glide plane normal and the tensile axis, λ is the angle between the film normal and the Burgers vector, b is the magnitude of the Burgers vector, ν is Poisson's ratio, h is the film thickness, μ_f and μ_s are the shear moduli of film and substrate, respectively, and β is a numerical constant defining the cut-off radius of the stress field of a dislocation at the substrate. It is clear from eq.(3.4) that the minimum stress σ_{Nix} required to drive a dislocation through a film varies linearly with the reciprocal film thickness.

In Fig. 3.14(a) the data from Fig. 3.7 are replotted as gray symbols. The minimum stress amplitude of damaged beams (black open squares) is named the critical stress amplitude, since this stress is required at least in order to induce fatigue damage. For films thinner than 0.6 µm the critical stress amplitude increases significantly with decreasing film thickness, whereas the curve in Fig. 3.14(a) slopes down gradually for thicker films. For thicker films we expect that dimensional influences decrease and the critical stress amplitude approaches a constant value

also describing fatigue behavior of bulk material. However, a slow decrease is observed in Fig.3.14, but the asymptotic limit was not reached in the experiments performed.

In Fig.3.14(b) the critical stress amplitude for all film thicknesses is shown. The dashed and dotted lines represent the stress σ_{Nix} according to eq. (3.4) for (111)- and (100)-oriented grains, respectively.

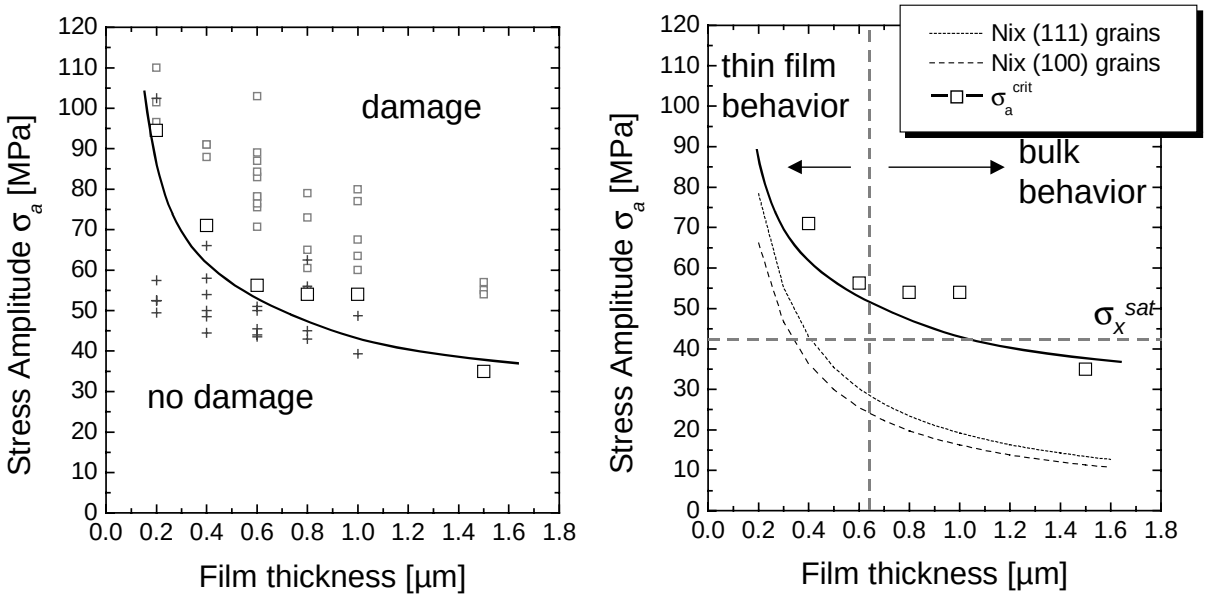

Fig. 3.14: (a) Stress amplitude vs. film thickness according to Fig. 3.7. The critical stress amplitude is symbolized by dark squares. Note that for the 1.5 µm thick film damage was always observed after 3.6 x 10^6 cycles. (b) The dashed and dotted lines represent predictions for the critical stress amplitude according to eq.(3.4), for (111)- and (100)-oriented grains, respectively, using the following values: $\frac{\sin\Phi}{\cos\alpha\cos\lambda} = 2.145$ and 1.8125 for a (111)- and a (001)-oriented grain, β=1.7, μ_f=26.1 GPa,μ_s=30.2 GPa, and ν=0.38. For $\cos\alpha\cos\lambda$ the average of the maximum and minimum value for all possible angles was used.

We interpret the stress σ_{Nix} as the minimum stress amplitude that is required at least to move the first dislocation in a thin film. When the applied stress amplitude is smaller than the stress according to eq. (3.4) no dislocations move, and no fatigue damage can occur. Hence, the stress σ_{Nix} can be regarded as a fatigue limit for thin films on a substrate.

The experimental data and the predictions of the Nix model show a similar functionality. However, the critical stress amplitude is greater than the stress σ_{Nix} for all film thicknesses. This discrepancy can be explained as follows: The films were tested over 3.8 x 10^6 cycles, which is an order of magnitude smaller than the numbers of cycles typically invoked to define the fatigue limit of materials. Therefore, higher stress amplitudes are expected at these smaller

cycle numbers, as determined in our experiments. Furthermore, grain boundaries have not been incorporated in the Nix formulation, which would shift the stress σ_{Nix} to higher stress levels and further reduce the gap in between the curves. However, fatigue tests on thin films with different grain sizes or on single-crystalline films at higher cycle numbers have not yet been performed, but would be desirable. These tests would further clarify to what extent the Nix formulation, which usually describes the dimensional constraint exerted on a dislocation moving in a thin film, also describes the fatigue behavior of thin films on a substrate.

As the film thickness influences dislocation motion, we expect a transition from bulk- to thin film fatigue behavior at a certain film thickness. In bulk material, persistent slip bands (*PSB*s) are typically observed during fatigue. A *PSB* is divided into channels by a periodic array of dislocation walls made up of edge dislocation dipoles, as schematically shown in Fig. 3.15(a). Self-organization of the dislocation structures results in typical distances between the *PSB* walls, which is about 1.3 µm for Cu [38]. Deformation in a *PSB* is accomplished by edge dislocations bowing out from the walls and traversing the channel, thereby producing screw dislocations, which then glide along the channels [38], [40]. The mains question is, whether *PSB*-like dislocation structures can form and for which film thicknesses similar deformation processes occur.

We would like to point out that the motion of dislocations in a thin film resembles the motion of dislocations in a *PSB* channel, but is expected to be influenced by the film thickness. In the Nix model the dislocation motion in a thin film is described as a channeling process (compare also Fig. 3.11). This is schematically shown in Fig. 3.15(b). The channel is defined by the film-substrate interface and the film surface, respectively. Due to the free surface, however, the threading dislocation can move along the surface, and, therefore, the thin film corresponds to only half the *PSB* channel in bulk, as shown in Fig. 3.15(a) and (b). From the geometrical analogy in Fig. 3.15 and assuming similar wall spacings in Ag as in Cu, we conclude that at a film thickness of 0.65 µm (which corresponds to about half the *PSB* wall spacing) the transition between bulk and thin film fatigue behavior occurs. This is in reasonable agreement with our observations that the critical stress amplitude increases significantly for films thinner than 0.6 µm (compare Fig. 3.14).

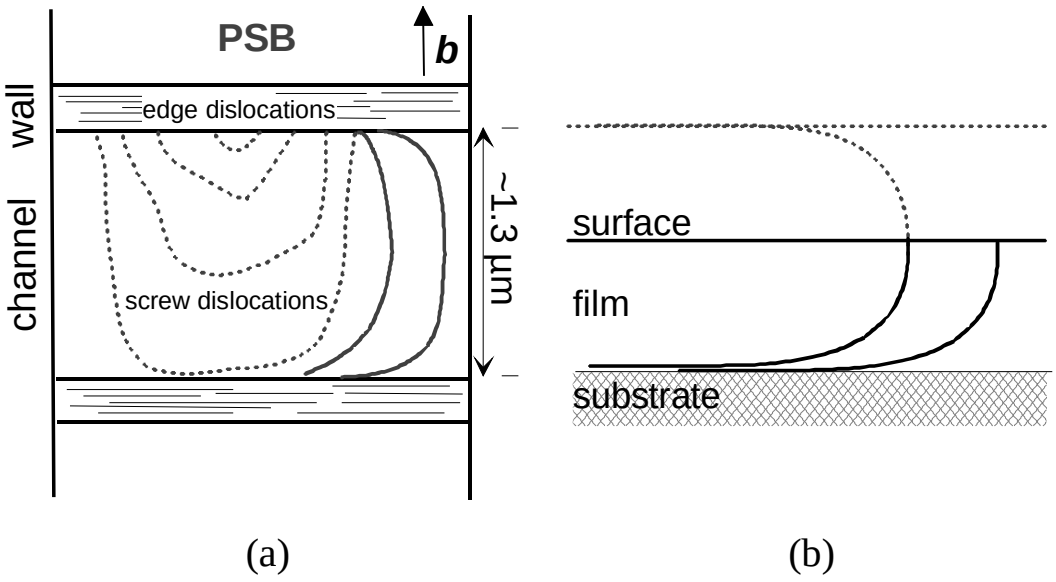

Fig. 3.15: Schematic comparing the dislocation motion (a) in a *PSB* channel and (b) in a thin film. The wall spacing in a *PSB* of Cu was found to be about 1.3 µm [38]. The dislocation moves in a thin film in a channel defined by the film-substrate interface and the surface.

In bulk single crystals *PSB* formation is related to a certain resolved shear stress and a plateau in the cyclic stress-strain curve (compare 2.2.2). For Ag single crystals, the plateau shear stress was measured to be 17.5 MPa [40]. Hence, for bulk polycrystals this corresponds to a stress σ_x^{sat} of ~43 MPa, using a *Schmid* factor of about 0.41, which was found to be a typical value for our films (see 3.4.1). The observed stress amplitudes of films thicker than ~1 µm are comparable to σ_x^{sat} (see Fig. 3.14). This indicates that *PSB*-like deformation mechanisms start to operate in the thicker films, since the geometrical restrictions of Fig. 3.15 do not apply. For thicker films we expect the stress amplitude to approach the bulk value of ~43 MPa. However, within the scope of the experiments performed in this work the asymptoptic limit has not been reached; further investigations of thicker films should be performed. Nevertheless, we have shown in this work that the film thickness affects the cyclic deformation behavior of thin films. A model originally proposed to describe monotonic behavior of thin films was shown to provide a suitable description of thin film fatigue.

3.5 Summary and conclusions

Fatigue tests on thin Ag films with thicknesses between 0.2 and 1.5 µm on SiO_2 substrates were performed. The films were investigated by cantilever microbeam deflection and analyzed by finite element calculations. The findings can be summarized as follows:

(1) The surface damage is similar in appearance to extrusions typically observed after fatigue of bulk materials. Voids were observed beneath the extrusions close to the film-substrate interface. Extrusions were preferentially observed in (100)-oriented grains, whereas (111)-oriented grains were to a large extent undamaged after fatigue.

(2) The film thickness was found to affect the cyclic deformation behavior of the films investigated. The results suggest that there is a fatigue limit for thin Ag films on a substrate. The stress amplitude required to induce fatigue damage was found to increase significantly for films thinner than 0.6 µm.

(3) Tensile mean stresses were found to reduce the fatigue life of the thin films tested. The data could be described by empirical bulk laws, irrespective of the different mechanisms responsible for fatigue failure in bulk and thin film materials.

(4) The evolution of extrusions in the thin films due to cyclic loading was described by a model based on a dimensional constraint on dislocation motion and the formation of vacancies due to dislocation annihilation. Based on this model the orientation dependence could be explained: the formation of voids is restricted in (111)-oriented grains.

(5) The increase of the critical stress amplitude with decreasing film thickness for films thinner than 0.6 µm was rationalized by a transition from bulk to thin film behavior at the respective film thickness.

This work confirms previous observations by several authors that the mechanical properties of thin films generally differ from those of bulk materials of the same composition. Further work is required to understand in more detail how the fatigue mechanisms depend on grain size and texture, and how they operate in small dimensions.

3.6 Acknowledgements

This work was partially supported by the Deutsche Forschungsgemeinschaft under contract Ar 201/5-2. We also acknowledge the support of Dr. D. Müller and R. Völker, who prepared the thin Ag films. The SiO_2 beams were prepared at the Center of Integrated Systems at Stanford University.

3.7 References

1. Venkatraman, R. and Bravman, J. C., "Separation of film thickness and grain boundary strengthening effects in Al thin films on Si", *J. Mater. Res.* **7** (8), 2040-2048 (1992).
2. Freund, L. B., "The stability of a dislocation threading a strained layer on a substrate", *J. Appl. Mech.-Transactions of the ASME* **54** (3), 553-57 (1987).
3. Nix, W. D., "Mechanical Properties of Thin Films", *Metall. Trans. A* **20**, 2217-2245 (1989).
4. Thompson, A. W. and Backofen, W. A., "The effect of grain size on fatigue", *Acta Metall.* **19**, 597-606 (1971).
5. Keller, R.-M., Baker, S. P. and Arzt, E., "Quantitative Analysis of Strengthening Mechanisms in Thin Cu Films: Effects of Film Thickness, Grain Size, and Passivation", *J. Mater. Res.* **13** (5), 1307-1317 (1998).
6. Hommel, M. and Kraft, O., to be published in *Acta Mater.*
7. Baker, S. P., Kretschmann, A. and Arzt, E., "Thermomechanical behavior of different texture components in Cu thin films", *Acta Mater.* **49**, 2145-2160 (2001).
8. Judelewicz, M., Künzi, H. U., Merk, N. and Ilschner, B., "Microstructural development during fatigue of copper foils 20-100 µm thick", *Mater. Sci. Eng. A* **186**, 135-142 (1994).
9. Hong, S. and Weil, R., "Low cycle fatigue of thin copper foils", *Thin Solid Films* **283**, 175-181 (1996).
10. Merchant, H. D., Minor, M. G. and Liu, Y. L., "Mechanical Fatigue of Thin Copper Foil", *J. Electronic Mater.* **28** (9), 998-1007 (1999).
11. Oshida, Y. and Chen, P. C., "High and Low-Cycle Fatigue Damage Evaluation of Multilayer Thin Film Structure", *J. Electronic Packaging* **113**, 58-62 (1991).
12. Hong, S., Weihs, T. P., Bravman, J. C. and Nix, W. D., "The Determination of Mechanical Parameters and Residual Streses for Thin Films Using Micro-Cantilever Beams", in *Thin Films: Stresses and Mechanical Properties*, edited by Bravman, J. C., Nix, W. D., Barnett, D. M. and Smith, D. A. (Mater. Res. Soc. Proc. Vol. 130, (1989)), pp. 93-98.
13. Kuschke, W.-M., Kretschmann, A. and Keller, R.-M., "Textures of thin copper films", *J. Mater. Res.* **13** (10), 2962-1968 (1998).
14. Kretschmann, A., "Untersuchung der mechanischen Eigenschaften von Kupfer-Duennschichten mit roentgenographischen Spannungsmessmethoden", *PhD Dissertation* (Institut f. Metallkunde, Universität Stuttgart (1997)).

15. Levi-Setti, R., Fox, T. R. and Lam, K., "Ion channeling effects in scanning ion microscopy with a 60 keV Ga^{+}probe", *Nucl. Instr. Methods Phys. Res.* **205** (1-2), 209-309 (1983).
16. Weihs, T. P., Hong, S., Bravman, J. C. and Nix, W. D., "Mechanical Deflection of Cantilever Microbeams: A New Technique for Testing the Mechanical Properties of Thin Films", *J. Mater. Res.* **3** (5), 931-942 (1988).
17. Baker, S. P. and Nix, W. D., "Mechanical Properties of Compositionally Modulated Au-Ni Thin Films: Nanoindentation and Microcantilever deflection experiments", *J. Mater. Res.* **9** (12), 3131-3144 (1994).
18. Oliver, W. C. and Pharr, G. M., "An Improved Technique for Determining Hardness and Elastic Modulus Using Load and Displacement Sensing Indentation Experiments", *J. Mater. Res.* **7** (6), 1564-1583 (1992).
19. Pethica, J. B. and Oliver, W. C., "Mechanical Properties of Nanometre Volumes of Material: Use of the Elastic Response of Small Area Indentations", in *Thin Films: Stresses and Mechanical Properties*, edited by Bravman, J. C., Nix, W. D., Barnett, D. M. and Smith, D. A. (Mater. Res. Soc. Symp. Proc. Vol. 130, Mater. Res. Soc., Pittsburgh, PA (1989)), pp. 13-23.
20. Lawn, B., "Fracture of Brittle Solids", Cambridge University Press, (1993), p. 55.
21. CRC Handbook of Chemistry and Physics, edited by Weast, R. C. (1984).
22. Elsevier Materials Selector, Vol. 2, edited by Waterman, N. A. and Ashby, M. F. (1991).
23. Courtney, T. H., "Mechanics of Materials", McGraw-Hill Publishing Company, (1990), p. 48.
24. Schwaiger, R. and Kraft, O., "High Cycle Fatigue of Thin Silver Films Investigated by Dynamic Microbeam Deflection", *Scripta Mater.* **41** (8), 823-829 (1999).
25. Gere, J. M. and Timoshenko, S. P., "Mechanics of Materials", PWS-KENT Publishing Company, Boston (1984).
26. Schwaiger, R. and Kraft, O., "Fatigue behavior of thin silver films investigated by dynamic microbeam deflection", in *Thin Films: Stresses and Mechanical Properties VIII*, edited by Vinci, R. P., Besser, P. R., Kraft, O., Moody, N. and Shaffer, E. (Materials Research Society Symp. Proc. Vol. 594, Materials Research Society, Pittsburgh, PA (2000)), pp. 201-206.
27. Barr, D. L. and Brown, W. L., "Contrast formation in focused ion beam images of polycrystalline aluminum", *J. Vac. Sci. Technol. B* **13** (6), 2580-2583 (1995).

28. Mughrabi, H. and Wang, R., "Cyclic strain localization and fatigue crack initiation in persistent slip bands in face-centered cubic metals and single phase alloys", in *Defects and Fracture*, edited by Sih, G. C. and Zorski, H. (Proc. First Int. Symp. on Defects and Fracture, Martinus Nijhoff Publishers, The Hague (1982)), pp. 15-28.
29. Rasmussen, K. V. and Pedersen, O. B., "Fatigue of copper polycrystals at low plastic strain amplitudes", *Acta Metall.* **28**, 1467-1478 (1980).
30. Wang, R., Mughrabi, H., McGovern, S. and Rapp, M., "Fatigue of Copper Single Crystals in Vacuum and in Air I: Persistent Slip Bands and Disloaction Microstructures", *Mater. Sci. Eng.* **65**, 219-233 (1984).
31. Basinski, S. J., Basinski, Z. S. and Howie, A., "Early stages of fatigue in copper single crystals", *Phil. Mag.* **19**, 899-924 (1969).
32. Hancock, J. R. and Grosskreutz, J. C., "Mechanisms of fatigue hardening in copper single crystals", *Acta Metall.* **17**, 77-97 (1969).
33. Winter, A. T., "A model for the fatigue of copper at low plastic strain amplitudes", *Phil. Mag.* **30**, 719-738 (1974).
34. Laird, C., "The fatigue limits of metals", *Mater. Sci. Eng.* **22**, 231-236 (1976).
35. Lukás, P. and Klesnil, M., "Dislocation structures in fatigued single crystals of Cu-Zn system", *Phys. Stat. Sol. (a)* **5**, 247-258 (1971).
36. Backofen, W. A., "Formation of slip-band cracks in fatigue", in *Fracture*, edited by Averbach, B. L., Felbeck, D. K., Hahn, G. T. and Thomas, D. A. (Inter. Conf. on the Atomic Mechanisms of Fracture, The Technology Press of MIT, Cambridge (1959)), pp. 435-449.
37. Finney, J. M. and Laird, C., "Strain localization in cyclic deformation of copper single crystals", *Phil. Mag.* **31**, 339-366 (1975).
38. Grosskreutz, J. C. and Mughrabi, H., "Description of the work-hardened structure at low temperature in cyclic deformation", in *Constitutive equations in plasticity* (The MIT Press, Cambridge, MA, (1975)), pp. 251-325.
39. Mughrabi, H., "The cyclic hardening and saturation behavior of copper single crystals", *Mater. Sci. Eng.* **33**, 207-223 (1978).
40. Mughrabi, H., Ackermann, F. and Herz, K., "Persistent slipbands in fatigued face-centered and body-centered cubic metals", in *Fatigue Mechanisms* (Special Technical Publication 675, ASTM, Philadelphia, PA, (1979)), pp. 69-97.

41. Ackermann, F., Kubin, L. P., Lepinoux, J. and Mughrabi, H., "The dependence of dislocation microstructure on plastic strain amplitude in cyclically strained copper single crystals", *Acta Metall.* **32** (5), 715-725 (1984).
42. Holzwarth, U. and U., E., "Transformation of dislocation patterns in fatigued copper single crystals", *Mater. Sci. Eng. A* **164**, 206-210 (1993).
43. Wang, Z., Gong, B. and Wang, Z. G., "Cyclic deformation behavior and dislocation structures of [001] copper single crystals - II. Characteristics of dislocation structures", *Acta Mater.* **45** (4), 1379-1391 (1997).
44. Feltner, C. E. and Laird, C., "Cyclic stress-strain response of fcc metals and alloys - II Dislocation structures and mechanisms", *Acta Metall.* **15**, 1633-1653 (1967).
45. Johnson, E. W. and Johnson, H. H., "Imperfection density of fatigued and annealed copper via electrical-resistivity measurements", *Trans. Metall. Soc.* **233**, 1333-1339 (1965).
46. Polák, J., "The effect of intermediate annealing on the electrical resistivity and shear stress of fatigued copper", *Scripta Metall.* **4**, 761-764 (1970).
47. Polák, J., "Resistivity of fatigued copper single crystals.", *Mater. Sci. Eng.* **89**, 35-43 (1987).
48. Mughrabi, H., "Microscopic Mechanisms of Metal Fatigue", in *Strength of Metals and Alloys*, Vol. 3, edited by Haasen, P., Gerold, V. and Kostorz, G. (Proc. of the 5th Int. Conf., Pergamon Press, Oxford (1980)), pp. 1615-1638.
49. Essmann, U., Gösele, U. and Mughrabi, H., "A model of extrusions and intrusions in fatigued metals", *Phil. Mag. A* **44** (2), 405-426 (1981).
50. Piqueras, J., Grosskreutz, J. C. and Frank, W., "The influence of point-defect clusters on fatigue hardening of copper single crystals", *Phys. Stat. Sol. A* **11**, 567-580 (1972).
51. Antonopoulos, J. G. and Winter, A. T., "Weak-beam study of dislocation structures in fatigued copper", *Phil. Mag.* **33**, 87-95 (1976).
52. Thompson, N., Wadsworth, N. and Louat, N., "The origin of fatigue fracture in copper", *Phil. Mag.* **1**, 113-126 (1956).
53. Argon, A. S. and Godrick, J. A., "Fatigue in lithium fluoride crystals at elevated temperature", in *FRACTURE 1969*, edited by Pratt, P. L. (Second International Conference on Fracture, Chapman and Hall Ltd, London, UK (1969)), pp. 576-586.
54. Ogura, T. and Karashima, S., "Studies on the structure developed around fatigue cracks of aluminium using a high voltage electron microscope", *Trans. Japan Inst. Metals* **15**, 324 (1974).

55. Yamamoto, A., Saka, H. and Imura, T., "In-situ study on the Fatigue Process of Metals by HVEM", *Kristall und Technik* **14** (10), 1275-1281 (1979).
56. Essmann, U. and Mughrabi, H., "Annihilation of dislocations during tensile and cyclic deformation and limits of dislocation densities", *Phil. Mag. A* **40** (6), 731-756 (1979).
57. Antonopoulos, J. G., Brown, L. M. and Winter, A. T., "Vacancy dipoles in fatigued copper", *Phil. Mag.* **34** (4), 549-563 (1976).
58. Pratt, J. E., "Dislocation substructure in strain-cycled copper as influenced by temperature", *Acta Metall.* **15**, 319-327 (1967).
59. Kayali, E. S. and Plumtree, A., "Stress-substructure relationships in cyclically and monotonically deformed wavy slip mode metals", *Metall. Trans. A* **13**, 1033-1041 (1982).
60. Plumtree, A. and Pawlus, L. D., "Substructural developments during strain cycling of wavy slip mode metals", in *Basic Questions in Fatigue*, Vol. 1 (Special Technical Publication 924, ASTM, Philadelphia, (1988)), pp. 81-97.
61. Judelewicz, M., "Cyclic deformation of 100 μm thin polycrystalline copper foils", *Scripta Metall. Mater.* **29**, 1463-1466 (1993).
62. Read, D. T., "Tension-tension fatigue of copper thin films", *Int. J. Fatigue* **20** (3), 203-209 (1998).
63. Kraft, O., Schwaiger, R. and Wellner, P., "Fatigue in Thin Films: Lifetime and Damage Formation", to be published in *Mater. Sci. Eng. A.*
64. Figueroa, J. C. and Laird, C., "Crack initiation mechanisms in copper polycrystals cycled under constant strain amplitudes and in step tests", *Mater. Sci. Eng.* **60**, 45-58 (1983).
65. Mughrabi, H., Wang, R., Differt, K. and Essmann, U., "Fatigue crack initiation by cyclic slip irreversibilities in high cycle fatigue", in *Quantitative Measurement of Physical Damage* (Special Technical Publication 811, ASTM, Philadelphia, PA, (1983)), pp.5- 45.
66. Kim, W. H. and Laird, C., "Crack Nucleation and stage I propagation in high strain fatigue - II. Mechanism", *Acta Metall.* **26**, 789-799 (1978).
67. Chaudari, P., "Plastic properties of polycrystalline thin films on a substrate", *Phil. Mag. A* **39** (4), 507-516 (1979).
68. Thompson, C. V., "The Yield Stress of Polycrystalline Thin Films", *J. Mater. Res.* **8** (2), 237-238 (1992).
69. Differt, K., Essmann, U. and Mughrabi, H., "A model of extrusions and intrusions in fatigued metals, II. Surface roughening by random irreversible slip", *Phil. Mag. A* **54** (2), 237-258 (1986).

70. Gao, H., Zhang, L., Nix, W. D., Thompson, C. V. and Arzt, E., "Crack-like grain-boundary diffusion wedges in thin metal films", *Acta Mater.* **47** (10), 2865-78 (1999).
71. Weiss, D., "Deformation Mechanisms in Pure and Alloyed Copper Films", *PhD Dissertation* (Institut für Metallkunde, Universität Stuttgart (2000)).
72. Hommel, M., "Röntgenographische Untersuchung des monotonen und zyklischen Verformungsverhaltens dünner Metallschichten auf Substraten", *PhD Dissertation* (Institut f. Metallkunde, Universität Stuttgart (2000)).
73. Morrow, J. D., in *Fatigue Design Handbook - Advances in Engineering*, Vol. 4, Sec. 3.2 (Society of Automotive Engineers, Warrendale, PA, (1968)), pp. 21-29.
74. Dieter, G. E., "Mechanical Metallurgy", McGraw-Hill, (1988), p. 392.

Chapter 4 Cyclic Deformation of Polycrystalline Cu Films

4.1 Introduction

The fatigue behavior of cyclically deformed Cu single crystals oriented for single slip as well as the resulting dislocation structures have been well investigated over a wide range of cyclic strain amplitudes [1]-[10]. In the low amplitude fatigue of Cu and other face-centered cubic (*fcc*) single crystals persistent slip bands (*PSB*s) play a central role; *PSB*s also form in Cu polycrystals [11]-[15], but less frequently than in single crystals [12]. They have a characteristic dislocation substructure usually embedded in a matrix structure consisting of a regular array of predominantly primary dislocation walls. The *PSB*s that are characteristic for moderate strain amplitudes have a rather constant wall spacing of 1.3 µm in Cu [16] and accommodate localized strains essentially by primary slip only, whereas the labyrinth or cell structures characteristic for high amplitude fatigue exhibit systematically smaller wall spacings and accommodate deformation by slip on more than one slip system [4], [17], [18].

It is questionable if dislocation structures typical for bulk fatigue are formed in thin films as their typical dimensions would exceed the thickness and the grain size of a thin film, which is typically comparable to the film thickness. Only few observations regarding the dislocation structure of metal films or foils after fatigue have been published [19]-[23]. The foils investigated by Judelewicz *et al.* [19], [20] were 100 µm thick and exhibited bulk like dislocation structures. Hong and Weil [22] reported transmission electron microscopy (*TEM*) studies of 25 µm thick Cu foils. They found cell structures only in grains larger than 2 µm. In thinner films, i.e. 1.1 µm thick Cu films, only individual dislocations were found [23].

The fatigue life of Cu foils was found to be affected by the thickness at a constant average grain size. In tests with constant stress amplitude it was increased by a factor of 10-30 at a thickness reduction by a factor of 5 [20]. An even more significant increase in lifetime with thickness reduction was found for thin Cu wires [24].

In this work the cyclic deformation behavior of Cu films with thicknesses between 0.4 and 3 µm on polyimide substrates was investigated. Due to the elastic nature of the substrate, the films were deformed in tension and compression as described in [25]. The films were cyclically loaded with a total strain range of 1 %. The amount of plastic strain was determined by micro-tensile tests in an X-ray diffractometer. The fatigued 3.0 µm thick film was investigated by *TEM*.

4.2 Experimental details

4.2.1 Sample preparation and characterization

Copper films were deposited by magnetron sputtering under *UHV* conditions (base pressure $6x10^{-7}$ Pa, sputter machine: DAF) onto 125 µm thick polyimide substrates. Before deposition the substrate surface was cleaned by Ar ion bombardment (1 min at 100 V). The deposition was performed at a power of 100 W and Ar pressure of $4.2x10^{-1}$ Pa. During deposition the substrate was electrically grounded and clamped to a plate that was cooled with liquid nitrogen. The Ar sputtering gas was purified with a gettering system. The deposition rate was 50 nm/min. The film thickness was adjusted by the duration of sputtering. The films were then annealed for 2 h at a temperature of 373 K without breaking the vacuum. The gage length of the dog-bone shaped tensile samples was 20 mm and the width 6 mm. Films with thicknesses of 0.4, 0.8, 1.0, and 3.0 µm were prepared.

The microstructure of the films was characterized by focused ion beam (*FIB*) microscopy. Digitized *FIB* images were evaluated using a Quantimet 500 (Zeiss, Oberkochen, Germany). The contrast mechanism in the *FIB* image is a result of ion channeling along varying crystallographic directions in the different grains that are exposed to the ion beam. Therefore, grain size measurements without special sample preparation may be routinely performed by tilting the sample to several angles of incidence and overlaying the respective images to determine the grain boundary locations. At just a single tilt angle adjacent grains may still have the same contrast, especially in a highly textured film. A series of four images of a surface area for each film thickness were taken with tilt angles of 0°, 15°, 20°, and 25°. The distortion due to the sample tilt was corrected by the *FIB* software. The identified grain boundaries were copied onto a transparency, which was digitized and analyzed utilizing the Quantimet. Twin boundaries were not taken into account. The grain size was defined as the diameter d of an equivalent circular grain area A:

$$d = 2 \cdot \sqrt{\frac{A}{\pi}} \qquad (3.1).$$

The microstructure through the depth of the film was investigated by preparing cross-sections through the film using the ion-milling mode of the *FIB* and subsequent imaging. The thickness of the films was examined in the same way.

The texture was investigated by X-ray diffraction in a 4-circle goniometer with a Cu anode; θ-2θ scans using Cu K_α radiation were performed in a range between 40° and 140° to identify existing grain orientations.

4.2.2 Testing procedure

Cu films on polyimide substrates were fatigued in experiments with a total strain range $\Delta\varepsilon_{tot}$ of 1 %. As described in [25], it is not possible to easily determine the stress-strain behavior of the films by measuring the externally applied force. Therefore, the stress-strain behavior of the Cu films was investigated beforehand by monotonic tests carried out with a micro-tensile machine that was mounted in an X-ray diffractometer. A Siemens D5000 $\theta-\theta$ goniometer with Cu-$K_{\alpha 1}$ radiation with a wavelength of 1.5404 Å, and parallel beam optics with a Goebel mirror and a position-sensitive detector were used for the X-ray measurements. The external load on the substrate was measured continuously by a load cell, and the total strain contactless by a laser extensometer (Fiedler Optoelektronik GmbH, Luetzen, Germany) directly on the sample. The sample was strained in steps of about 0.015 %, between which X-ray measurements were performed. The elastic strains were measured by the $\sin^2\psi$-method using {331} planes in <111>-oriented grains. Then, the stress components were calculated using *Hooke's law* and the elastic constants of Cu. Details of this procedure have been explained in Ref. [26]. The amount of plastic strain was determined from the total strain of the film-substrate composite and the elastic strain in the Cu film in the tensile direction measured by X-rays [27]. One complete loading cycle took about 12 h in time.

Subsequently, fatigue tests were performed on the same samples using a commercial electromechanical tensile testing machine (Zwicki 1120, Zwick, Germany). Since the polyimide substrate behaves elastically, a constant total strain range can be achieved by applying a constant force amplitude. The force was varied with a frequency of 0.1 Hz between a maximum and a minimum value to produce a total strain range $\Delta\varepsilon_{tot}$ of 1 %. The maximum force F_{max} was in the range between 27 and 33 N, depending on the film thickness, and the minimum force F_{min} was set to 2 N. The samples were carefully mounted in a special sample holder to avoid torsional deformation during the cyclic tests. The total strain was measured contactless directly on the sample by a laser extensometer (Fiedler Optoelektronik GmbH, Luetzen, Germany). For each cycle the strain range and the energy loss were recorded (see Fig. 4.1), which were found to be good indicators for the degradation of the film [28].

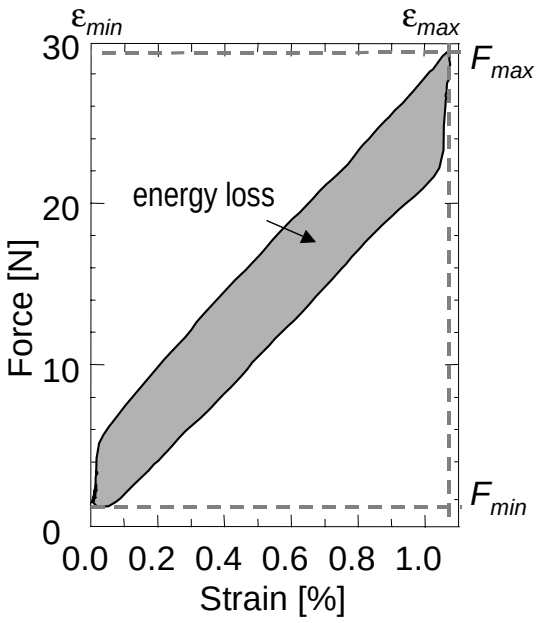

Fig. 4.1: Force-controlled fatigue cycle. The specimens were cycled between a maximum and minimum force F_{max} and F_{min}, respectively. F_{min} was set to 2 N to avoid buckling of the specimen, and F_{max} was adjusted with respect to the film thickness to apply a total strain amplitude ε_a of 0.5 % (equivalent to $\Delta\varepsilon_{tot} = \varepsilon_{max} - \varepsilon_{min} = 1\%$). During the fatigue cycles, strain, force, and energy loss were recorded.

4.2.3 Transmission electron microscopy

The fatigued 3.0 µm thick film was investigated by transmission electron microscopy (*TEM*) using a JEOL 200CX operated at an acceleration voltage of 200 kV. Cross-sectional *TEM* samples were prepared from two differently oriented grains by *FIB*, using an FEI 200 microscope with a maxium acceleration voltage of 30 kV. This method allows site-specific preparation of *TEM* samples. For this, the sample surface was inspected and sites of interest defined. Then, a thin tungsten film with a thickness of about 200 nm was locally deposited in order to avoid damage by the Ga+ ion beam. Two parallel stair-step trenches of ~30 µm length and ~5 µm depth were cut into the sample and the material remaining in-between was thinned to a thickness of less than 300 nm using decreasing beam currents and acceleration voltages; in this way damage from lateral deflection of Ga+ ions into the electron transparent region of the lamella was avoided. After the final thinning, the lamella was scanned from both sides at an acceleration voltage of 6 kV at a tilt angle of 45° to remove a thin layer that was probably damaged from milling. Finally, the lamella was cut loose, lifted out of the sample, and transferred to a *TEM* grid using a micromanipulator equipped with a glass capillary. This technique is described in a review by Giannuzzi and Stevie [29]. The Burgers vectors of

dislocations were determined by finding at least two different two-beam conditions fulfilling the invisibility criterion [30].

4.3 Results

4.3.1 Microstructural characterization

The film thickness was found to vary over the gage length due to the sputter geometry. A variation up to 10 % of the nominal value was typical. The cumulative frequency of the grain size was analyzed for each film thickness. The grain size distribution was found to be lognormal in the case of the 0.4 and the 0.8 μm thick films, but apparently not unimodal for the thicker films. Therefore, the grain size was characterized by the arithmetic mean values, which were determined to be between 0.87 and 1.45 μm (Table 4.1). The films had a columnar grain structure (all grain boundaries extending through the thickness of the film). The X-ray measurements indicated that the films were (111) and (100) textured as only peaks corresponding to these orientations were found in the θ-2θ scan. With increasing film thickness the fraction of <100>-oriented grains increased, as estimated from the relative peak intensities.

Film thickness [μm]	d_m [μm]	s_d [%]	Number of grains
0.4	1.00	52	236
0.8	1.13	52	341
1.0	1.51	49	270
3.0	1.45	56	312

Table 4.1: Microstructural parameters for different film thicknesses. The arithmetic mean value and the corresponding standard deviation are denoted by d_m and s_d, respectively.

4.3.2 Monotonic tests

Fig. 4.2 shows the stress-strain behavior as measured by X-ray diffraction up to a total strain of 1.0 % for the 0.4, 0.8, 1.0, and 3.0 μm thick films, respectively. It can be seen that the curves do not start at the origin of the plot because residual stresses were present in the films after sample preparation. The residual stresses of the unstrained specimens after film deposition were between -1 and 100 MPa, and the total strain has been corrected for the amount of the corresponding elastic strain. The curves all show an elastic regime, then the slope of the curves decreases as the films deform plastically. On unloading, the film first

relaxes elastically. The film then becomes subject to compressive stresses and yields at a smaller stress than in tension. The 0.8, 1.0, and 3.0 µm thick films exhibit a very similar stress-strain behavior with a maximum stress of about 300 MPa. The 0.4 µm thick film showed significantly higher stresses with a maximum stress of about 420 MPa. It should be noted that the average stress is tensile during a cycle. The amount of plastic strain ε_{pl} can be determined as the difference between the total strain ε_{tot} and the elastic strain ε_x in the tensile direction that was measured by X-rays. This procedure is illustrated in Fig. 4.3(a) for the 3 µm thick film. The elastic strain ε_x is plotted versus ε_{tot} of the film-substrate composite. The elastic strain increases linearly up to ε_{tot}=0.1 % with a slope m≈1. The slope of the curve then decreases till at a strain of 0.4 % an almost constant value for ε_x is reached. The deviation from linearity corresponds to the onset of plastic deformation in the Cu film. The amount of plastic strain was determined for all film thicknesses (Table 4.2). Only small differences were found, the values were between 0.83 and 0.91 %. The procedure to determine the yield stress is illustrated in Fig. 4.3(b). The yield stress $\sigma_{0.2}$ is highest for the 0.4 µm thick film, whereas it is almost the same for the films of 0.8 and 1.0 µm thickness. The value determined in case of the 3.0 µm Cu film is somewhat smaller. The yield stress depends only weakly on the film thickness, which unusual for thin films on substrates. The plastic strain $\varepsilon_{pl,}$ the residual stresses, and the flow stress $\sigma_{0.2}$ at ε_{pl}=0.2 % are summarized in Table 4.2.

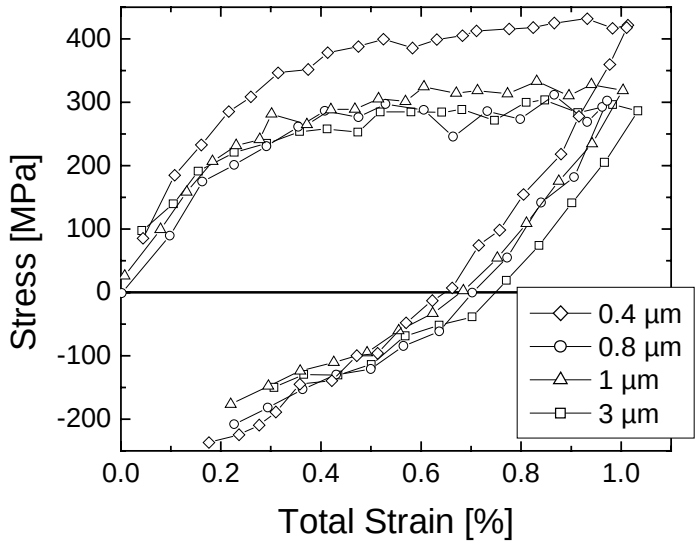

Fig. 4.2: σ-ε behavior determined by microtensile tests in an X-ray diffractometer for 0.4, 0.8, 1.0, 3.0 µm thick Cu films.

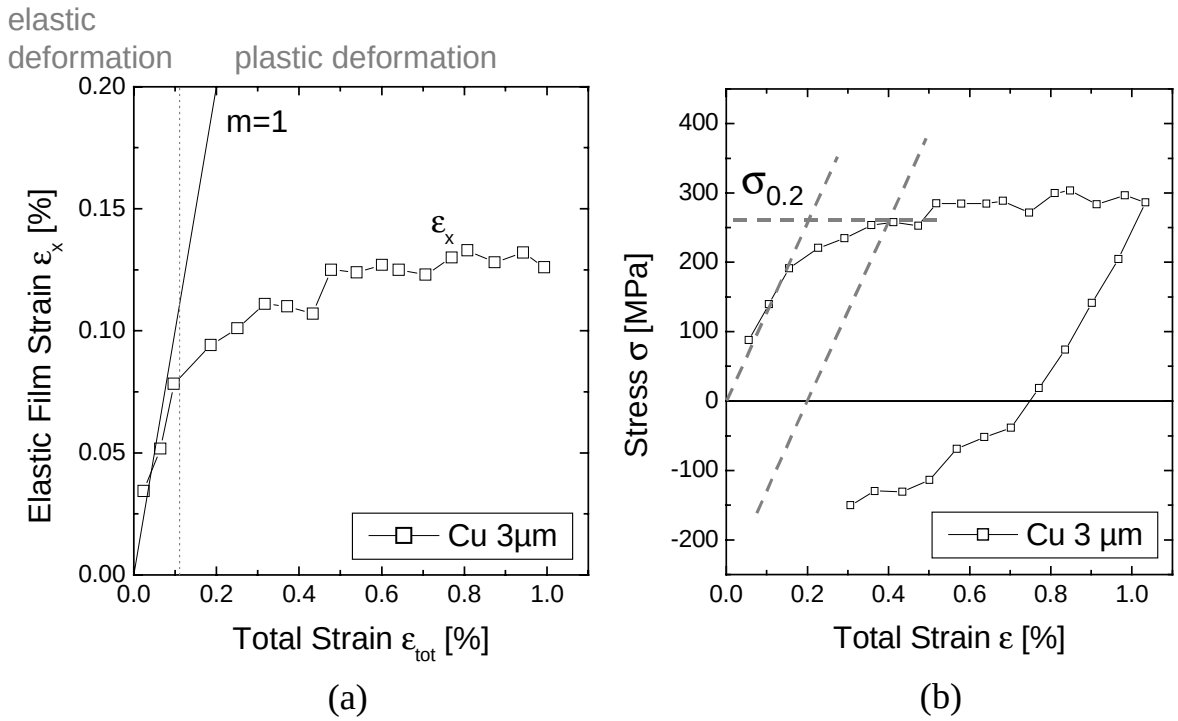

Fig. 4.3: (a) Elastic strain ε_x vs. total strain ε for the 3.0 µm thick Cu film. The deviation from linearity indicates the onset of plastic deformation. (b) Procedure of flow stress determination exemplified for the 3.0 µm thick Cu film.

Film thickness	Residual stress	Plastic strain (%)	Flow stress $\sigma_{0.2}$	Fatigue lifetime
0.4 µm	13 MPa	0.83	325 MPa	880 cycles
0.8 µm	-2 MPa	0.86	290 MPa	800 cycles
1.0 µm	26 MPa	0.87	289 MPa	270 cycles
3.0 µm	97 MPa	0.91	258 MPa	200 cycles

Table 4.2: Summary of mechanical parameters for the different film thicknesses, obtained by microtensile test up to a total strain or strain range of 1.0 %.

4.3.3 Fatigue tests

Fig. 4.4(a) shows the energy loss ΔW per cycle as a function of the number of cycles for a fatigue experiment on the 3.0 µm thick Cu film. Furthermore, the maximum and minimum strains ε_{max} and ε_{min}, respectively, recorded at the maximum and minimum force in a fatigue cycle are plotted in Fig. 4.4(b). The Cu-polyimide specimen was cyclically loaded with a maximum force of 34 N. During the first cycles the hysteresis decreases significantly until after 10 cycles an almost constant value is reached. After 200 cycles, ΔW decreases again and keeps going down until the end of the experiment after 5 000 cycles. We have defined the

lifetimes of the films as the number N_d of cycles to damage formation, which is related to the decrease in energy loss over cycles [31]. The curves describing ε_{max} and ε_{min} both smoothly increase as the gage length increases due to cyclic creep of the polymer substrate. Abrupt increases in gage length are observed after 200 cycles and 2000 cycles, which is consistent with the changes in energy loss in Fig. 4.4(a). The strain range of 1.1 % was constant throughout the fatigue experiment. As a result of these observations, the number N_d of cycles to damage formation was determined to be 200 for this experiment.

In Fig. 4.5(a) ΔW measured for a 0.4 µm thick Cu film is shown. For this experiment, the maximum force was set to 28 N. The scatter in the data is larger than in Fig. 4.4. Nevertheless, a plateau of the curve can be seen after 10 cycles, and, after 880 cycles, ΔW starts to decrease. The number N_d of cycles to damage formation was determined to be 880, which is also in agreement with the strain data (compare Fig. 4.5(b)). The strain range was 1.0 % throughout the test.

Fatigue experiments for different film thicknesses are summarized in Table 4.2. The 1.0 µm thick film sustained 270 cycles, which is more than in case of the 3.0 µm thick film. The fatigue lifetime increased further with decreasing film thickness, to 800 and 880 cycles for the 0.8 µm and the 0.4 µm thick Cu films, respectively.

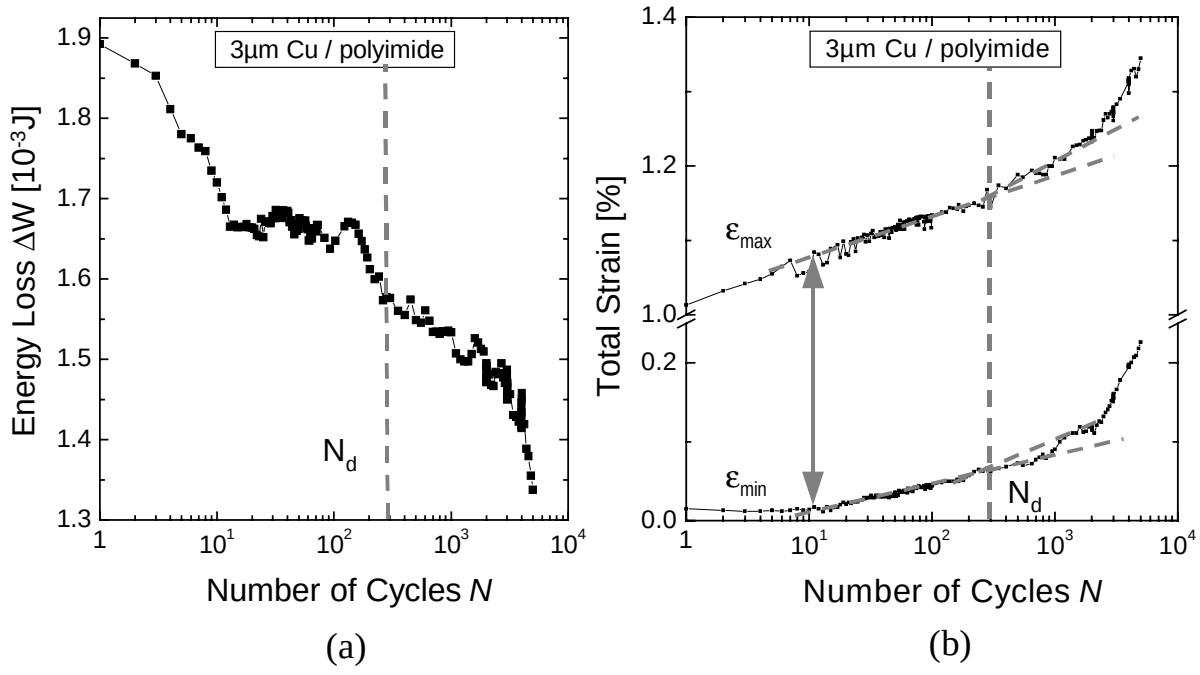

Fig. 4.4: (a) Energy loss ΔW vs. the number N of cycles and (b) the total strain ε_{min} and ε_{max} at the minimum and maximum force in a fatigue cycle (compare Fig. 4.1), respectively, versus N for the 3 µm Cu film on polyimide.

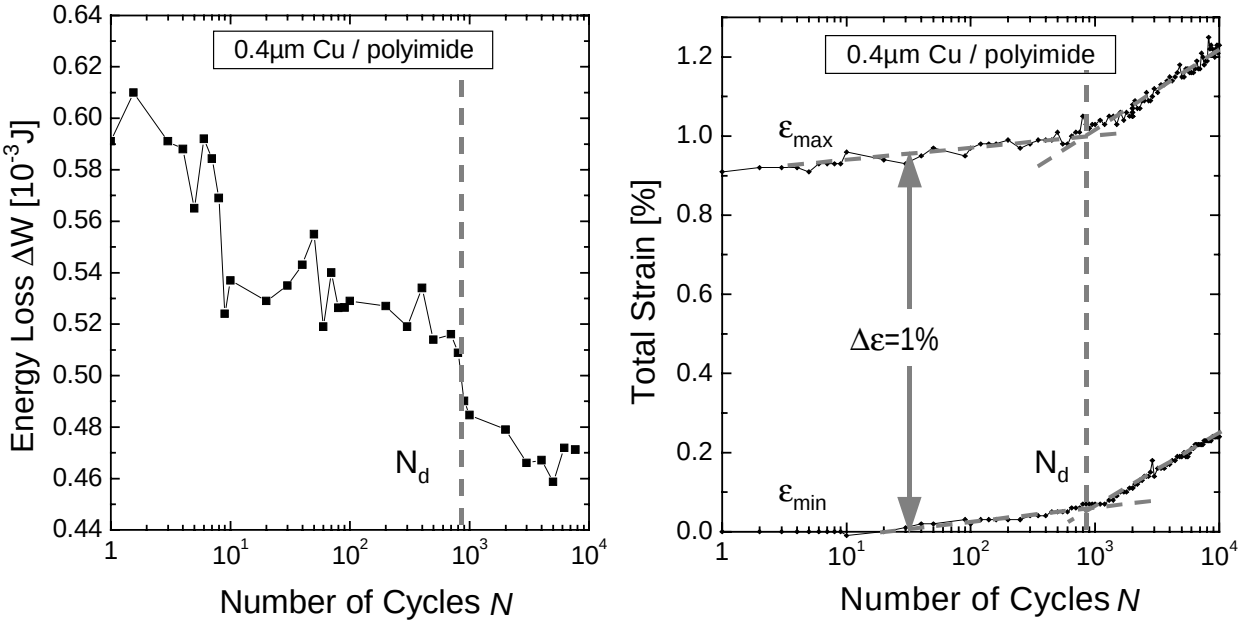

(a) (b)

Fig. 4.5: (a) Energy loss ΔW vs. the number N of cycles and (b) the total strain ε_{min} and ε_{max} at the minimum and maximum force in a fatigue cycle (compare Fig. 4.1), respectively, versus N for the 0.4 µm Cu film on polyimide.

4.3.4 Fatigue Damage

Figs. 4.6(a) and (b) show typical fatigue damage at the film surface, in this case of the 3.0 µm thick film after 5000 cycles. Extrusions and cracks were analyzed by *FIB* microscopy. The extrusions are usually located in individual grains, the cracks (marked by arrows) were found to propagate along grain boundaries. The extrusion height is of the order of 1 µm. Underneath the extrusions, voids were observed at the film-substrate interface as shown in Fig. 4.6(c) and (d). These micrographs show cross-sections cut into extrusions at the locations indicated in Fig. 4.6(a) and (b), respectively. The voids extend from the film-substrate interface towards the surface, and crack-like features extend from the voids towards to surface. Note that there are no intrusions or cracks extending from the surface into the films.

In Fig. 4.7, the damaged surface of the 0.4 µm thick film is shown. Fig. 4.7(a) shows extrusions in large grains and cracks along the grain boundaries. Micrographs of cross-sections that were cut into the Cu film are shown in Figs. 4.7(b) and (c). The positions of the cross-sections have been marked in Fig. 4.7(a). Again, there are voids at the film-substrate interface extending towards the film surface, where extrusions were observed. The extrusion height is significantly smaller compared to the 3.0 µm thick film. Also, fewer extrusions were found compared to the thicker films.

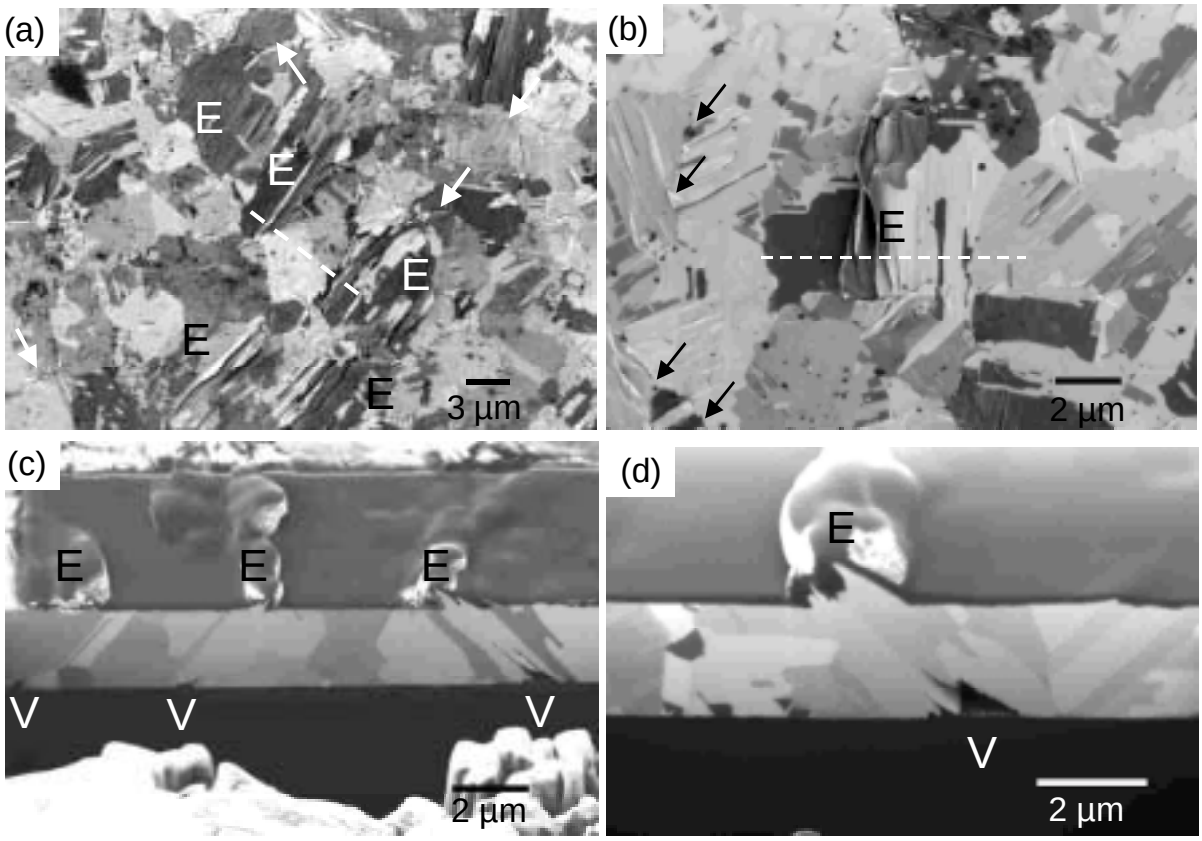

Fig. 4.6: Fatigue damage of the 3.0 µm thick Cu film: (a), (b) Extrusions (marked "*E*") at the film surface and (c), (d) voids (marked "*V*") at the film-substrate interface. The cross-sections were prepared by *FIB* milling; their positions are indicated in (a) and (b), respectively. The cross-section was imaged at a tilt angle of 45°.

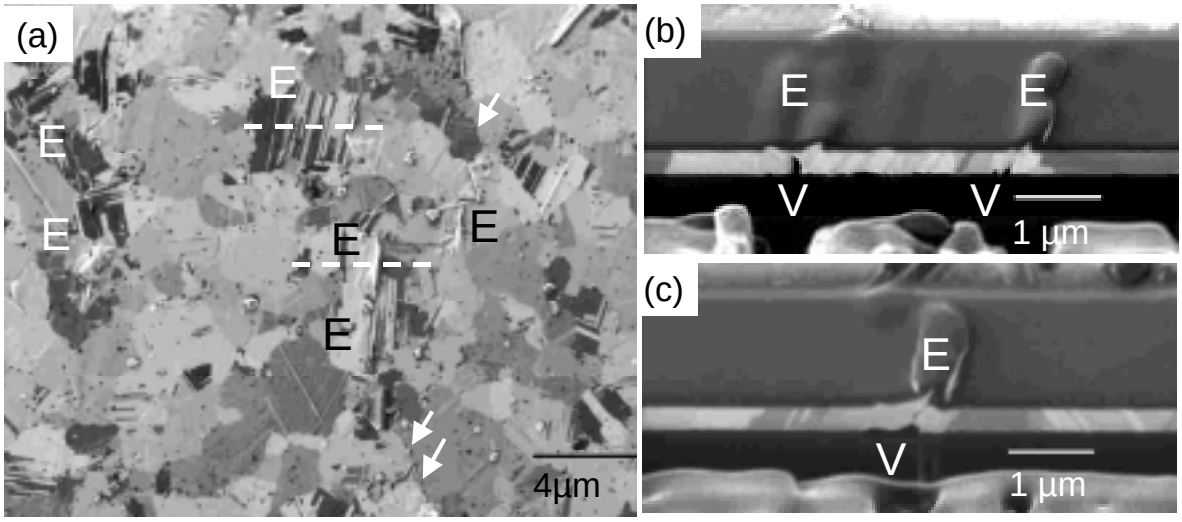

Fig. 4.7: Fatigue damage of a 0.4 µm thick film: (a) Extrusions (marked "*E*") at the film surface and (b) voids (marked "*V*") at the film-substrate interface. The cross-sections were prepared by *FIB* milling and imaged at a tilt angle of 45° in the *FIB* microscope. The positions of the cross-sections are indicated in (a).

The dislocation structure of the 3.0 µm thick Cu film, which was cycled at a total strain range of ~1.1 % was investigated by *TEM*. The polyimide substrate, to which the film is attached, gives only a weak contrast in the microscope (lower surface). Further, the film is covered by a thin tungsten layer to protect the surface during sample preparation (upper surface). The imaged grain shown in Fig. 4.8 has a diameter of about 8 µm. There are voids at the film-substrate interface and extrusions at the surface labeled "V" and "E", respectively. These findings are consistent with the results from *FIB* microscopy. In addition, twins, which are usually present in our Cu films, are denoted by "T" in Fig. 4.8(a). The Cu has a (010) orientation and the dislocation structure is imaged under two-beam diffraction conditions using $\boldsymbol{g}_{(020)}$ and $\boldsymbol{g}_{(\bar{1}11)}$ close to a [101] zone axis, respectively. The cross-section reveals mainly individual dislocations, whereas no long-range order or dislocation cell formation is visible. Due to the projection of the cross-sectional image dislocations on different slip systems differ in line length. Dislocations with a similar line length lie parallel to each other, implying that they belong to the same slip system. In the following, the grain sections A, B, and C, marked in Fig. 4.8, are analyzed separately.

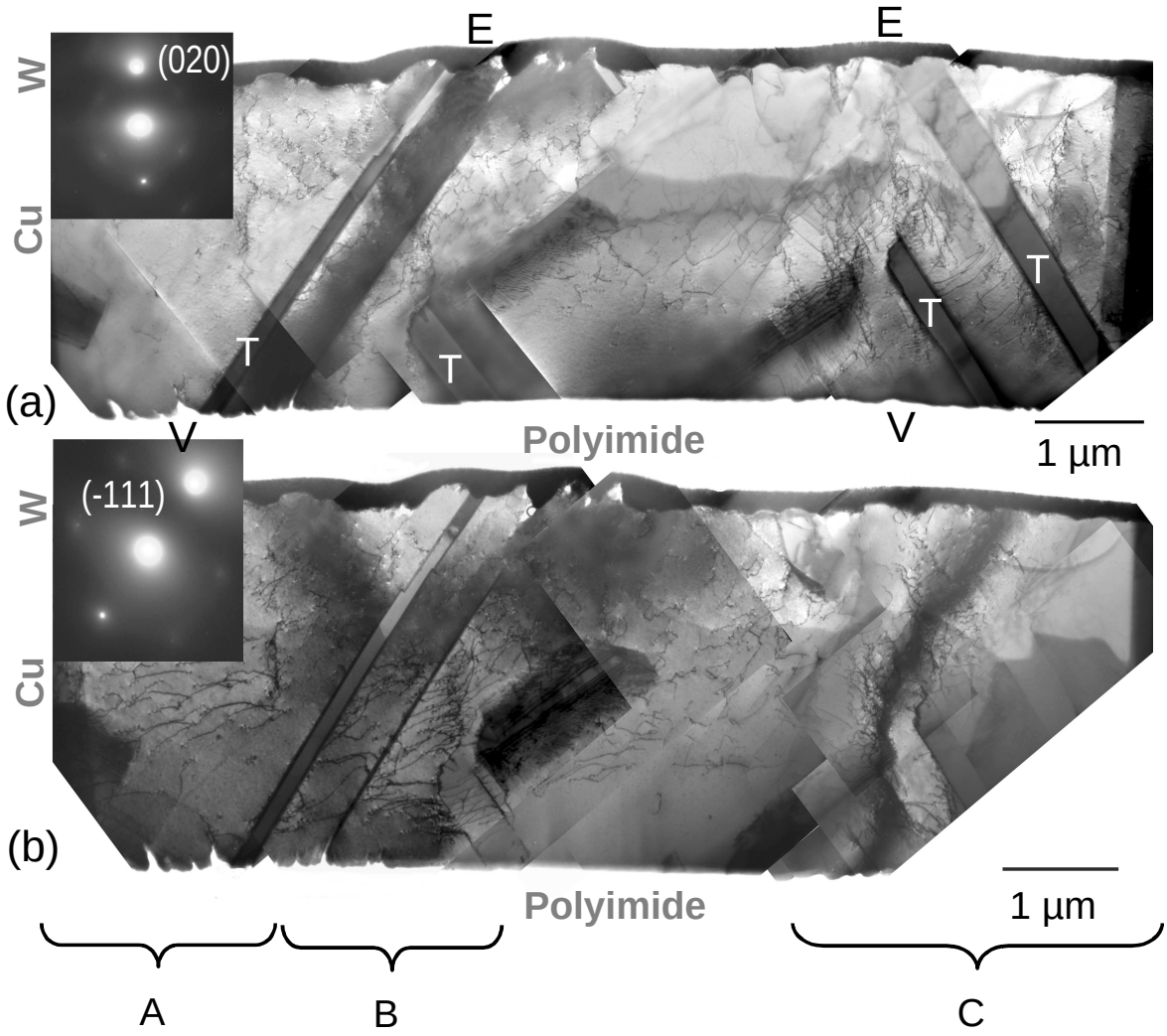

Fig. 4.8: *TEM* image of the 3.0 µm thick Cu film covered by a thin tungsten coating for cross-sectional *TEM* sample preparation. The two-beam bright field images of a (010)-oriented grain were taken at (a) $\boldsymbol{g}_{(020)}$ and (b) $\boldsymbol{g}_{(\bar{1}11)}$ diffraction conditions. The images reveal extrusions (E) at the film surface, voids (V) at the film-substrate interface, and twins (T). The Cu film is attached to the polyimide substrate, which gave no noticeable contrast in the image. For further analysis the image has been subdivided into three regions labelled A, B, and C.

Fig. 4.9 shows the dislocation structure in section A imaged under $\boldsymbol{g}_{020}$ and $\boldsymbol{g}_{\bar{1}11}$ two-beam conditions. Burgers vectors $\boldsymbol{b}$ of dislocations were determined by finding at least two different two-beam conditions fulfilling the invisibility criterion. The dislocations visible in Fig. 4.9(a) possess $\boldsymbol{b}=\frac{1}{2}[\bar{1}10]$ and $\boldsymbol{b}=\frac{1}{2}[0\bar{1}1]$ as illustrated in Fig. 4.9(b). The Burgers vectors of the dislocations in Fig. 4.9(c) and (d) are $\boldsymbol{b}=\frac{1}{2}[\bar{1}10]$ and $\boldsymbol{b}=\frac{1}{2}[\bar{1}01]$. Some dislocations could not be clearly identified because of their short length. The dislocations with $\boldsymbol{b}=\frac{1}{2}[\bar{1}01]$

are bowed and show a rather long line length, whereas dislocations with $\boldsymbol{b}=\frac{1}{2}[\bar{1}10]$ and $\boldsymbol{b}=\frac{1}{2}[0\bar{1}1]$ appear to be short due to the projection.

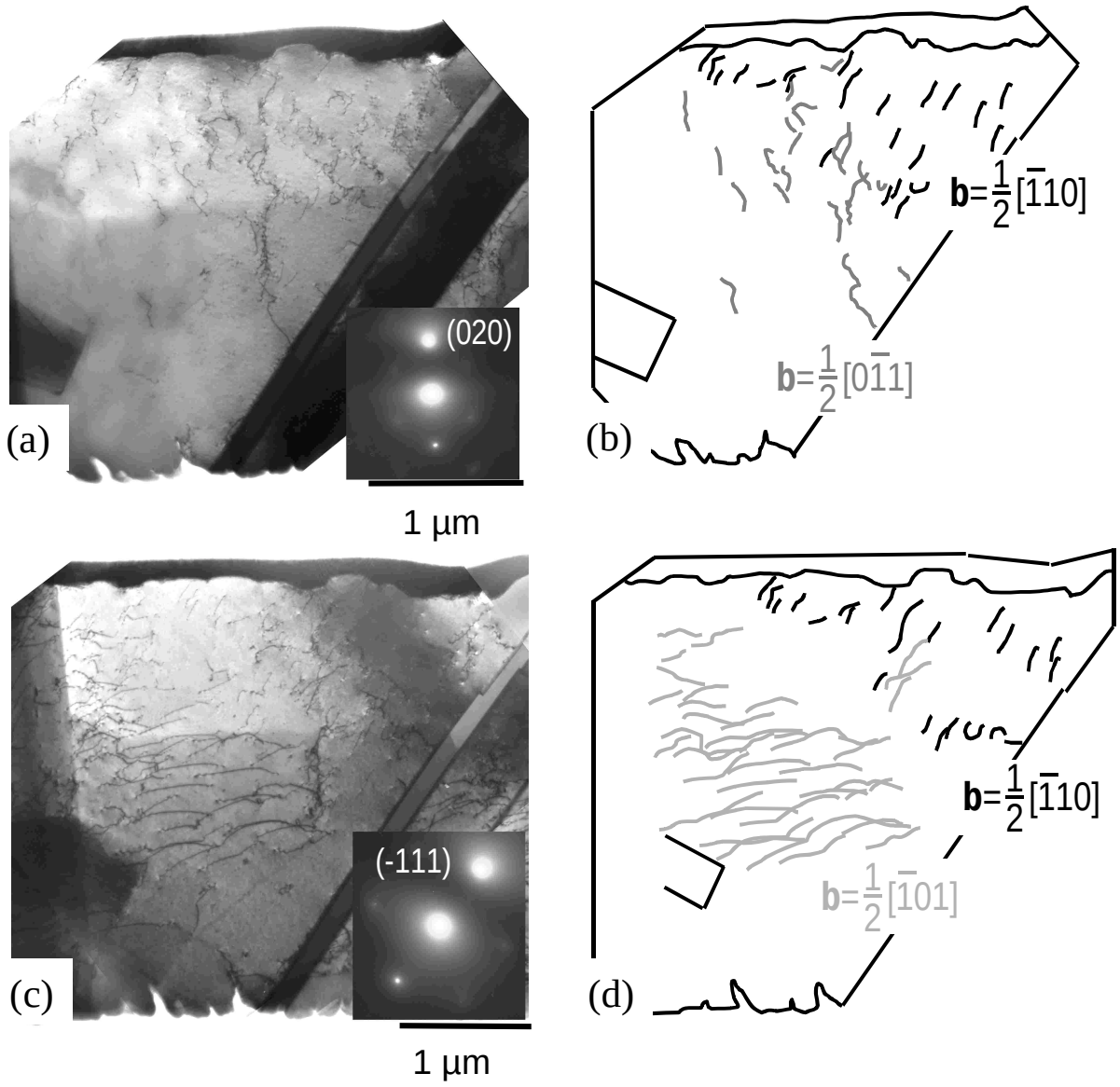

Fig. 4.9: Dislocation configuration of section A (Fig. 4.8) imaged at (a) $\boldsymbol{g}_{020}$ and (c) $\boldsymbol{g}_{\bar{1}11}$ (b) and (d) are the corresponding schematic drawings of the dislocations under consideration of their Burgers vectors.

Small dislocation half loops were found at twin boundaries; these dislocations have mainly $\boldsymbol{b}=\frac{1}{2}[\bar{1}01]$, but also dislocation half loops of $\boldsymbol{b}=\frac{1}{2}[\bar{1}10]$ were observed to bow out of the twin boundary (Fig. 4.10(a),(b), see arrows). Furthermore, dislocations were observed to be constrained by the twin boundaries (see Fig. 4.10(c)). These dislocations are mainly of type $\boldsymbol{b}=\frac{1}{2}[\bar{1}10]$.

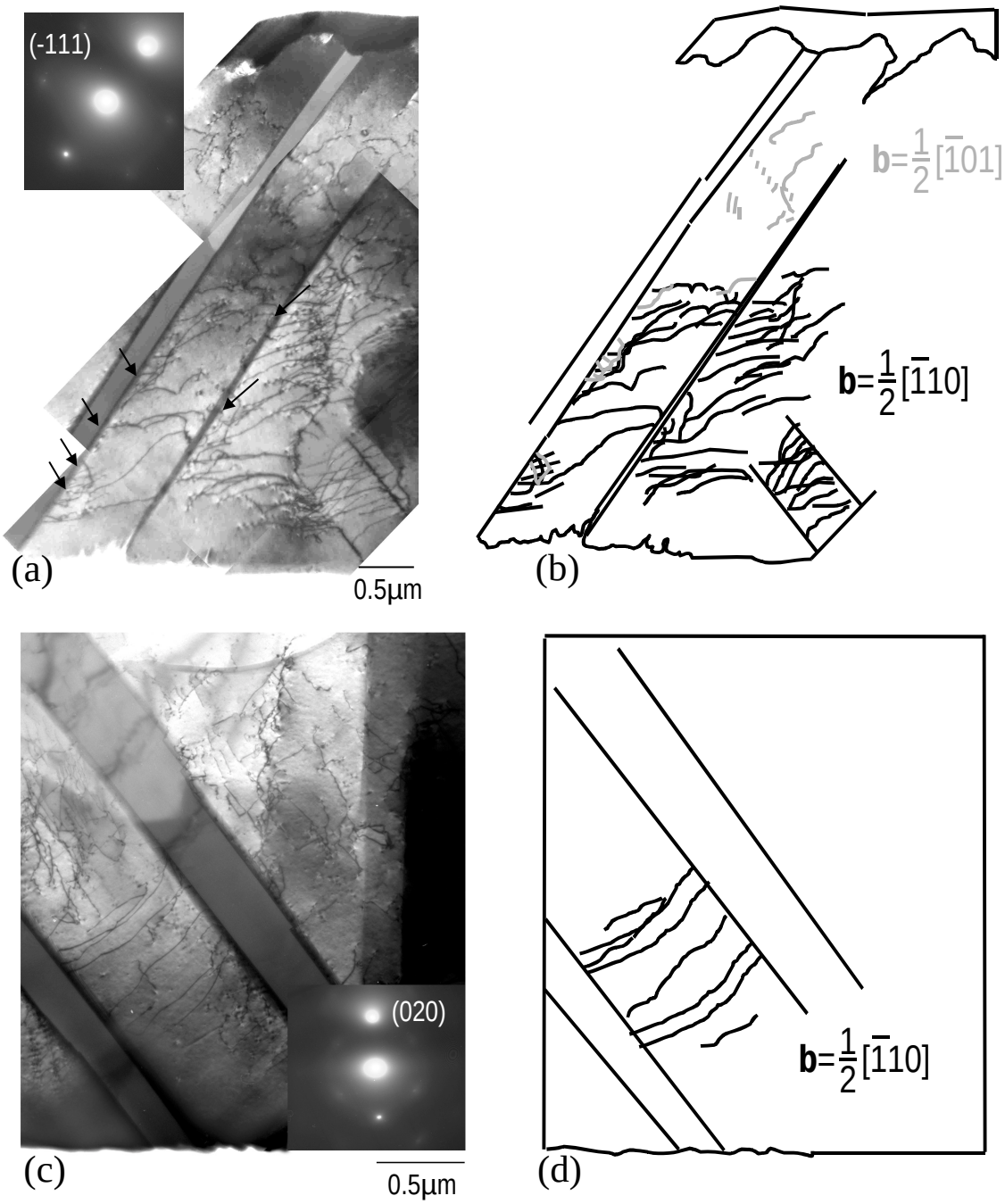

Fig. 4.10: (a) Micrograph of section B in Fig. 4.8 imaged with $\boldsymbol{g}_{\bar{1}11}$. Parallel dislocations with $\boldsymbol{b}=\frac{1}{2}[\bar{1}10]$ and $\boldsymbol{b}=\frac{1}{2}[\bar{1}01]$ are bowed between twin boundaries. (b) Schematic drawing of the dislocation structure shown in (a). (c), (d) *TEM* image and corresponding schematic drawing of section C Fig. 4.8 imaged with $\boldsymbol{g}_{020}$. Dislocations can be seen to expand between the twin boundaries.

In addition to grains exhibiting obvious extrusions, also grains that seemed to be undamaged after the fatigue tests according to *FIB* imaging were investigated by *TEM*. Fig. 4.11 shows a (111) oriented grain with a rather rough surface, but no distinct extrusions or voids have been found. The grain is about 6 µm in diameter and expands over the complete

film thickness of 3.0 µm. However, near the surface and near the interface the grain is twinned (labeled "T" in Fig. 4.11). Imaging with $\boldsymbol{g}_{020}$ close to a [101] zone axis shows an inhomogeneous dislocation distribution in the grain. Two sections, A and B, were seen to have a high dislocation density separated by a region of 2 µm width, which is nearly devoid of dislocations. In these sections, arrays of parallel dislocations lie on different glide planes and thus show different line length in the cross-sectional *TEM* image.

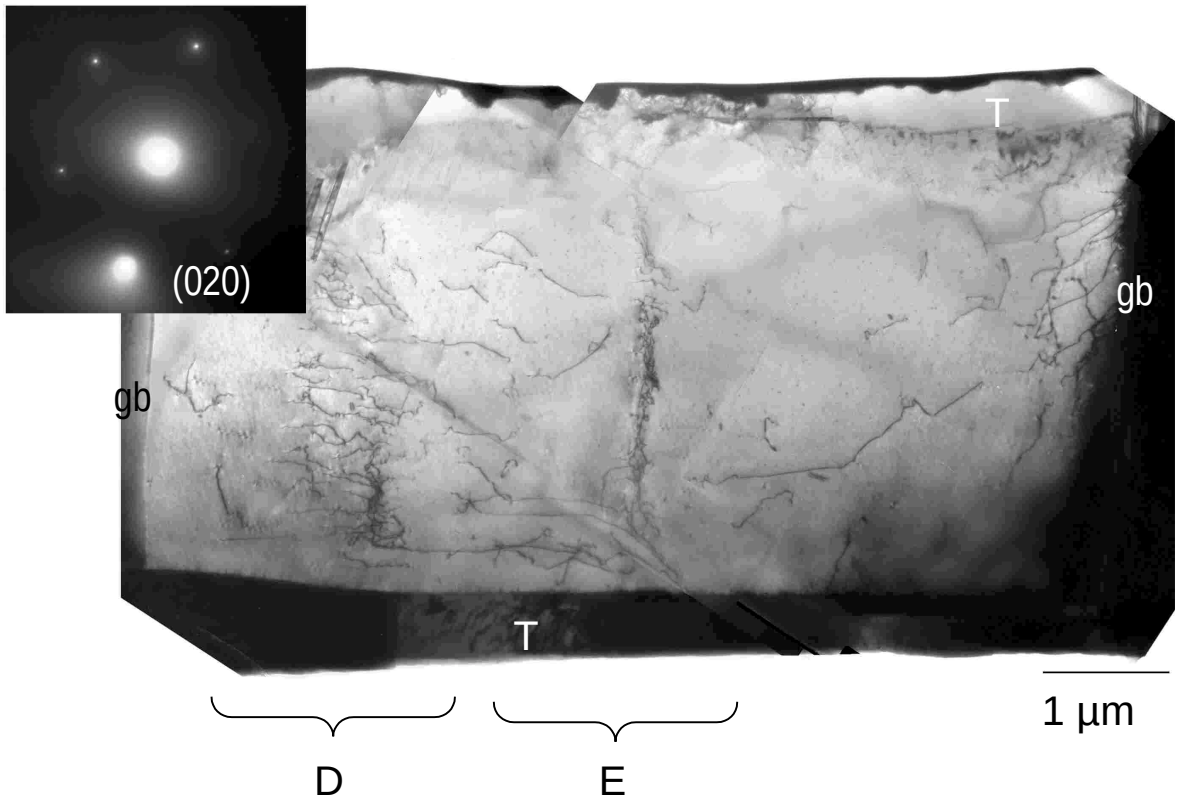

Fig. 4.11: *TEM* image of a (111) oriented grain in the 3.0 µm thick Cu film on polyimide after the fatigue test. The image was taken under $\boldsymbol{g}_{020}$ two-beam conditions. Here, no voids were seen at the interface. Twins and grain boundaries are labeled "T" and "gb", respectively. The thin dark layer at the surface of the Cu film is a protective layer of tungsten necessary for the *TEM* sample preparation. The Cu film is attached to the polyimide substrate. The image has been subdivided into parts D and E (see Fig. 4.12).

Fig. 4.12 shows the dislocation structure of sections D and E at a higher magnification. The dislocations in section D were found to have Burgers vector $\boldsymbol{b}=\frac{1}{2}[\bar{1}10]$. A bright-field image taken under $\boldsymbol{g}_{020}$ two-beam conditions and the corresponding schematic drawing are presented in Fig. 4.12(a), (b). The dislocation array of section E was imaged with $\boldsymbol{g}_{020}$ and $\boldsymbol{g}_{200}$ two-beam conditions close to a [101] and [011] zone axis, respectively, (Fig.

4.12(c), (d)). The dislocations of the array have Burgers vector $\boldsymbol{b}=\frac{1}{2}[101]$ and $\boldsymbol{b}=\frac{1}{2}[011]$, while a few dislocations with $\boldsymbol{b}=\frac{1}{2}[\bar{1}10]$ were observed close to the intersection of the dislocation array with the twin boundary (Fig. 4.12(e)).

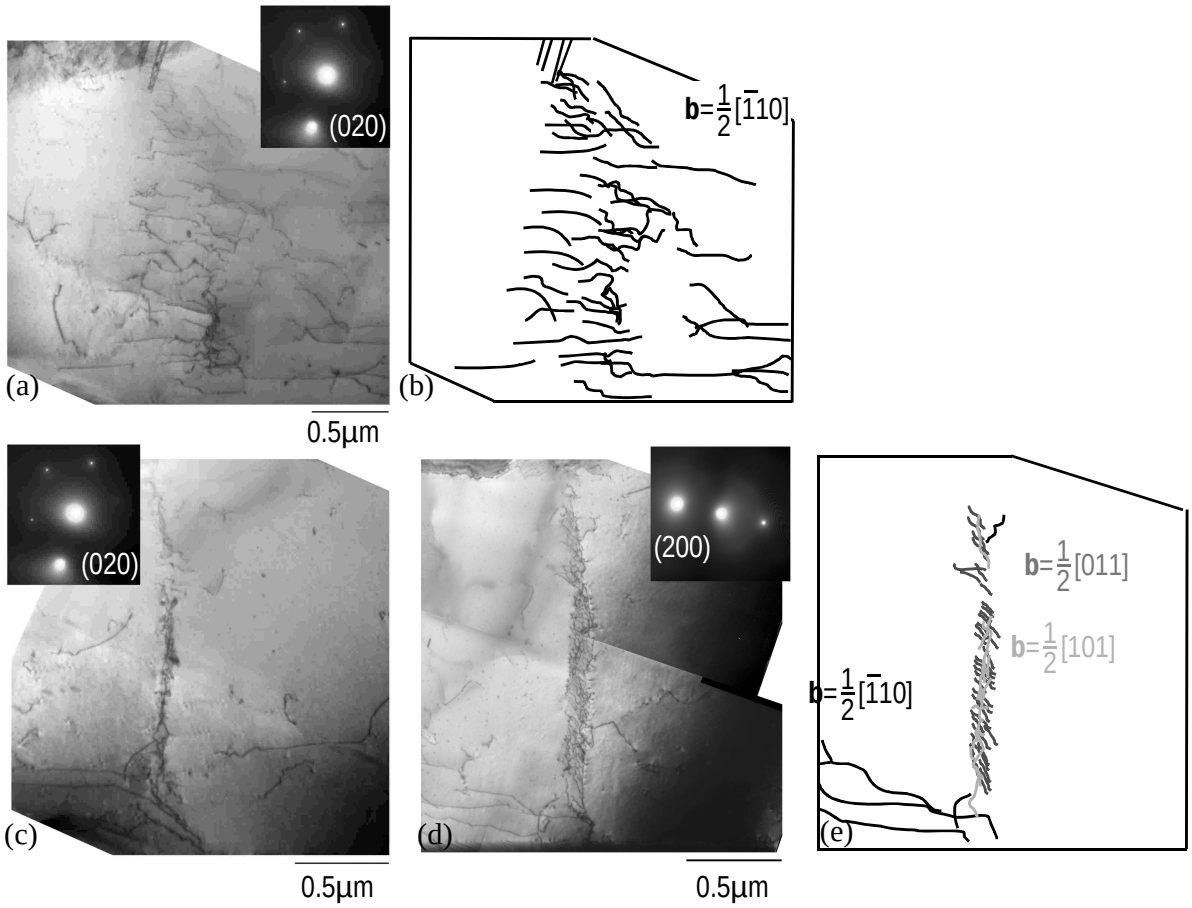

Fig. 4.12 (a), (b) Bright-field *TEM* image under $\boldsymbol{g}_{020}$ and schematic of the dislocation array in section D of Fig. 4.11 of the (111) oriented grain. The dislocations were found to have mainly Burgers vector $\boldsymbol{b}=\frac{1}{2}[\bar{1}10]$. (c), (d), (e) *TEM* images and drawing of dislocations in section E of Fig. 4.11. Dislocations with three different Burgers vectors were identified; dislocation array consists mainly of dislocations with $\boldsymbol{b}=\frac{1}{2}[101]$ and a few dislocations with $\boldsymbol{b}=\frac{1}{2}[011]$. In addition, a few long dislocations with $\boldsymbol{b}=\frac{1}{2}[\bar{1}10]$can be seen close to the dislocation array.

4.4 Discussion

4.4.1 Fatigue lifetime

Before discussing the fatigue life of thin Cu films investigated in this study, we will briefly recall the presentation of fatigue life in terms of the strain amplitude. Fig. 4.13 schematically shows a double-logarithmic plot of the total strain amplitude ε_a versus the number of load reversals $2N_f$ to failure. The fatigue life N_f of a material depends on the elastic as well as on the plastic strain amplitudes, ε_{ae} and ε_{ap}, respectively, (eg. [32]):

$$\varepsilon_a = \varepsilon_{ae} + \varepsilon_{ap} = \frac{\sigma_f'}{E}(2N_f)^{c_s} + \varepsilon_f'(2N_f)^{c_d} \qquad (4.2),$$

where E is Young's modulus, σ'_f the fatigue strength coefficient, ε'_f the fatigue ductility coefficient, c_s the fatigue strength exponent, and c_d the fatigue ductility exponent. The asymptotic behavior of the strain-life (black dashed curve in Fig. 4.13) is shown by solid lines and described by the *Coffin-Manson* [32] and the *Basquin* law [33], respectively. The coefficients σ'_f and ε'_f are related to the strength and ductility of a material, respectively.

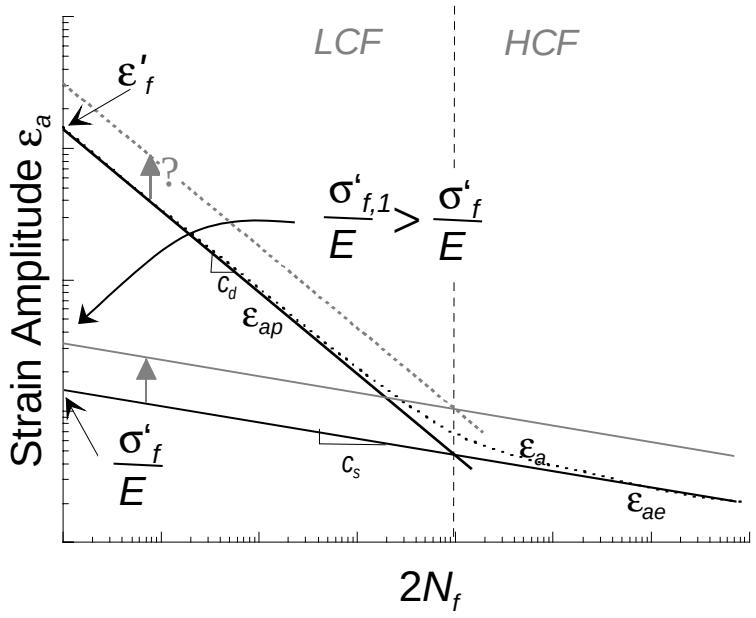

Fig. 4.13: Schematic of a strain-life diagram. The total strain amplitude ε_a is plotted versus the number $2N_f$ of load reversals to failure. At 10^4 cycles the transition from low cycle fatigue (*LCF*) to high cycle fatigue (*HCF*) occurs. The dark solid lines correspond to the elastic and plastic strain amplitude, ε_{ae} and ε_{ap}, respectively. σ'_f and ε'_f are the fatigue strength and fatigue ductility coefficients, respectively.

In thin film materials, the reduction of the thickness and/or the grain size leads to an increase in strength of the specimen. Therefore, σ'_f is expected to increase with decreasing film thickness and/or grain size, shifting the *HCF* curve to enhanced fatigue lives as shown in Fig. 4.13. Indeed, an increase in the *HCF* life was observed in stress-controlled fatigue tests of thin Cu foils of 100 and 20 µm thickness [20]. The fatigue life of the foils was reported to increase by a factor of 10, when the foil thickness was reduced by a factor of 5. Investigations of thin Ag films showed that the stress-amplitude necessary to induce fatigue damage was higher for decreasing film thickness (see chapter 3). It is, however, not clear yet, how the *LCF* life and accordingly the ductility ε'_f and will be affected by smaller film thickness and/or grain size. The investigations in this work serve to further clarify this point.

Coarse-grained Cu films with different thicknesses were fatigued in the low cycle/high strain region with a plastic strain range $\Delta\varepsilon_{pl}$ of ~1 %. The fatigue life was found to increase with decreasing film thickness (compare Table 4.2). The effect of the film thickness is small in case of the 3.0 and 1.0 µm thick films, respectively, but compared to the 0.8 µm and 0.4 µm thick ones an increase of the fatigue life by a factor of 4 was observed.

For a comparison the experimentally determined fatigue lives of the films investigated in this work and of fine-grained Cu films studied by Kraft *et al.* [31] are illustrated in Fig. 4.14. In Ref. [31] Cu films with a thickness comparable to the films in this study but smaller grains were fatigued at different ranges of plastic strain. The data are shown as a *Coffin–Manson* plot with $\Delta\varepsilon_{pl}$ plotted versus the number N_f of cycles to failure.

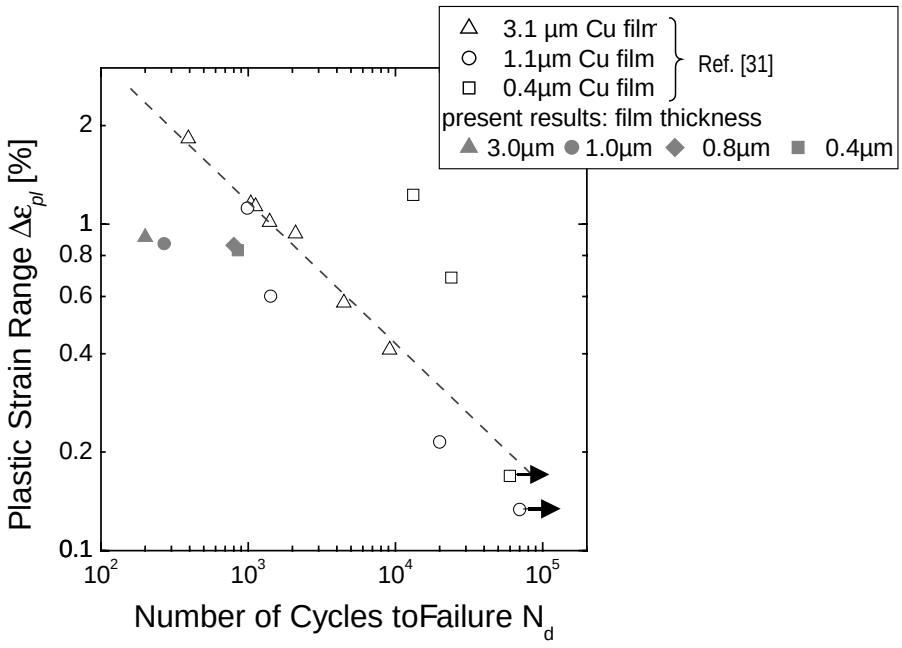

Fig. 4.14: *Coffin-Manson* plot comparing the fatigue behavior of coarse- and fine-grained thin Cu films [31].

The main points can be stated as follows: The lifetime of the 3.0 µm thick film of this work with a mean grain size of 1.45 µm was an order of magnitude smaller than the lifetime of Cu films with a grain size of about 800 nm having almost the same thickness. Similarly, the fatigue life of the 0.4 µm thick films with a grain size of ~280 nm was longer than in case of a coarser-grained specimen of the same thickness with a mean grain size of 1.0 µm. From these observations, we conclude that also in the *LCF* regime, which is controlled by the cyclic ductility, the fatigue endurance of thinner films on a substrate is enhanced. The mechanisms responsible for the formation of damage, and how it is affected by the characteristic dimensions of a thin film will be discussed below.

4.4.2 Microstructure and damage mechanisms

The dislocation structure in the interior of differently oriented grains of the 3.0 µm thick film was investigated by *TEM*; the results obtained on two of them have been presented above. This is, however, a small number of grains, and it is therefore difficult to deduce the general behavior of dislocations during fatigue of thin films. But, nevertheless, it is possible to see some trends and differences to previous work.

The interior of the (100) grain, which was about 8 µm wide, was filled by a network of individual dislocations, suggesting that the whole grain was deformed in the course of cyclic deformation. This is not in accordance with previous work performed on Cu foils of 25 and 33 µm thickness [22], where cell structures were observed in grains larger than 2 µm. Therefore, in films thinner than 3.0 µm it is reasonable not to expect any long-range order, but only individual dislocations. We clearly see differences to the dislocation structure in bulk fatigued Cu, where the self-organization of dislocations results in the formation *PSB*s and well-defined cell structures at intermediate and high cyclic plastic strains, respectively. At room temperature these dislocation structures typically extend over several micrometers with typical dimensions in the range of 1 or 2 microns [16], [17].

The interpretation of the results obtained for the (111)-oriented grain is conflicting: The dislocations can be interpreted as individual ones as well as to be part of an almost regular structure, because regions devoid of dislocations separated by “dislocation walls” can be seen (compare Fig. 4.11 and Fig. 4.12). The “walls” are rather ill-defined, but their distance, indeed, is comparable to typical cell sizes of bulk [17] as well as Cu foils [22].

In bulk, surface extrusions often precede fatigue failure, both in single crystals and in grains of polycrystalline material. This is similar to observations of fatigued thin Ag films, where extrusions and voids, but no cracks, were observed after cyclic deformation at a small number of cycles [34]. The (100)-oriented grain in this work shows extrusions at the surface,

which are similar to those in fatigued bulk Cu. Although in case of the (111) grain no clear slip lines were seen at the surface, the surface roughness is absolutely comparable to the height of the extrusions of the (100) oriented grain (compare Fig. 4.8 and Fig. 4.11). The extrusions at the surface of the (100) grain do not appear to have any obvious correlation with the dislocation structure in the interior (see Fig. 4.8 - Fig. 4.10), which in bulk is generally accepted to be an indicator for multiple slip in single- as well as polycrystalline materials.

Further, in the (100)-oriented grain voids were found at the interface, which were also observed by *FIB* microscopy, whereas no voids were found in the (111)-oriented grain. An explanation for the observation that no voids are formed in (111) oriented grains has been given in chapter 3 for the case of Ag films on SiO_2 substrates. Briefly, the damage process in thin film fatigue is based on a "channeling" mechanism of dislocations in a thin film [35] and the annihilation of edge dislocations of opposite sign encountering at a critical distance of 1.6 nm [36]. When dislocations move through the films during cyclic deformation dislocations of opposite signs are deposited at the film-substrate interface. These interface dislocations are pure screws in case of (111) oriented grains when the primary slip systems are taken into account, the annihilation of which does not result in the formation of vacancies. Therefore, no voids nucleate in (111) oriented grains. Whether this generally applies to a larger number of grains in the Cu films investigated is not clear to date, but further investigations are on the way.

In our previous studies of thin film fatigue it has been reported that voids form close to the film-substrate interface due to cyclic deformation [37]. Reports of void formation in bulk are rare and controversial; in Al large voids of about 100 nm aligned along the active slip trace have been observed by Yamamoto *et al.* [38] and Ogura and Karashima [39]. Small defect clusters have been found by Piqueras *et al.* [40], who interpreted their observations as agglomerates of vacancies. Antonopoulos and Winter [41] showed that the loops in their foils were faulted dipoles. Further, Antonopoulos *et al*. [42] showed that the dipoles in foils from copper crystals fatigued into early saturation were predominantly of vacancy type. Also, electrical resistivity annealing measurements [43], [44] indicated that vacancies and their agglomerates occur in the course of cyclic deformation.

In our fatigued thin films on substrates vacancies appear to play an important role, as the voids formed at the interface are some 100 nm in size. We have found extrusions and voids in all film thicknesses, but the extrusions were smaller and fewer in the 0.4 µm thick film, which was also found in fatigue studies of thin Ag films (see chapter 3). Neither voids nor extrusions were observed in 0.4 µm films with a median grain size of 0.3 µm [31]. Those films failed

due to cracks along the grain boundaries. Therefore, the process responsible for the formation of voids and extrusions is influenced by the film thickness and the grain size, which is also reflected in the fatigue resistance of the thin films (see 4.4.1).

The effect of the film thickness and the grain size in thin film fatigue can be rationalized considering the mechanisms responsible for the formation of voids and extrusions in thin films proposed by Schwaiger and Kraft [37], which has been briefly described in chapter 3, and the mobility of vacancies. According to this model, nucleation and growth of voids are seen as the dominant failure mechanism in thin films. Apparently during cyclic deformation of thin films, the role of vacancies is more important than in cyclic deformation of bulk materials. This might be due to the fact that the interface between the film and the substrate does not act as a sink or source for point-defects as discussed for diffusional creep in thin films [45], [46], and a sufficiently high concentration of vacancies should be obtained.

The nucleation of voids due to vacancy condensation is possible if a supersaturation of vacancies exists at least in some localized region. The concentration of vacancies in metals, for instance after cold work, is as high as 10^{-4} [47]. Furthermore, the measurements of electrical resistivity of fatigued copper [43] showed that the plastic straining of 2×10^{-4} per cycle increased the concentration of vacancies by 5×10^{-8} per cycle.

As resistivity measurements in bulk indicate, simultaneously with the formation of the dislocation structures point defects are produced. The mechanism for point defect production consists of non-conservative motion of the jogs on screw dislocations as well as the mutual annihilation of two opposite edge dislocations moving on adjacent slip planes. As the vacancies are highly mobile at room temperature the excess vacancy concentration depends strongly on the density of sinks. In a thin film, strongly adherent to a substrate, the diffusion of vacancies can be accomplished if, beside dislocations, the surface as well as the grain boundaries act as sinks for vacancies.

In Fig. 4.15(a) a simplistic schematic of a columnar grain structure of a thin film on a substrate is shown. Close to the film-substrate interface vacancies form due to dislocation annihilation and diffuse simultaneously to the surface and grain boundaries. However, with increasing cycles the vacancy concentration also increases (compare Fig. 4.15(b)), until a critical vacancy concentration C_v^{crit} at N_d cycles is obtained and vacancy condensation takes place. From Figs. 4.15(a) and (b) it becomes clear immediately, that the diffusion length is smaller for thinner films and the vacancies reach the surface more quickly. Equally, for smaller grains the vacancies might to a large extent reach the grain boundary and the build-up of the critical vacancy concentration C_v^{crit} is retarded. This is confirmed by our findings that

extrusions and voids are preferentially found in the large grained Cu film, whereas in case of the 0.4 µm thick film with very fine grains investigated by Kraft *et al.* [31] no extrusions were observed.

These arguments can explain our observations that thinner and finer-grained films are more fatigue resistant. However, more investigations on films with different thicknesses and grain sizes are necessary to better understand the microscopic processes responsible for fatigue failure.

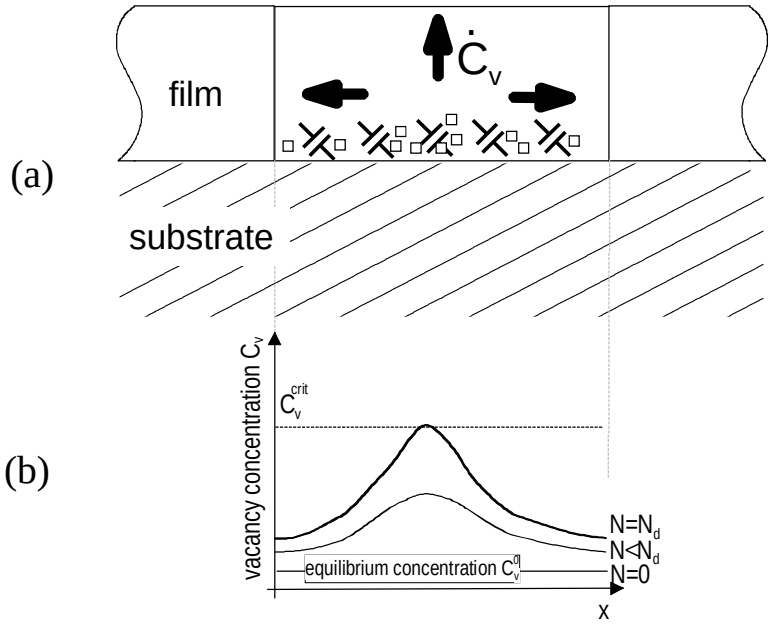

Fig. 4.15: (a) Schematic of a columnar grain structure. Close to the interface between film and substrate vacancies are created by dislocation annihilation. Simultaneously, the vacancies diffuse to the surface and grain boundaries (as indicated by $\dot{C}_V$). The interface does not act as sink or source for vacancies (see Refs. [45], [46]). With decreasing film thickness and grain size the diffusion length is reduced and vacancies reach the sinks more quickly. (b) With increasing cycles N the vacancy concentration increases from the equilibrium concentration at N=0 up to the critical value C_v^{crit} at $N=N_d$, the number of cycles to failure. As soon as C_v^{crit} is achieved vacancy condensation starts and voids nucleate close to the film-substrate interface, which we believe to be the main reason for thin film fatigue failure.

4.5 Summary and conclusions

The present study describes microscopic features of fatigued thin polycrystalline Cu films and effects of microstructural parameters on the fatigue resistance. Cu films with thicknesses

ranging from 0.4 to 3.0 µm were fatigued with a plastic strain range of about 0.9 %. The main findings can be summarized as follows:

(1) Similar to bulk material, extrusions were observed at the film surface after fatigue. The extrusions were related to voids close to the film-substrate interface. Voids and extrusions were observed in all film thicknesses. The height of the extrusions scales with the film thickness.

(2) *TEM* investigations of the 3.0 µm thick Cu film showed that the dislocation structures were different in differently oriented grains. Rather individual dislocations than a well-defined long range order were found.

(3) Film thickness and grain size affect the fatigue life in the *LCF* region. With decreasing film thickness and/or grain size the fatigue life increases.

(4) We believe that void formation is the major cause for thin film fatigue failure. Vacancies are created by dislocation annihilation close to the film-substrate interface and diffuse simultaneously to the surface and grain boundaries. After certain cycle numbers a supersaturation of vacancies is achieved close to the interface and vacancy condensation takes place. It is argued that the reduced diffusion length due to a small film thickness or grain size is responsible for the increased fatigue life of thin and fine-grained Cu films.

In summary, important steps have been made towards understanding fatigue behavior of thin films. An understanding of fatigue mechanisms may lead to an intelligent selection of materials and an improvement in reliability and performance of thin film components.

4.6 Acknowledgements

This work was partially supported by the Deutsche Forschungsgemeinschaft under contract Ar 201/5-2. The support of Dr. G. Dehm, who provided training at the Transmission Electron Microscope, is gratefully acknowledged. We also acknowledge the support of R. Völker, who prepared the Cu thin films.

4.7 References

1. Laird, C., Charsley, P. and Mughrabi, H., "Low Energy Dislocation Structures Produced by Cyclic Deformation", *Mater. Sci. Eng.* **81**, 433-450 (1986).
2. Basinski, Z. S. and Basinski, S. J., "Fundamental aspects of low amplitude cyclic deformation in face-centered cubic crystals", *Progress in Materials Science* **36**, 89-148 (1992).

3. Mughrabi, H., Ackermann, F. and Herz, K., "Persistent slipbands in fatigued face-centered and body-centered cubic metals", in *Fatigue Mechanisms* (Special Technical Publication 675, ASTM, Philadelphia, PA, (1979)), pp. 69-97.
4. Ackermann, F., Kubin, L. P., Lepinoux, J. and Mughrabi, H., "The dependence of dislocation microstructure on plastic strain amplitude in cyclically strained copper single crystals", *Acta Metall.* **32** (5), 715-725 (1984).
5. Laird, C., Finney, J. M. and Kuhlmann-Wilsdorf, D., "Dislocation Behavior in Fatigue VI: Variation in the Localization of Strain in Persistent Slip Bands", *Mater. Sci. Eng.* **50**, 127-136 (1981).
6. Basinski, Z. S., Korbel, A. S. and Basinski, S. J., "The temperature dependence of the saturation stress and dislocation substructure in fatigued copper single crystals", *Acta Metall.* **28**, 171-207 (1980).
7. Winter, A. T., "A model for the fatigue of copper at low plastic strain amplitudes", *Phil. Mag.* **30**, 719-738 (1974).
8. Finney, J. M. and Laird, C., "Strain localization in cyclic deformation of copper single crystals", *Phil. Mag.* **31**, 339-366 (1975).
9. Woods, P. J., "Low-amplitude fatigue of copper and copper -5 at.% aluminium single crystals", *Phil. Mag.* **28**, 115-191 (1973).
10. Lukás, P., Klesnil, M. and Krejcí, J., "Dislocations and Persistent Slip Bands in Copper Single Crystals Fatigued at Low Stress Amplitude", *Phys. Stat. Sol.* **27**, 545 (1968).
11. Rasmussen, K. V. and Pedersen, O. B., "Fatigue of copper polycrystals at low plastic strain amplitudes", *Acta Metall.* **28**, 1467-1478 (1980).
12. Mughrabi, H. and Wang, R., "Cyclic deformation of face-centered cubic polycrystals: a comparison with observations on single crystals", in *Deformation of Polycrystals: Mechanisms and Microstructures*, edited by Hansen, N., Horsewell, A., Leffers, T. and Lilholt, H. (2nd Risø International Symposium on Metallurgy and Materials Science, Risø National Laboratory, Roskilde, Denmark pp. 87-98.
13. Winter, A. T., Pedersen, O. B. and Rasmussen, K. V., "Dislocation microstructures in fatigued copper polycrystals", *Acta Metall.* **29**, 735-748 (1981).
14. Llanes, L. and Laird, C., "Substructure evolution of copper polycrystals under different testing conditions: conventional control and ramp loading", *Mater. Sci. Eng. A* **161** (1), 1-12 (1993).
15. Liu, C. D., Bassim, M. N. and You, D. X., "Dislocation structures in fatigued polycrystalline copper", *Acta Metall. Mater.* **42** (11), 3695-3704 (1994).

16. Grosskreutz, J. C. and Mughrabi, H., "Description of the work-hardened structure at low temperature in cyclic deformation", in *Constitutive equations in plasticity* (The MIT Press, Cambridge, MA, (1975)), pp. 251-325.
17. Feltner, C. E. and Laird, C., "Cyclic stress-strain response of fcc metals and alloys - II Dislocation structures and mechanisms", *Acta Metall.* **15**, 1633-1653 (1967).
18. Kayali, E. S. and Plumtree, A., "Stress-substructure relationships in cyclically and monotonically deformed wavy slip mode metals", *Metall. Trans. A* **13**, 1033-1041 (1982).
19. Judelewicz, M., "Cyclic deformation of 100 µm thin polycrystalline copper foils", *Scripta Metall. Mater.* **29**, 1463-1466 (1993).
20. Judelewicz, M., Künzi, H. U., Merk, N. and Ilschner, B., "Microstructural development during fatigue of copper foils 20-100 µm thick", *Mater. Sci. Eng. A* **186**, 135-142 (1994).
21. Merchant, H. D., Minor, M. G. and Liu, Y. L., "Mechanical Fatigue of Thin Copper Foil", *J. Electronic Mater.* **28** (9), 998-1007 (1999).
22. Hong, S. and Weil, R., "Low cycle fatigue of thin copper foils", *Thin Solid Films* **283**, 175-181 (1996).
23. Read, D. T., "Tension-tension fatigue of copper thin films", *Int. J. Fatigue* **20** (3), 203-209 (1998).
24. Hofbeck, R., Hausmann, K., Ilschner, B. and Künzi, H. U., "Fatigue of very thin copper and gold wires", *Scripta Metall.* **20**, 1601-1605 (1986).
25. Hommel, M., Kraft, O. and Arzt, E., "A new method to study cyclic deformation of thin films in tension and compression", *J. Mater. Res.* **14** (6), 2373-2376 (1999).
26. Hommel, M., Kraft, O., Baker, S. P. and Arzt, E., "Micro-Tensile and Fatigue Testing of Copper Thin Films on Substrates", in *Materials Science of Microelectromechanical Systems (MEMS) Devices*, edited by Heuer, A. H. and Jacobs, S. J. (Mater. Res. Soc. Symp. Proc. Vol. 546, Materials Research Society, Warrendale, PA (1999)), pp. 133-138.
27. Hommel, M., "Röntgenographische Untersuchung des monotonen und zyklischen Verformungsverhaltens dünner Metallschichten auf Substraten", *PhD Dissertation* (Institut f. Metallkunde, Universität Stuttgart (2000)).
28. Kraft, O., Schwaiger, R. and Wellner, P., "Fatigue in Thin Films: Lifetime and Damage Formation", to be published in *Mater. Sci. Eng. A.*
29. Gianuzzi, L. A. and Stevie, F. A., "A review of focused ion beam milling techniques for TEM specimen preparation", *Micron* **30** (3), 197-204 (1999).
30. Edington, J. W., "Interpretation of transmission electron micrographs", Philips Technical Library, (1975), p. 14.

31. Kraft, O., Wellner, P., Hommel, M. and Schwaiger, R., to be submitted to J. Appl. Phys.
32. Suresh, S., "Fatigue of materials", Cambridge University Press, Cambridge (1998), p. 256.
33. Suresh, S., "Fatigue of materials", Cambridge University Press, Cambridge (1998), p. 223.
34. Schwaiger, R. and Kraft, O., "Fatigue behavior of thin silver films investigated by dynamic microbeam deflection", in *Thin Films: Stresses and Mechanical Properties VIII,* edited by Vinci, R. P., Besser, P. R., Kraft, O., Moody, N. and Shaffer, E. (Materials Research Society Symp. Proc. Vol. 594, Materials Research Society, Pittsburgh, PA (2000)), pp. 201-206.
35. Nix, W. D., "Mechanical Properties of Thin Films", *Metall. Trans. A* **20**, 2217-2245 (1989).
36. Essmann, U., Gösele, U. and Mughrabi, H., "A model of extrusions and intrusions in fatigued metals", *Phil. Mag. A* **44** (2), 405-426 (1981).
37. Schwaiger, R. and Kraft, O., "High Cycle Fatigue of Thin Silver Films Investigated by Dynamic Microbeam Deflection", *Scripta Mater.* **41** (8), 823-829 (1999).
38. Yamamoto, A., Saka, H. and Imura, T., "In-situ study on the Fatigue Process of Metals by HVEM", *Kristall und Technik* **14** (10), 1275-1281 (1979).
39. Ogura, T. and Karashima, S., "Studies on the structure developed around fatigue cracks of aluminium using a high voltage electron microscope", *Trans. Japan Inst. Metals* **15**, 324 (1974).
40. Piqueras, J., Grosskreutz, J. C. and Frank, W., "The influence of point-defect clusters on fatigue hardening of copper single crystals", *Phys. Stat. Sol. A* **11**, 567-580 (1972).
41. Antonopoulos, J. G. and Winter, A. T., "Weak-beam study of dislocation structures in fatigued copper", *Phil. Mag.* **33**, 87-95 (1976).
42. Antonopoulos, J. G., Brown, L. M. and Winter, A. T., "Vacancy dipoles in fatigued copper", *Phil. Mag.* **34** (4), 549-563 (1976).
43. Johnson, E. W. and Johnson, H. H., "Imperfection density of fatigued and annealed copper via electrical-resistivity measurements", *Trans. Metall. Soc.* **233**, 1333-1339 (1965).
44. Polák, J., "Resistivity of fatigued copper single crystals.", *Mater. Sci. Eng.* **89**, 35-43 (1987).
45. Gao, H., Zhang, L., Nix, W. D., Thompson, C. V. and Arzt, E., "Crack-like grain-boundary diffusion wedges in thin metal films", *Acta Mater.* **47** (10), 2865-78 (1999).

46. Weiss, D., "Deformation Mechanisms in Pure and Alloyed Copper Films", *PhD Dissertation* (Institut für Metallkunde, Universität Stuttgart (2000)).
47. Gottstein, G., Bewerunge, J., Mecking, H. and Wollenberger, H., "Stored energy of 78k tensile deformed copper crystals", *Acta Metall.* **23** (5), 641-652 (1975).

Chapter 5 On the Nucleation of Voids During Fatigue of Thin Cu Films

5.1 Introduction

In the preceding chapters we have pointed out that void nucleation is decisive for thin film fatigue failure. In this part we will show by a simple model that indeed a sufficiently large number of vacancies is created in the course of cyclic deformation.

First, the relevant results of foregoing chapters, which the model to be presented is based on, will be summarized. A general observation on our fatigued thin film specimens is the formation of extrusions at the surface and voids at the film-substrate interface beneath the extrusions (see Figures 3.8, 4.6, and 4.7). Void formation was interpreted as a result of annihilation of edge dislocations. A qualitative model was presented, which is based on a dimensional constraint on dislocation motion and dislocation annihilation (see section 3.4.1).

The role of vacancies in bulk fatigue has also been described. Briefly, it was observed that dislocations in bulk single crystal Cu with opposite Burgers vectors spontaneously annihilate over a distance of 1.6 or 50 nm [1], depending on whether they have edge or screw character, respectively. For fatigued Cu single crystals, it was reported that annihilation of edge dislocations in *PSB* walls will produce higher vacancy concentrations than at thermal equilibrium [2] resulting in a net volume increase of the specimen. As a result of this vacancy supersaturation, extrusions are formed. The height η of the extrusions was modeled to be only $\eta \approx 3\times10^{-4} d$, where d is the grain size or specimen thickness in polycrystalline specimens and single crystals, respectively [Essmann, 1981 #168]. In contrast, in our thin films the height of the extrusions is of the same order as the original film thickness (Fig.3.8 and Ref. [3]). Therefore, and also from the large size of the observed voids, it can be concluded that for the fatigued thin film samples, vacancies are more important than for bulk.

The damage morphology of the thin Cu films (Figures 4.6 and 4.7) suggests the following sequence of events for fatigue failure: (i) surface roughening and formation of small voids close to or at the film/substrate interface, predominantly in large grains, (ii) crack nucleation at these voids and crack extension towards the film surface, and (iii) crack growth leading to the observed pattern of cracks and extrusions. This description is supported by the fact that cracking is only observed when extrusions and voids are already present. This has been confirmed by interrupted fatigue tests [Schwaiger, 2000 #350]. Hence, it is reasonable to say that the fatigue lifetime of a film is controlled by the time required to nucleate a void from

which the crack starts. In the following, a simple model is derived aiming to predict the fatigue lifetime of thin metal films, with respect to film thickness and grain size as a function of the applied plastic strain range.

5.2 Lifetime model

The number of vacancies created during fatigue is a function of the plastic strain. The plastic strain $\Delta\varepsilon_{pl}$ applied during one half-cycle of a fatigue experiment leads to the formation of Z_d dislocation loops of same Burgers vector inside one grain:

$$\Delta\varepsilon_{pl} = Z_d \frac{b}{d} \qquad (5.1)$$

where b is the magnitude of the Burgers vector and d the grain size.

Fig. 5.1 shows a schematic of a cuboidal grain of size d in a film of thickness h with interface dislocations of same Burgers vector separated by a distance δ_a. We assume that dislocations will annihilate with dislocations of opposite Burgers vectors at a distance smaller than y_e. The probability for dislocation annihilation is assumed to be $2y_e/\delta_a$, where δ_a is the average distance between dislocations of same Burgers vector after a steady-state dislocation structure has evolved after a certain number of cycles. Values for $2y_e/\delta_a$ are between 0 - when no interface dislocations at all exist - and 1 - when the spacing between dislocations of same Burgers vector equals $2y_e$. For the latter configuration, every dislocation pair with opposite Burgers vectors will annihilate.

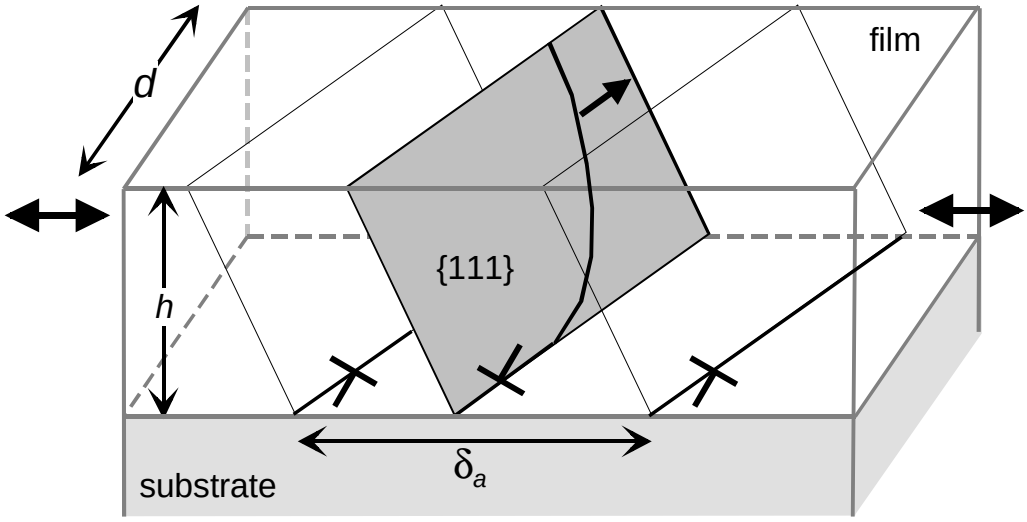

Fig. 5.1: Schematic representation of the deformation mechanism in a thin film envisioned for the model described in 3.4.1. Dislocation segments with same Burgers vectors separated by a distance δ_a are present at the interface. Under cyclic loading, dislocations of opposite Burgers vectors are deposited. Dislocation annihilation occurs when the distance between dislocations of opposite Burgers vector becomes smaller than the annihilation distance ($\delta_a/2 < y_e$). The grains are assumed to be cuboidal, with grain size *d*.

Using eq.(5.1), the number Z_{ann} of annihilating dislocations per half-cycle is calculated to be

$$Z_{ann} = Z_d \frac{2y_e}{\delta_a} = \frac{\Delta\varepsilon_{pl} d}{b} \frac{2y_e}{\delta_a} \tag{5.2}$$

The number Z_{vac} of vacancies produced when Z_{ann} dislocations annihilate during one half-cycle is estimated to be:

$$Z_{vac} = A \frac{d}{b} Z_{ann} \tag{5.3}$$

where *A* is the number of vacancies produced per lattice site, and *d/b* the number of lattice sites along a dislocation within one grain.

Using eq.(5.3) and $Z_{lat}=d^2h/b^3$ for the number Z_{lat} of lattice sites in a cuboidal grain in a film of thickness *h*, the concentration C_N of vacancies produced after *2N* half-cycles is given by

$$C_N = 2N \frac{Z_{vac}}{Z_{lat}} = 2N \frac{A Z_{ann} b^2}{dh} \tag{5.4}$$

Damage formation occurs when the vacancy concentration reaches a critical value C_{cr}. After rearranging eq.(5.4) and inserting eq.(5.2), the number N_d of cycles to damage formation is determined to be

$$N_d = \frac{C_{cr} h \delta_a}{2Ab\Delta\varepsilon_{pl} y_e} \tag{5.5}$$

Finally, we estimate the average distance δ_a between dislocations. Two limiting conditions are considered:

First, the annihilation process is the only mechanism by which dislocations are removed from the grain. In this case, dislocations will be added at the interface until $\delta_a/2 = y_e$. Solving eq. (5.5) for $\Delta\varepsilon_{pl}$ leads to

$$\frac{\Delta\varepsilon_{pl}}{2} = \frac{C_{cr} h}{Ab} \frac{1}{2N_d} \tag{5.6}$$

It is obvious that the *Coffin -Manson* relation (chapter 2, eq.2.8) and eq.(5.6) have the same form with a fatigue exponent c_d=-1.

In the second case, we account for additional mechanisms removing dislocations from a grain and leading to a steady-state condition after N_s cycles. At this point δ_a (>$2y_e$) becomes constant. After N_s cycles, the number of dislocations of same Burgers vector inside the grain is given by

$$N_s Z_d = N_s \Delta\varepsilon_{pl} \frac{d}{b} \tag{5.7}.$$

The resulting mean planar spacing δ_a is given by

$$\delta_a = \frac{d}{N_s Z_d} = \frac{b}{N_s \Delta\varepsilon_{pl}} \tag{5.8}.$$

After inserting eq.(5.8) into eq.(5.5) and solving for $\Delta\varepsilon_{pl}$, we find

$$\frac{\Delta\varepsilon_{pl}}{2} = \left(\frac{C_{cr} h}{4AN_s y_e} \right)^{1/2} \left(\frac{1}{2N_d} \right)^{1/2} \tag{5.9}.$$

Eq.(5.9) also is of the same form as the *Coffin-Manson* relation, albeit with a fatigue exponent c_d=-0.5.

5.3 Comparison of experiment and model

For a comparison between experimentally determined lifetimes of thin films and calculated ones, lifetime data of Ref.[4] for 3 μm thick Cu films on a polyimide substrate were used. As the data was presented in terms of the total strain, it was necessary to estimate the experimentally applied plastic strain, which was not measured by the X-ray diffraction. We estimate the plastic strain range $\Delta\varepsilon_{pl}$ to be

$$\Delta\varepsilon_{pl} = \Delta\varepsilon_{tot} - \frac{2\sigma_y}{E} \qquad (5.10)$$

where $\Delta\varepsilon_{tot}$ is the total strain range, E Young's modulus, and σ_y the yield strength. Values for the latter were calculated by using the *Hall-Petch* relation

$$\sigma_y = \sigma_o + \frac{k_y}{\sqrt{d}} \qquad (5.11)$$

with σ_o=25 MPa for the yield strength of single crystal Cu [5], and the empirically determined constant k_y=0.112 MPa√m for Cu [6]. This estimate gives an upper limit for the plastic strain range, since strain hardening effects, which usually play an important role for the deformation of thin films [7], are neglected.

Fig. 5.2 compares the experimentally determined lifetimes [4] and the model presented above. The gray dashed line represents eq.(5.9) for 3 μm film thickness using the following values: b=0.256 nm, y_e=1.6 nm [1], and A=0.5 assuming that, on average, one vacancy per two lattice sites is produced upon dislocation annihilation. C_{cr} was estimated to be 0.001, corresponding to the vacancy concentration at the melting point of a *fcc* metal [8]. The number of cycles N_s until steady-state was reached was set to 10, since after 10 cycles the mechanical energy loss became almost constant [4]. The dashed black line in Fig. 5.2 represents eq.(5.6) with the same values for A and C_{cr}. It can be seen that eq.(5.9) of the model agrees reasonably with the experimental data. In particular, the measured fatigue exponent c_d of –0.4 is very close to the predicted one of -0.5.

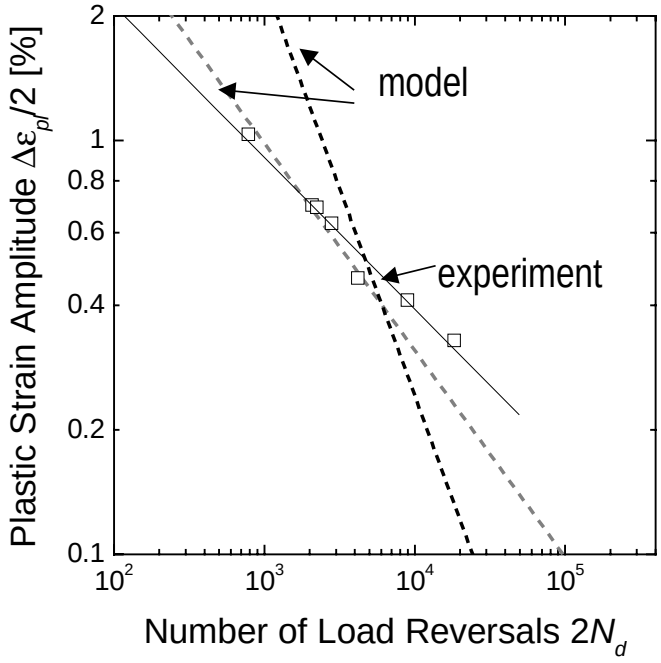

Fig. 5.2: Lifetime diagram for 3 µm thick Cu films compared to calculated lifetime data. The model predicts a power-law dependence with an exponent of about -0.5 (eq.(5.9), grey dashed line), the black dashed line corresponds to an exponent of about -1 (eq. (5.6)).

The model predicts that the fatigue resistance decreases with decreasing film thickness. This prediction is the contradictory to our results (chapter 4). In the model, we assume that the absolute number of vacancies produced by the annihilation process is independent of film thickness. As a result, the concentration of vacancies after a certain number of cycles scales inversely with the film thickness (eq.(5.4)) and, thus, more cycles have to be performed to produce a critical vacancy concentration in thicker films.

This discrepancy, however, may be due to the fact that vacancies annihilate at vacancy sinks, such as grain boundaries or the free surface (see 4.4.2). Our observations suggest that this indeed plays a role, since extrusions and voids are often found in the middle of large grains, indicating that the interface to the substrate is not an effective sink for vacancies. In very thin and fine-grained films, however, a supersaturation of vacancies sufficient for void nucleation might not be achieved, because too many vacancies reach the grain boundaries or the surface. This argument is in agreement with the observation that voids or extrusions are predominantly found in large grains and that smaller extrusions were found in the 0.4 µm thick films (Figs. 4.6 and 4.7).

It has to be stated that our model is a very strong simplification in terms of dislocation configurations occurring in reality. Nevertheless, it is a useful attempt to quantitatively link the dislocation dynamics under fatigue conditions to the formation of point defects. The reasonable agreement between model and experiment highlights the role of point defects for thin film fatigue.

5.4 Conclusions

It is argued that the formation of vacancies as a result of dislocation annihilation leads to void nucleation. Based on this consideration, a quantitative lifetime model for thin film fatigue was derived, which predicts the number of cycles required for building up a critical vacancy concentration. This model agrees reasonably well with the measured lifetimes of 3.1 μm thick films. However, in ist present state the model cannot explain the experimentally observed thickness dependence (chapter 4).

5.5 References

1. Essmann, U. and Mughrabi, H., "Annihilation of dislocations during tensile and cyclic deformation and limits of dislocation densities", *Phil. Mag. A* **40** (6), 731-756 (1979).
2. Essmann, U., Gösele, U. and Mughrabi, H., "A model of extrusions and intrusions in fatigued metals", *Phil. Mag. A* **44** (2), 405-426 (1981).
3. Schwaiger, R. and Kraft, O., "High Cycle Fatigue of Thin Silver Films Investigated by Dynamic Microbeam Deflection", *Scripta Mater.* **41** (8), 823-829 (1999).
4. Kraft, O., Schwaiger, R. and Wellner, P., "Fatigue in Thin Films: Lifetime and Damage Formation", to be published in *Mater. Sci. Eng. A.*
5. Embury, J. D., "Strengthening by dislocation substructures", in *Strengthening methods in crystals* (Elsevier Publ. Comp. Ltd.), pp. 331-402.
6. Feltham, F. and Meakin, J. E., *Phil. Mag.* **2**, 105 (1957).
7. Hommel, M. and Kraft, O., to be published in *Acta Mater.*
8. Simmons, R. O. and Balluffi, R. W., *Phys. Rev.* **117** (1), 52-61 (1960).

Chapter 6 Final Remarks

Two different methods were applied to investigate the fatigue behavior of thin metal films in the *HCF* and the *LCF* regimes, respectively. These two aspects were studied and discussed separately, but are, nevertheless, strongly linked. Within the scope of *HCF* investigations, Ag films with thicknesses between 0.2 and 1.5 µm on SiO_2 substrates were cyclically deformed utilizing cantilever microbeam deflection. This method allows the application of a large number of fatigue cycles at small amplitudes and was applied to describe the fatigue behavior in terms of the stress. The *LCF* behavior of thin Cu films with thicknesses between 0.4 and 3.0 µm on polyimide substrates was studied by cyclic tensile testing. The fatigue behavior was characterized in terms of the plastic strain amplitude. The preparation method for the Ag and Cu films resulted in an average grain size nearly independent of the film thickness. Therefore, dimensional effects could be attributed to either the film thickness or the grain size.

The dislocation distribution in a 3.0 µm thick Cu film was investigated by *TEM*. Mostly, individual dislocations were found, whereas in one case the dislocations could also be interpreted to be part of a more regular structure. In films thinner than the investigated one, it is even reasonable not to expect any long-range order, but only individual dislocations. However, in this direction more research is necessary to further clarify the nature of the dislocation arrangement, especially for films with submicron dimensions.

Extrusions similar to bulk extrusions were found at the surface of both the Ag and Cu films after cyclic loading. The extrusion height scaled with the film thickness, but the extrusion height in the thin films was much larger than predicted by bulk models. Voids were observed beneath the extrusions at the film-substrate interface. The voids appear to contribute significantly to thin film failure, since they appear to be the site for crack initiation.

The occurrence of extrusions and voids was explained qualitatively by a model that combines mechanisms of bulk fatigue with constraints exerted on dislocations by the small dimensions of a thin film. The model is based on a dimensional constraint on dislocation motion. When a dislocation moves in a thin film an additional dislocation segment has to be laid down at the film-substrate interface, which requires a certain amount of stress. It is suggested, that the edge segments of the interface dislocations annihilate to form vacancies, whereas the annihilation of screw dislocations does not produce vacancies. A localized supersaturation of vacancies leads to void nucleation. Hence, vacancies are more important in case of thin film fatigue. The gliding dislocations leave the film at the surface, thereby forming steps that finally accumulate in the form of an extrusion.

Application of this model implies the following points: (i) when no voids are nucleated, the formation of fatigue damage is suppressed, (ii) a minimum stress is required to move a dislocation in a thin film, and thus a stress fatigue limit exists, which is expected to scale with the inverse film thickness.

We have shown that the stress amplitude necessary to induce fatigue damage in the Ag films scales inversely with the film thicknesses. For all film thicknesses, this experimentally determined critical value was greater than the minimum stress required to move a dislocation and increased significantly for films thinner than ~0.6 μm. The existence of a fatigue limit was also indirectly shown by testing the films at various mean stress levels: On one hand, the presence of a mean stress reduced the fatigue lifetime of the films, however, on the other hand, an extremely high mean stress did not cause fatigue damage when the stress amplitude was sufficiently small.

Lifetime increased with decreasing film thickness for Cu films fatigued at a plastic strain amplitude of 0.8 %. From comparison with previous results, similar behavior was observed for smaller grained films. Furthermore, small extrusions in the 0.4 μm thick, 1 μm grain size film were produced in the course of fatigue, whereas cracks, but no extrusions were found in 0.4 μm thick, 0.28 μm grain size films. Thus, for sufficiently small grain size a different failure mechanism seems to be active.

These findings indicate that void nucleation is increasingly inhibited with decreasing film thickness and/or grain size. We propose the following explanation: Since vacancies are mobile at room temperature, the excess vacancy concentration depends strongly on the sink density. The interface between the film and the substrate does not act as a sink or source for point-defects, as discussed for diffusional creep in thin films, and a sufficiently high concentration of vacancies should be obtained. Hence, in a thin film strongly adherent to a substrate, the diffusion of vacancies can be accomplished if, beside dislocations, the surface as well as the grain boundaries act as vacancy sinks. With increasing cycles, the vacancy concentration increases despite the simultaneous annihilation of vacancies at grain boundaries and surfaces. The time to reach a grain boundary or surface decreases with decreasing grain size and film thickness, respectively. Thus, for thinner and finer-grained films the time to build up a critical vacancy concentration increases. In the limit of very thin, fine-grained films this critical concentration may never be reached.

Our findings that fatigue failure in thin films is closely related to void nucleation and growth are supported by a simple model. We have shown in an admittedly simplistic picture that a sufficiently large number of vacancies is created in the course of cyclic loading.

This research work was not concerned with fatigue crack propagation. However, this field is also worth investigating. Peculiarities in the crack growth behavior will also be expected, since the film thickness and the presence of a substrate largely affect the stress state at the crack tip and cracks in thin films are usually of the same size as microstructural features.

Further work is required to better understand how fatigue mechanisms operate in small dimensions, and how they depend on grain size and texture. The role of vacancies, for instance, may be further elucidated by fatigue tests at different temperatures. According to the fatigue model, vacancy mobility is the crucial factor for the fatigue resistance of thin films on substrates. Consequently, the fatigue resistance of thin films on a substrate at high temperature should be better than that at low temperature, since vacancy diffusion is enhanced and void nucleation suppressed.

Fatigue in small dimensions cannot be completely described by using bulk models and new models must account for the effect of a substrate, free surface, and reduced dimensions. The increasing technological relevance of thin film fatigue will give rise to more research work and a better understanding of the relevant mechanisms.

Appendix

A Fatigue testing of thin Ag films

A.1 Grain size distributions

In this section plots of the grain size distributions for the Ag films investigated in chapter 3 and determined following the procedure described in 3.3.1 are shown.

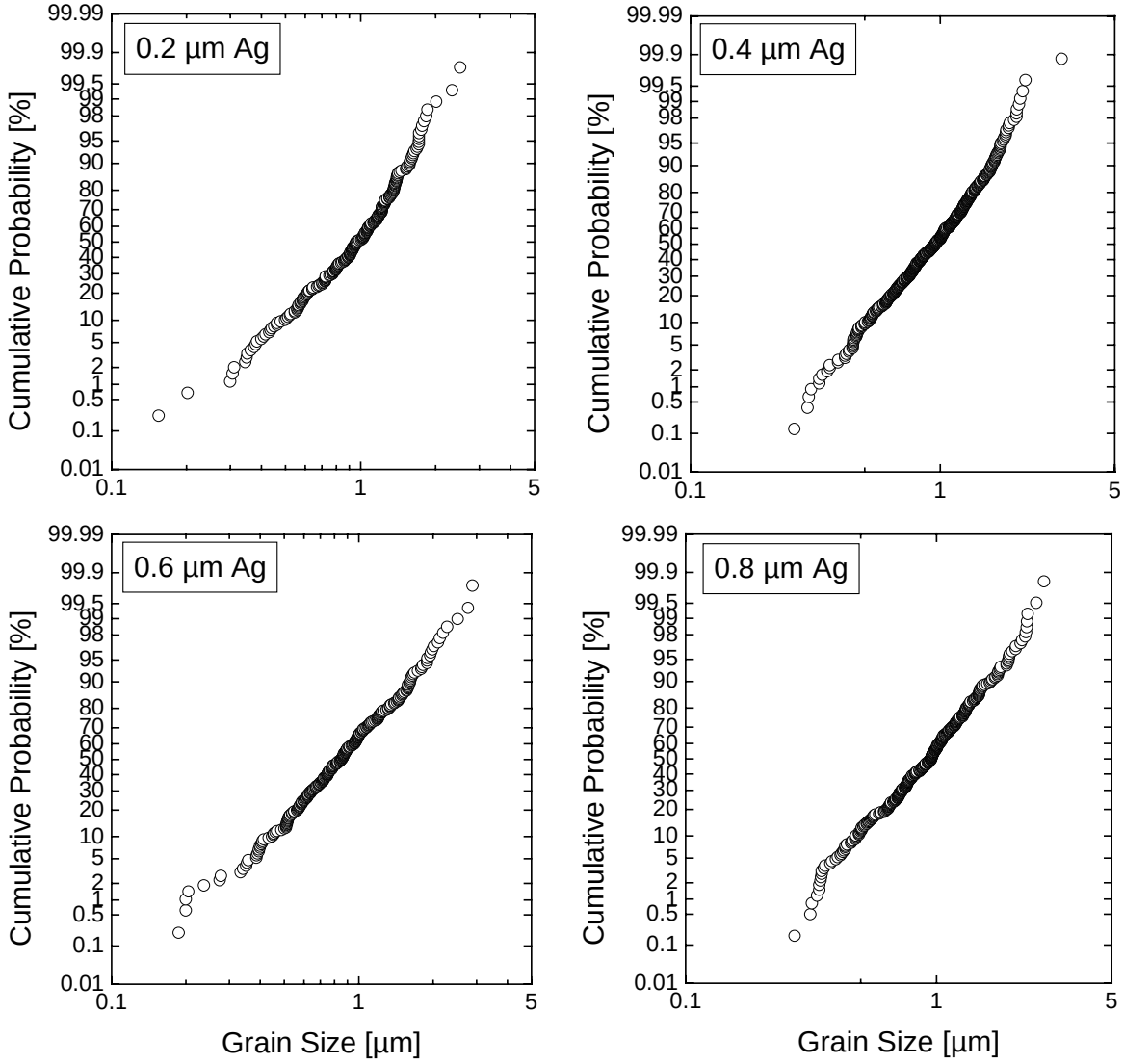

Fig. A.1: Cumulative probabilities of the grain size of Ag films with different film thicknesses

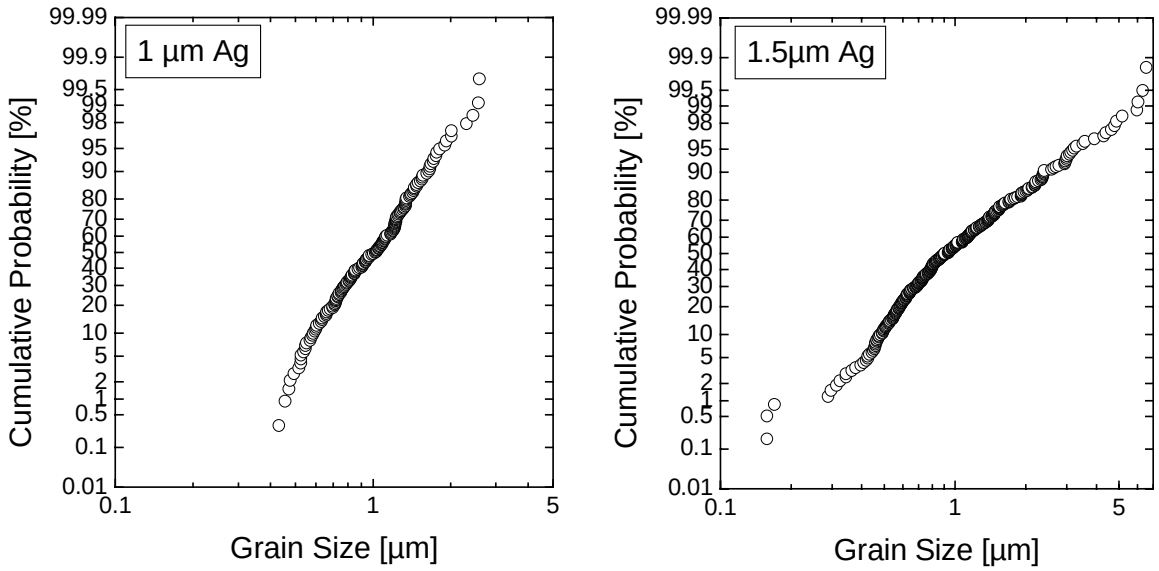

Fig. A.1 (continued)

A.2 Monotonic stress-strain behavior

The average values and deviations of σ_y and Θ according to fig. 3.4 are summarized in Table A.1.

Film thickness [µm]	σ_y [MPa]	$s_{\sigma y}$ [MPa]	Θ [MPa]	s_Θ [MPa]
0.2	300	7	30 000	1000
0.4	290	8	29 000	500
0.6	270	7	28 000	700
0.8	250	5	18 000	1000
1.0	210	10	13 000	1200
1.5	155	1	15 000	100

Table A.1: Average values for σ_y and Θ for different film thicknesses.

A.3 Fatigue tests

Fig. A.2 - Fig. A.6 show the stiffness versus the number of cycles for fatigue tests performed on different film thicknesses. The data are summarized in Table A.2.

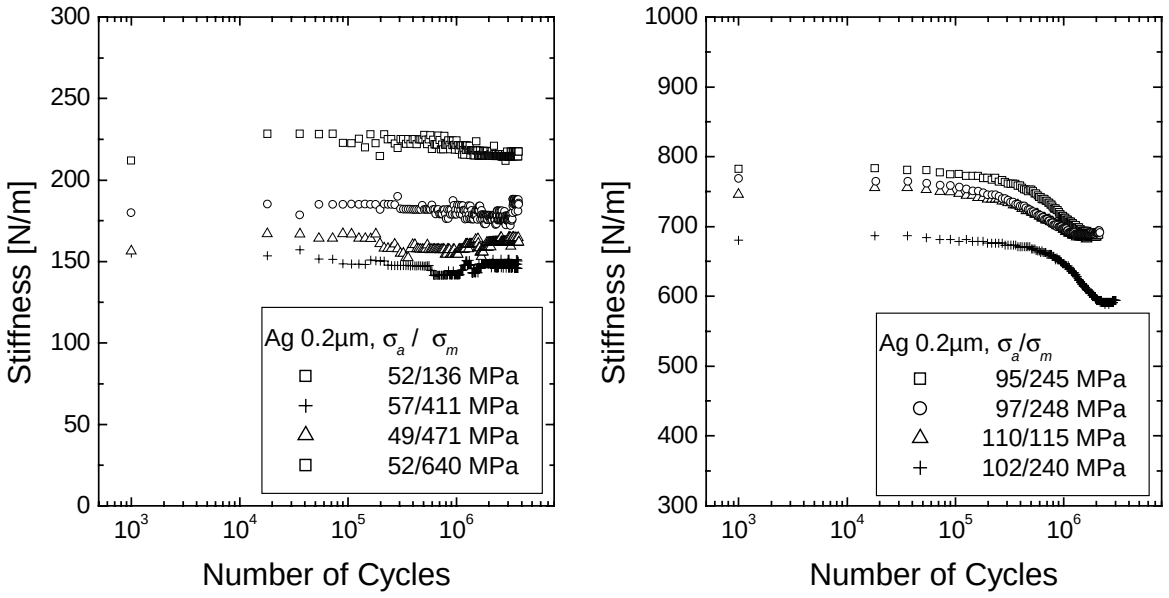

Fig. A.2: Stiffness versus the number of cycles for the 0.2 µm thick Ag film tested at stress amplitudes σ_a at which (a) no fatigue damage occurred and (b) fatigue damage occurred.

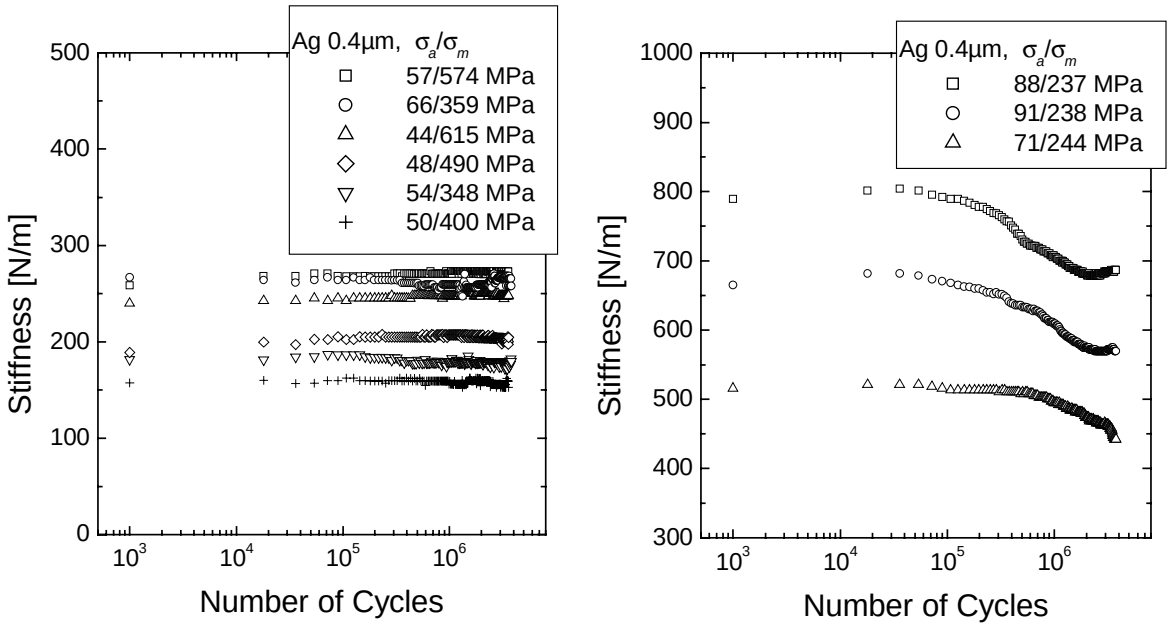

Fig. A.3: Stiffness versus the number of cycles for the 0.4 µm thick Ag film tested at stress amplitudes σ_a at which (a) no fatigue damage occurred and (b) fatigue damage occurred.

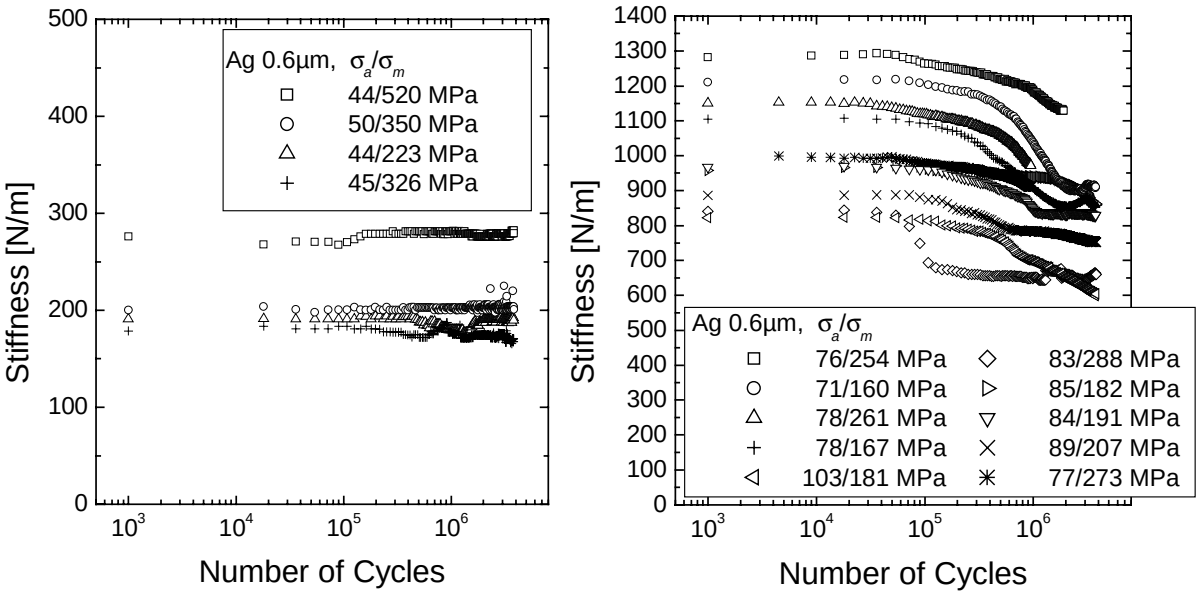

Fig. A.4: Stiffness versus the number of cycles for the 0.6 µm thick Ag film tested at stress amplitudes σ_a at which (a) no fatigue damage occurred and (b) fatigue damage occurred.

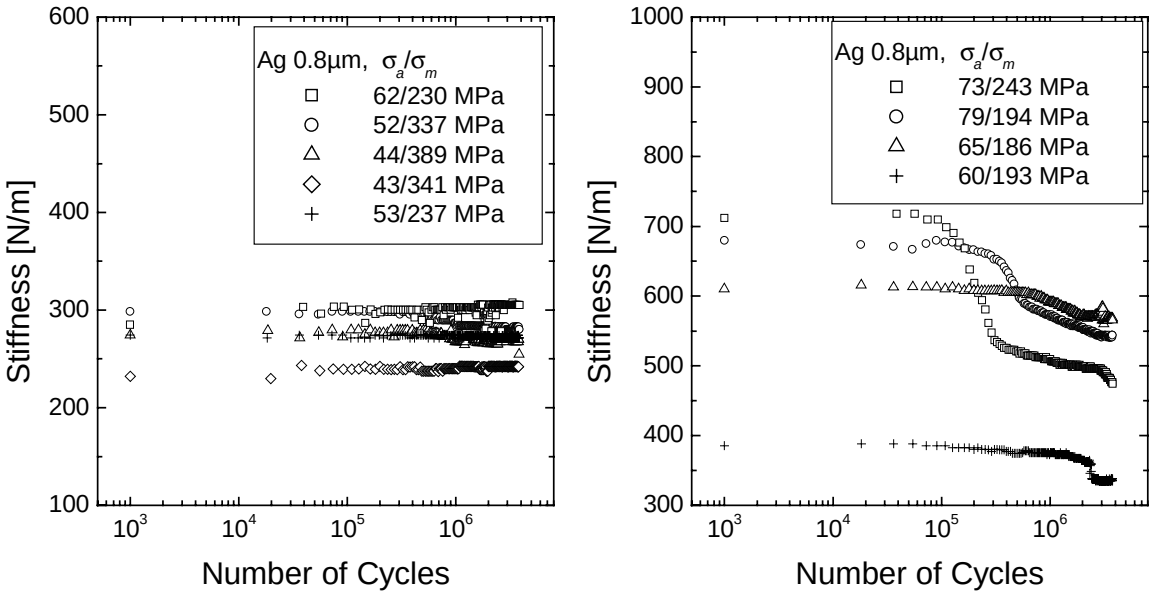

Fig. A.5: Stiffness versus the number of cycles for the 0.8 µm thick Ag film tested at stress amplitudes σ_a at which (a) no fatigue damage occurred and (b) fatigue damage occurred.

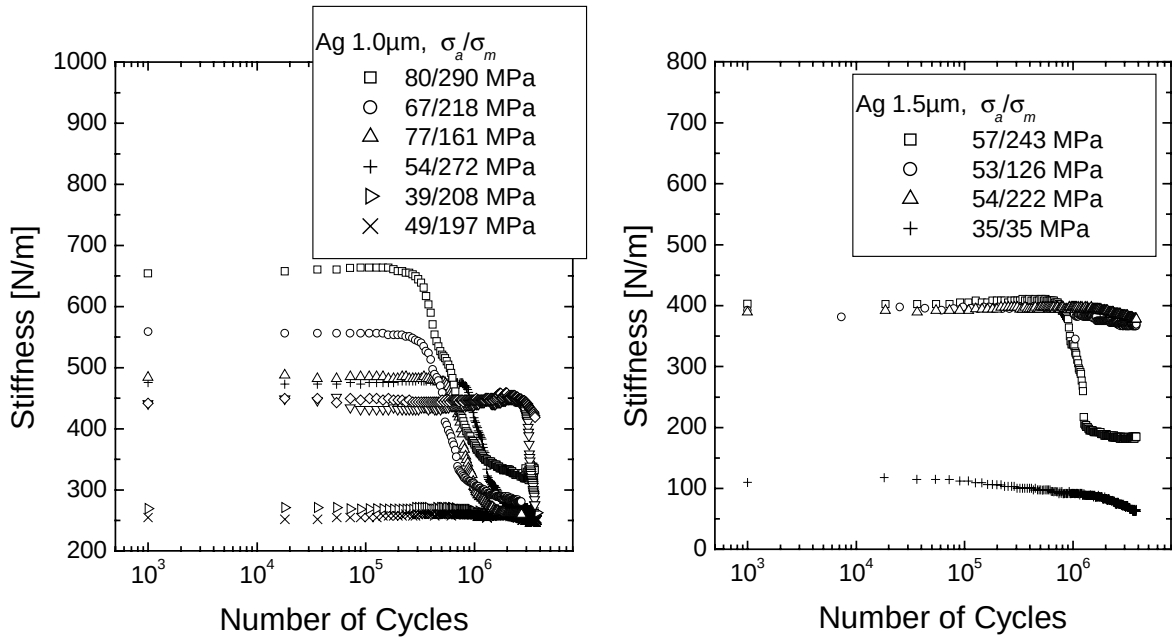

Fig. A.6: Stiffness versus the number of cycles for the (a) 1.0 µm and (b) 1.5 µm Ag films.

Film thickness [µm]	σ_a [MPa]	σ_m [MPa]	N_d
0.2	49	471	$> 3.8 \times 10^6$
	52	136	$> 3.8 \times 10^6$
	57	411	$> 3.8 \times 10^6$
	95	245	1.08×10^5
	97	248	1.09×10^5
	102	240	2.88×10^5
	110	115	2.52×10^5
0.4	44	615	$> 3.8 \times 10^6$
	48	490	$> 3.8 \times 10^6$
	50	400	$> 3.8 \times 10^6$
	54	348	$> 3.8 \times 10^6$
	57	574	$> 3.8 \times 10^6$
	66	359	$> 3.8 \times 10^6$
	71	244	8.46×10^5
	88	237	1.08×10^5
	91	238	9.7×10^4

Table A.2: Experimental data of fatigue tests on different film thicknesses

0.6	44	223	$> 3.8 \times 10^6$
	44	520	$> 3.8 \times 10^6$
	45	326	$> 3.8 \times 10^6$
	50	350	$> 3.8 \times 10^6$
	51	494	$> 3.8 \times 10^6$
	71	160	4.68×10^5
	76	254	7.21×10^4
	77	273	4.51×10^4
	78	261	4.96×10^4
	83	288	5.4×10^4
	84	191	1.62×10^5
	85	182	1.08×10^5
	89	207	9.6×10^4
	103	181	2.88×10^4
0.8	43	341	$> 3.8 \times 10^6$
	44	389	$> 3.8 \times 10^6$
	52	337	$> 3.8 \times 10^6$
	53	237	$> 3.8 \times 10^6$
	60	193	2.4×10^6
	62	230	$> 3.8 \times 10^6$
	65	186	7.4×10^5
	73	243	1.3×10^5
	79	194	1.4×10^5
1.0	39	208	$> 3.8 \times 10^6$
	49	197	$> 3.8 \times 10^6$
	54	272	8.9×10^5
	67	218	7.8×10^5
	77	161	5.5×10^5
	80	290	2.7×10^5
1.5	35	35	1.1×10^6
	53	126	1.1×10^6
	54	222	9.2×10^5
	57	243	7.5×10^5

Table A.2 (continued)

B Grain size distributions of thin Cu films

In this section plots of the grain size distributions for the Cu films investigated in chapter 4 and determined following the procedure described in 3.3.1 are shown.

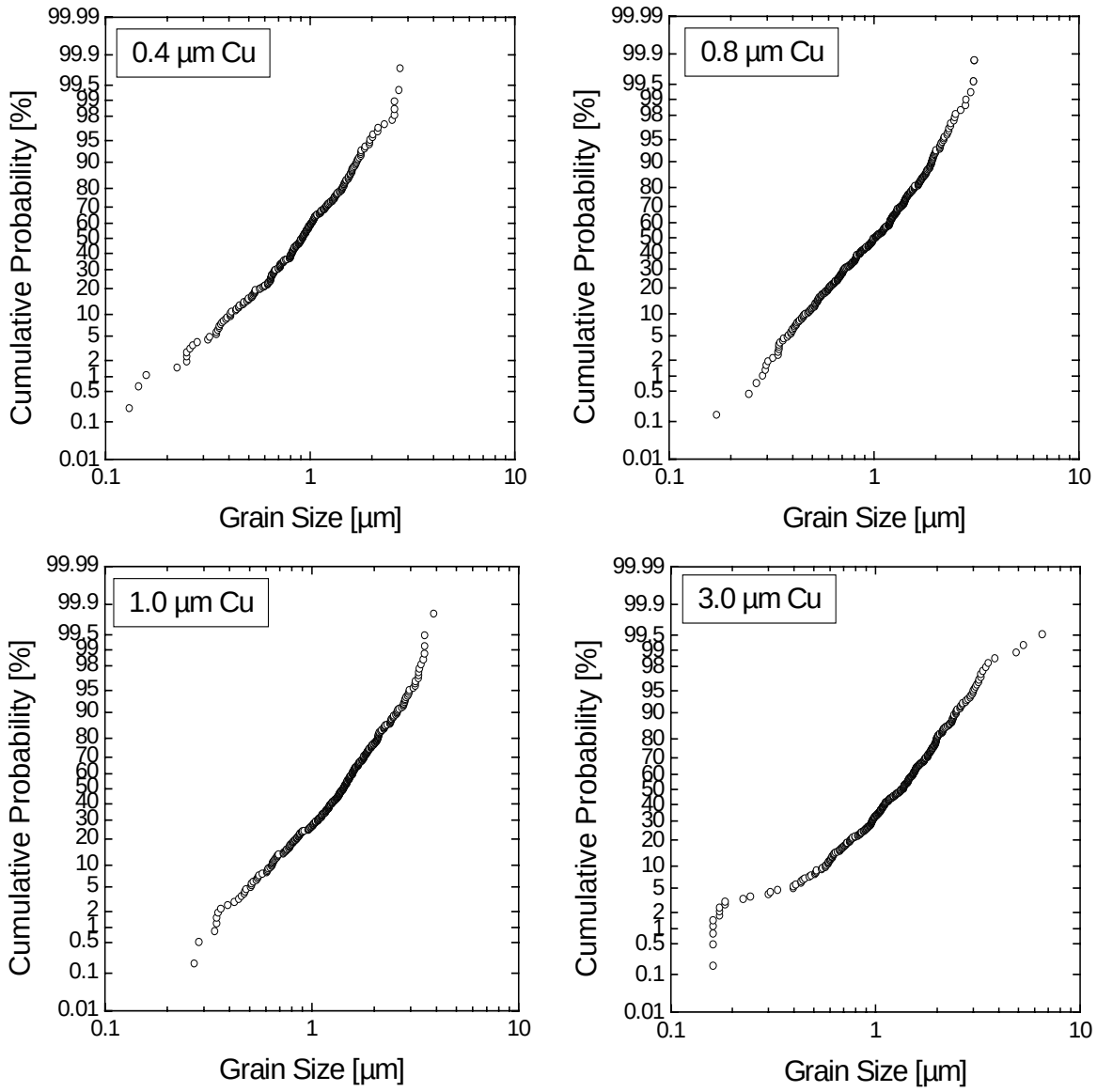

Fig. B.1: Cumulative probabilities of the grain size of Cu films with different film thicknesses

C List of Symbols

da/dN	crack length increment per cycle (m)
A	grain area (m^2),
	also: number of vacancies per lattice site
α	angle between the glide plane normal and the tensile axis
$\boldsymbol{b}$	Burgers vector
b	Burgers vector length (m)
β	numerical constant describing the stress field of a dislocation
C	scaling constant used in the *Paris* law
c_d	fatigue ductility exponent
c_s	fatigue strength exponent
C_{cr}	critical vacancy concentration
C_N	concentration of vacancies after N cycles
d	grain diameter (m)
	also: specimen thickness (m)
d_m	mean grain size (m)
d_{50}	median grain size (d)
δ_a	average distance between dislocations with same Burgers vectors (m)
E	Young's modulus (N/m^2)
ε	strain
ε_a	total strain amplitude
ε_{ae}	elastic strain amplitude
ε_{ap}	plastic strain amplitude
ε_f'	fatigue ductility coefficient
ε_{pl}	plastic strain

ε_x	total strain along the beam axis,
	also: elastic strain in the tensile direction in microtensile tests
$\varepsilon_{x,pl}$	plastic strain along the beam axis
$\Delta\varepsilon_{tot}$	total strain range
$\Delta\varepsilon_{pl}$	plastic strain range
F_{max}	maximum force in a loading cycle (N)
F_{min}	minimum force in a loading cycle (N)
Φ	angle between the glide plane normal and the film normal
γ_r	resolved shear strain
γ_s	total applied resolved shear strain in a stress-strain cycle
γ_{pl}	plastic shear strain amplitude
γ_{el}	elastic shear strain amplitude
h	film thickness (m)
η	extrusion height (m)
K_{Ic}	static fracture toughness ($Nm^{-3/2}$)
K_{max}	maximum value of the stress intensity factor ($Nm^{-3/2}$)
K_{min}	minimum value of the stress intensity factor ($Nm^{-3/2}$)
ΔK	range of the stress-intensity factor ($Nm^{-3/2}$)
ΔK_0	threshold stress intensity factor range ($Nm^{-3/2}$)
L	cantilever length (m)
λ	angle between the film normal and the Burgers vector
m	scaling constant used in the *Paris* law
μ_f, μ_s	shear moduli of film and substrate (N/m^2)
N_d	number of cycles to damage formation,
	also: number of cycles to stiffness decrease

N_f	number of cycles to failure
N_s	number of cycles to reach a steady state condition
$2N_f$	number of load reversals
$2N_t$	transition life: number of load reversals to failure at which the elastic and plastic strain amplitudes are equal
ν	Poisson's ratio
Θ	work hardening rate (N/m^2)
R	loading ratio
σ	stress (N/m^2)
σ_a	stress amplitude (N/m^2)
σ_m	mean stress (N/m^2)
σ_{max}	maximum stress in a loading cycle (N/m^2)
σ_{min}	minimum stress in a loading cycle (N/m^2)
σ_{Nix}	stress required to move a dislocation through a film according to Nix (N/m^2)
σ_x	stress along the beam axis (N/m^2)
σ_x^{sat}	saturation stress in the direction of the beam axis (N/m^2)
σ_y, $\sigma_{0.2}$	yield stress and yield stress at a 0.2 % strain (N/m^2)
σ_o	yield strength of single crystals (N/m^2)
$\Delta\sigma$	stress range in a fatigue cycle (N/m^2)
σ_f'	fatigue strength coefficient
τ_r	resolved shear stress (N/m^2)
τ_s	peak resolved stress in a stress-strain cycle (N/m^2)
τ_s^{sat}	peak resolved shear stress at saturation (N/m^2)
ΔW	energy loss (J)
x	variable defining the distance along the beam axis (m)

y_e	annihilation of edge dislocations (m)
ψ	angle between the surface normal and the normal of the diffracting crystal planes
Z_{ann}	number of annihilating dislocations
Z_d	number of dislocation loops in a grain of size d
Z_{lat}	number of lattice sites

D List of Abbreviations

HCF	high cycle fatigue
S-N curves	stress-life plots, Wöhler curves
LCF	low cycle fatigue
CSS curve	cyclic stress-strain curve
Fcc	face-centered cubic
PSB	persistent slip band
FIB	focused ion beam
UHV	ultra-high vacuum
XRD	x-ray diffraction
EBSD	electron backscatter diffraction
OIM	orientation imaging microscopy
CSM	continuous stiffness measurement
FEA	finite element analysis
TEM	transmission electron microscopy